GEOMETRIC OPTICAL METASURFACE FOR POLARIZATION CONTROL

Fuyong Yue

Submitted for the degree of Doctor of Philosophy

Heriot-Watt University

School of Engineering & Physical Sciences

September 2017

ABSTRACT

Like amplitude and phase, polarization is one of the fundamental properties of light. Controlling polarization in a desirable manner is fundamental to science and technology. However, practical applications based on polarization manipulation are mainly hindered by the complexity of experimental system, bulky size and poor spatial resolution. In recent years, metasurfaces have drawn considerable attention in the scientific community due to their exotic electromagnetic properties and potential breakthrough for light manipulation. With the development of nanophotonics, the generation of arbitrary spatially-varying polarization from an input beam is achievable. The objective of this thesis is to develop metasurface approaches to control phase and polarization of light in subwavelength scale for novel applications, such as polarization-controlled hologram generation and structured beam generation. The emphasis of the thesis is placed on the polarization control using geometric plasmonic metasurfaces.

We start by reviewing recent progress regarding novel planar optical components. After the introduction of mechanism of light-nanostructure interaction and the far-field scattering of metal nanostructure arrays based on Mie theory, we discuss the abrupt phase change emerging from rotated nanostrips and the generalized Snell's law. To demonstrate the precise phase manipulation, we develop a metasurface approach for polarization-controlled hologram generation. Moreover, we propose and experimentally demonstrate a novel method to realise the superposition of orbital angular momentum states in multiple channels using a single device.

Spring from the superposition of two opposite circular polarizations, two different approaches for polarization manipulation at nanoscale are developed and experimentally verified. Based on the first approach, a vector vortex beam with inhomogeneous polarization and phase distributions is demonstrated, which features the spin-rotation coupling and the superposition of two orthogonal circular components, i.e., the converted part with an additional phase pickup and the residual part without a phase change. The

second approach is to control the phase of the two orthogonal circular components simultaneously to engineer the polarization profile. Furthermore, we adopt this approach to develop a compact metasurface device which can hide a high-resolution grayscale image in a laser beam. The compactness of metasurface approach in polarization manipulation renders this technology very attractive for diverse applications such as encryption, imaging, optical communications, quantum science, and fundamental physics.

DEDICATION

To my family and my girlfriend.

DECLARATION STATEMENT

(Research Thesis Submission Form should be placed here)

ACKNOWLEDGEMENTS

First and foremost, I would like to thank Dr. Xianzhong Chen for providing me the opportunity to pursue my PhD study with his supervision. I appreciate all his contributions of time, ideas, and funding to make my PhD experience productive and stimulating. During the years of working with him, I got the professional trainings as a PhD candidate and a scientific researcher. I learned a great deal from him such as the nanofabrication, numerical simulation, and experimental skills. His attention toward my study gives me a solid standing ground in my research. His enthusiasm for science and its understanding, and his wealth of ideas never ceases to amaze me. I would like to take this opportunity to thank my second supervisor Prof. Brian D Gerardot for all his support. I also sincerely thank Prof. Shuang Zhang from University of Birmingham for his instructions.

Thanks to Dandan Wen, who is my close colleague, for providing big helps on my research. Thanks to Mrs Chunmei Zhang for her help in lab, and the wonderful party at every Christmas day. I would like to thank Neil Ross, Mark Lenard, Adrian Dzipalski, Dr. Santosh Kumar, for all the help regarding nanofabrication. I would like also to thank my friends Prof. Jinghua Sun, Dr. Ximing Ren, and Yang Chen for all the support. I feel very lucky to have these wonderful friends in Edinburgh. Many thanks to our visiting scholars, Prof. Ming Chen, Dr. Huigang Liu, Dr. Xiaofei Zang and Dr. Zhengren Zhang. Their broad knowledge always inspires me.

Particularly, I am grateful to my girlfriend Qianru Zhou for her support and love, and for helping me to put everything into perspective.

Finally, my deepest appreciations go to my parents and my sister. Without their selfless support, I never have the chance to sit in the office at Heriot-Watt University to write this thesis.

TABLE OF CONTENTS

LISTS OF TABLES AND FIGURES

LIST OF PUBLICATIONS

Journal papers

1. **Yue F.**, Zhang, C., Zang X., Wen D., Gerardot B. D., Zhang S., Chen X. *High-resolution grayscale image hidden in a laser beam*. Light: Science & Applications accepted article preview 31 August (2017), doi: 10.1038/LSA.2017.129.

2. **Yue F.**, Wen D., Zhang C., Gerardot B. D., Wang W., Zhang S., Chen X. *Multichannel polarization-controllable superposition of orbital angular momentum states*. Advanced Materials, (2017), 29 (15): 1603838.

3. **Yue F.**, Wen D, Xin J, Gerardot B. D., Li J, Chen X. *Vector vortex beam generation with a single plasmonic metasurface*. ACS Photonics, (2016), 3(9): 1558-1563.

4. **Yue F.**, Zang X., Wen D., Li Z., Zhang C., Liu H., Gerardot B., Wang W., Zheng G., Chen X. *Geometric phase generated optical illusion*. Scientific Reports (2017), 7: 11440.

5. Wen D.*, **Yue F.***, Li G. *****, Zheng G., Chan K., Chen S., Chen M., Li K.F., Wong P.W.H., Cheah K.W. and Pun E.B., Zhang S., Chen X. *Helicity multiplexed broadband metasurface holograms*. Nature Communications (2015), 6. **authors contributed equally to this work.*

6. Zhang C. *, **Yue F. ***, Wen D. *, Chen M., Zhang Z., Wang W., and Chen X. *Multi-channel metasurface for simultaneous control of holograms and twisted light beams.* ACS Photonics, (2017), 4(8): 1906-1912. ***authors contributed equally to this work.*

7. Wen D., **Yue F.**, Ardron M., Chen X. *Multifunctional metasurface lens for imaging and Fourier transform*. Scientific Reports (2016), 6: 27628.

8. Wen D., **Yue F.**, Zhang C., Zang X., Liu H., Wang W., Chen X. *Plasmonic metasurface for optical rotation*. Applied Physics Letters (2017), 111(2):023102.

9. Wen D., Chen S., **Yue F.**, Chan K., Chen M., Ardron M., Li K.F., Wong P.W.H., Cheah K.W., Pun E.Y.B., Li G., Zhang S., and Chen X. *Metasurface device with*

helicity-dependent functionality. Advanced Optical Materials (2016), 4(2): 321-327.

10. Wen D., **Yue F.**, Kumar S., Ma Y., Chen M., Ren X., Kremer P.E., Gerardot B.D., Taghizadeh M.R., Buller G.S., and Chen X. *Metasurface for characterization of the polarization state of light*. Optics Express (2015), 23(8): 10272-10281.

11. Chen X., Chen M., Mehmood M.Q., Wen D., **Yue F.**, Qiu C.W. and Zhang S. *Longitudinal multifocial metalens for circularly polarized light*. Advanced Optical Materials (2015), 3(9): 1201-1206.

Conference papers

Chen X, Wen D., and **Yue F**. *Unusual ultrathin optical devices: Metasurfaces make them practical*. Progress in Electromagnetic Research Symposium (PIERS), (2016), 2335-2335

Chapter 1 – INTRODUCTION

Metasurfaces, a novel kind of ultrathin optical components, can manipulate light properties by introducing abrupt phase change over the scale of subwavelength. They can be considered as arrays of subwavelength optical elements which perform efficient light-matter interaction to control the light properties. Considering the materials of nanostructures, this field are currently classified into two main categories: plasmonic metasurfaces [1-6] and dielectric metasurfaces [7-11]. These two categories have a common characteristic of geometry related interaction with light. Plasmonic metasurfaces are based on meta-atoms made from metallic nanostructures that exhibit effective electric and/or magnetic polarizabilities which are determined by their size, geometry, and orientation. In this context, optical responses are governed by the particle plasmon resonances they support. When applying an electric field to a metallic structure, the quasi-free electrons are displaced from their equilibrium positions with respect to the nuclei. The metallic structure is polarized in this case. Meanwhile, a restoring force arises to bring the system back toward equilibrium. In a time varying external field such as light, this collective motion can be viewed as a Lorentzian oscillator. This resonance is called surface plasmon resonance, which is the basis of light-matter interaction. Up to now various designs of nanostructures (such as rod antennas [2], V-shaped antennas[1], L-shaped antennas[12], and split-ring resonator [13]), and different types of metals (such as gold [14], silver [15], and aluminum [6]) are investigated to realize plasmonic metasurface with interesting optical functionalities. However, the transmissive plasmonic metasurfaces consisting of single layer of nanostructures suffer from low device efficiency. To overcome this problem, the reflective metasurface consisting of a gold ground layer, a silicon dioxide spacer layer and a top layer of nanostructures are developed to increase the efficiency [16]. Moreover, the three-layer design can give rise to a broad spectral response in the visible/near-infrared range.

In comparison with plasmonic metasurface, dielectric metasurfaces are made of high-refractive-index dielectric arrays, such as silicon [7, 10], andTiO_2 [17, 18], which provide substantial control over the local light scattering property. For a fixed geometric size, the difference between metallic and dielectric nanostructures is in the sign of the dielectric permittivity, which is negative for metals and positive for dielectrics [19]. When light with frequency below or near the bandgap frequency of the material hits a dielectric

nanostructure, both the magnetic and electric dipole resonances are excited. Dielectric metasurfaces offer the opportunity for reducing dissipative losses and achieving large resonant enhancement of both electric and magnetic fields [7]. By carefully optimizing the shape and size of the dielectric nanostructures, the conversion efficiency of transmissive dielectric metasurface can be higher than 80% [7, 10, 18].

With the interaction between metasurface and light field, wavefronts can be steered and shaped at subwavelength scale. The phase, polarization, and amplitude of light waves can be changed in unusual ways through metasurface. These features distinguish metasurfaces from conventional optical components which rely on light propagation over large optical path [1, 20, 21]. Meta-atoms are defined at the nanoscale, which can largely surpass the classical limits imposed by diffraction. The control over light beam at the nanoscale has led to a variety of relevant applications, including metasurface holograms, polarization dependent surface plasmon polaritons excitation, optical devices based on wavefront manipulation and nonlinear photonics. It also sets high expectations for applications of integrated circuits, optical computing, and medical technologies.

1.1 Review of Metasurfaces

1.1.1 Metasurface for phase and polarization control

Metasurfaces break the dependence on the propagation effect by introducing abrupt phase changes over the scale of the subwavelength. The first phase-gradient metasurface was demonstrated by Capasso's group [1]. A two-dimensional array of V-shaped antennas was used to produce a linear phase gradient distribution (Figure 1.1(a)). Anomalous reflection and refraction phenomena were observed by patterning periodic distributed nanoantennas, where each unit cell consists of eight different V-shaped antennas covering the whole [0 2π] phase range. They derived generalized laws of reflection and refraction from Fermat's principle and experimentally demonstrated an optical vertex by using gold nano-antennas (Figure 1.1(c)). Following this paper, this group demonstrated an out-of-plane anomalous reflection and refraction through anisotropic arrays of V-shaped gold antennas [22]. Here the phase changes are generated by the interaction of linearly polarized light beam with V-shaped meta-atoms that support two plasmonic eigenmodes with different resonant properties. Huang *et al*. subsequently investigated dispersionless phase discontinuous by using dipole antenna array [2] (Figure 1.1(b)). It should be noted that this is a completely different approach, which is based on the Pancharatnam-Berry phase [23-25]. Abrupt phase change is generated when a circularly polarized light beam is converted to the opposite polarization. A broadband optical vortex beam was experimentally demonstrated based on this configuration (Figure 1.1(d)). Metasurface has recently attracted considerable attention because of its ultrathin structure, subwavelength precision of wavefront manipulation, broadband performance, and easier fabrication. It provides unprecedented capabilities in the manipulation of phase and polarization. More and more metasurface devices have been developed, such as planar lenses [10, 20, 26, 27], axicons [3], waveplates [28, 29], beam splitters [30], vortex beam generators [1, 2, 12, 31], polarization measurement devices [14, 32], an invisibility cloak [33], optical rotation [34], and spectrum splitters [35].

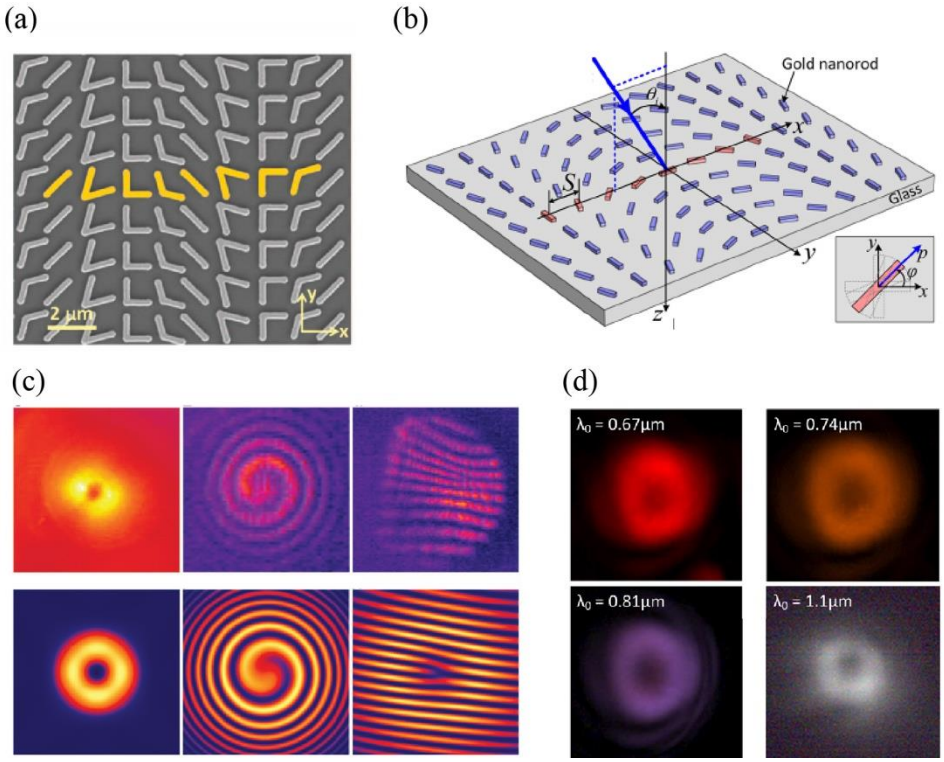

Figure 1.1 Plasmonic metasurfaces [1, 2]. (a) The SEM picture of a V-shape antenna array. The unit cell of the plasmonic interface compromises eight gold antennas of width 220 nm and thickness 50 nm. (b) Schematic illustrations of a representative dipole array. Each unit consists of eight gold rods with a rod to rod spacing of 400nm in both x and y directions. (c) Measured and calculated light distribution of an optical vortex with topological charge one, spiral patterns created by interference of the vortex beam and a co-propagating Gaussian beam, and interference patterns with a dislocated fringe. (d) Measured intensity distributions of the optical vortex beam at different wavelengths.

Dual-polarity plasmonic flat lens based on helicity-dependent phase discontinuities for circularly polarized light was demonstrated using metasurface [36]. By controlling the helicity of the input light, the positive and negative polarities are interchangeable in one identical flat lens. With special phase distribution, in-plane and out-of-plane refractions could also be manipulated. A beam can be focused in a 3D spot either in a real or virtual focal plane (Figure 1.2(a)). Figure 1.2(b) shows aberration-free ultrathin flat lenses and axicons at telecom wavelengths [3]. A radial distribution of phase discontinuities was introduced to generate respectively spherical wavefronts and non-diffracting Bessel beams at telecom wavelengths. According to the simulations, high numerical aperture lenses (NA=0.015 for the *f*=3 cm lens, NA=0.77 for the *f*=371 μm) were realised. These flat lenses described above are transmission-type. What's more, metasurface shows potential in the replacement of bulk refractive optical components with diffractive

property. Conventional diffractive optical components suffer from large chromatic aberrations due to the dispersion of the phase accumulated by light during propagation. Aieta *et al*. presented a planar lens without chromatic aberrations at three wavelengths [37]. This design is based on dielectric resonators which introduce a dense spectrum of optical modes to enable dispersive phase compensation (Figure 1.2(c)).

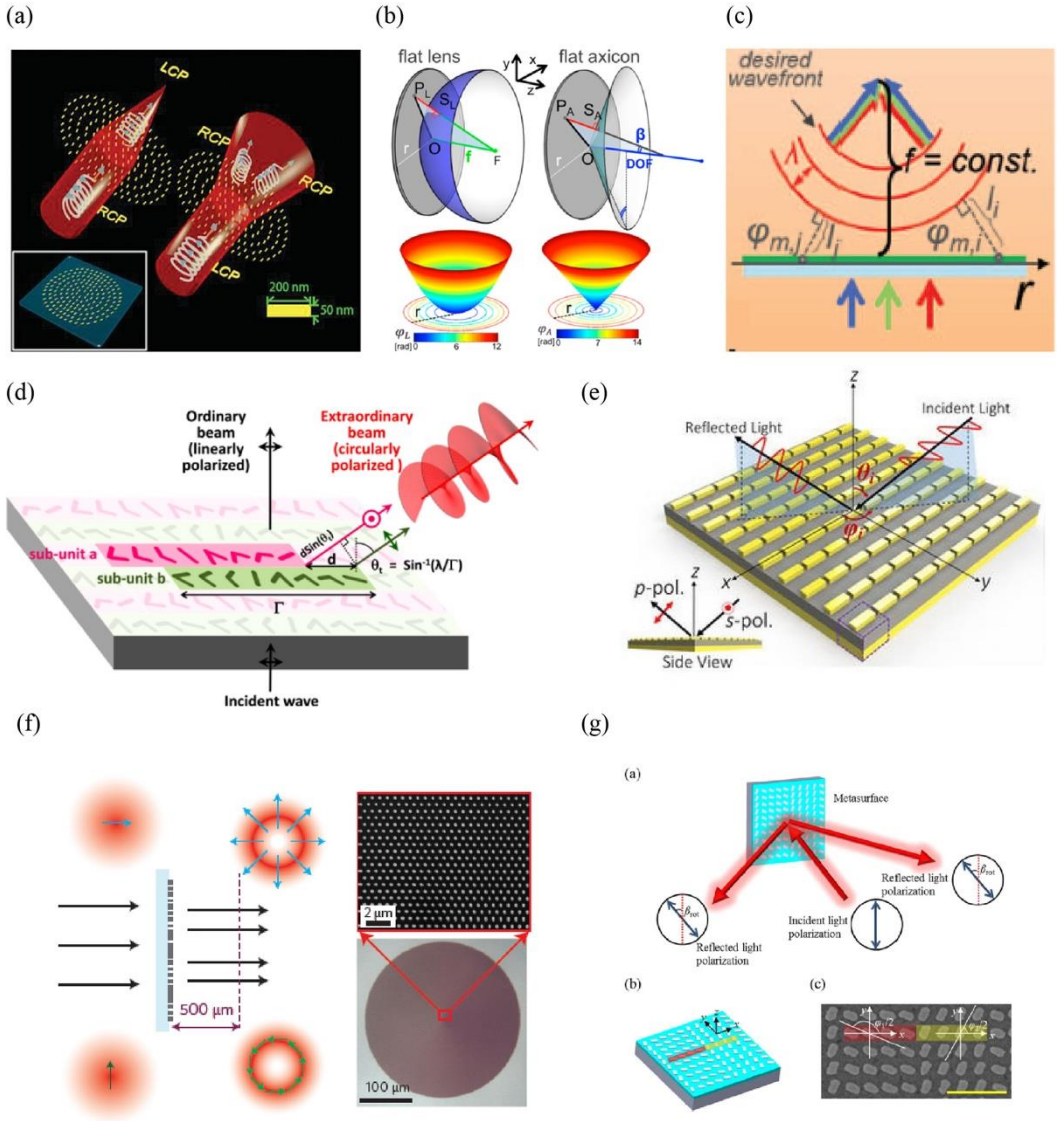

Figure 1.2. (a) Schematic of metalens with interchangeable polarity. The focusing properties of the same metalens can be switched between a convex lens and a concave lens by controlling the helicity of the incident light [36]. (b) Schematic of the design of flat lenses and axicons [3]. In order to focus a plane wave to a single point at a distance *f* from the metasurface, a hyperboloidal phase profile is imparted onto the incident wavefront. (c) Schematic of the achromatic metasurface. It consists of subwavelength space resonators to preserve the operation that different wavelengths of light share identical focal length [37]. (d) and (e) schematic design of quarter-wave plate[29] and

half-wave plate [38], respectively. (f) Dielectric metasurface for radially and azimuthally polarized cylindrical vector beams generation [7]. (g) Schematic of the polarization rotation by a metasurface.

Metasurfaces can be used not only for phase modulation, but also for polarization manipulation. Wave plates and polarizers have been successfully developed using metasurface approach. Figure 1.2(d) shows quarter-wave plate that generates light with a high degree of circular polarization (>0.97) from $\lambda = 5$ to 12 μm for arbitrary orientation of the linearly polarized incident light [29]. Figure 1.2(e) shows a broadband plasmonic metasurface-based half-wave plate [38]. A s-polarized wave incident from an angle of 135° is converted into a p-polarized wave upon reflection. Amir Arbabi, *et al*. demonstrated a dielectric metasurface for complete control of phase and polarization. Figure 1.2(f) shows the metasurface for radial and azimuthal polarized vector beams generation. However, the requirement for nanofabrication is very critical. Our group presented a method to realise optical rotation which originates from the additional phase difference between the two circular components (figure 1.2(g)) [34]. Metasurface not only offers degree of freedom in controlling the wavefront and polarization, but also exhibits the ability of spectrum splitting at visible and near infrared frequency with high conversion efficiency [35].

1.1.2 Metasurface for hologram generation

Another convincing example of phase control is metasurface hologram [6, 30, 35, 39-43]. The metasurface approach provides great flexibility in engineering the wavefront of light, and can be applied to generate holograms. Recently, a plethora of phase holograms based on metasurfaces have been investigated and presented (see Figure 1.3). Huang *et al*. have demonstrated phase-graded metasurface holograms with full 3D image reconstruction (Figure 1.3(a)) [21]. The required phase profile was calculated using a computer-generated holography algorithm similar to that used for holographic images using spatial light modulators. Almost simultaneously, Ni *et al*. [43] presented the ultrathin metasurface which provides phase modulation in the visible wavelength range for hologram generation (Figure 1.3(b)). It is worth noting that the conversion efficiency of hologram based on transmission-type metasurface is poor because of single-pass interaction between light beam and nanoantennas. To overcome the limitation, Huang *et al*. [6] and Zheng *et al*. [16] presented plasmonic meta-holograms with reflective-type

design which achieved multi-colour properties and higher efficiency (Figure 1.3(c)-(f)). Specifically, the concept introduced by Zhang and colleagues combines the superior phase controlling of geometric metasurfaces with reflect-arrays (arrays of metallic structures fabricated over a reflective surface) and yields a wide-angle reflective hologram with the efficiency of 80% (Figure 1.3(f)). The zeroth-order efficiency is extremely low. This structure also exhibits a broadband spectrum response over visible and near infrared wavelength range. These pave the way for putting metasurface hologram into practical application.

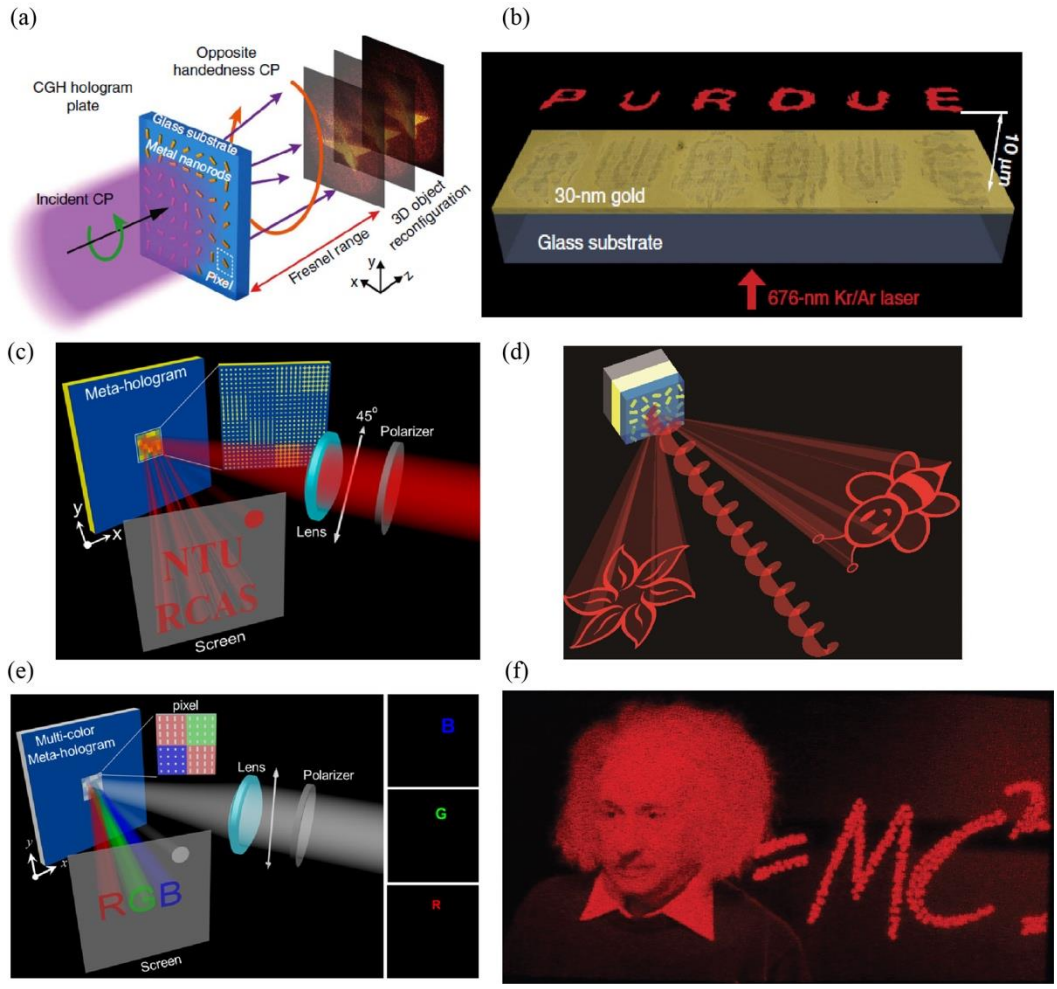

Figure 1.3. Examples of metasurface holograms (a) Hologram structure and reconstruction procedure. The reconfigured 3D models are designed to appear within the Fresnel range [21]. (b) The image of the word 'PURDUE' is obtained experimentally at a plane 10 μm above the metasurface hologram [43]. (c) Illustration of designed meta-hologram by Din Ping Tsai's group. The images 'NTU' and 'RCAS' can be reconstructed by linearly polarized light along the *x*- or *y*-direction, respectively. (d) Helicity multiplexed metasurface holograms [15]. (e) Illustration of the designed multi-colour

meta-hologram under illumination of linearly polarized light. (f) Experimentally obtained holographic images of Einstein's portrait captured by a camera in the far-field [16].

1.1.3 Surface plasmon polariton excitation using metasurface

Light can propagate at a metal-dielectric interface in the form of surface plasmon polaritons (SPP), which are hybrid waves of photons and charge oscillations sustained by the electrons near the interface [44-54]. Another exciting feature of plasmonic metasurfaces is the ability to control SPP over near field region [52, 55-60]. Conventional approaches for SPP excitation and modelling rely on bulky optical materials which lead to intrinsic limitations on the size and cost of devices. The latest work by several groups shows that metasurfaces can efficiently excite the SPPs. With the interaction between patterned plasmonic nanostructures and light, part of the radiative energy can convert to SPP. In this way, metasurface could be considered as a SPP emitter. Moreover, under special design of metasurface pattern, one can achieve polarization-dependent or wavelength–dependent unidirectional SPP excitation. Figure 1.4 (a) shows an approach of helicity dependent SPP excitation using a metasurface with phase discontinuity [55]. A circularly polarized light was normally incident on metasurface. The propagation direction of SPP wave could be controlled by changing the helicity of the incident light. Capasso's group also demonstrated a polarization-controlled surface plasmon polaritons [57]. They designed rectangle structure and circular structure to realise different SPP manipulation (Figure 1.4(b)). In 2015, Lin *et al.* reported a generic metasurface that can realise both wavelength and polarization multiplexing of SPP [61]. They used a straightforward method to reconstruct surface waves by compositing two patterns of different effective wavelengths or two separate patterns designed for orthogonal polarization states (Figure 1.4(c)). This mode-matching metasurface enables the access to the additional degree of freedom in surface optics, e.g. the transverse dimension of SPPs. In the same year, Wintz *et al*. [56] reported holographic metalens which engineered as switchable focal lens for SPP as shown in Figure 1.4 (d). This method overcomes some of the coupling and focusing issues for SPPs. The design strategy can be used to gain both wavelength and polarization tunability over the direction of SPP wave propagation. Most importantly, by recreating the wavefront of a point source it is feasible to focus SPP beams after coupling.

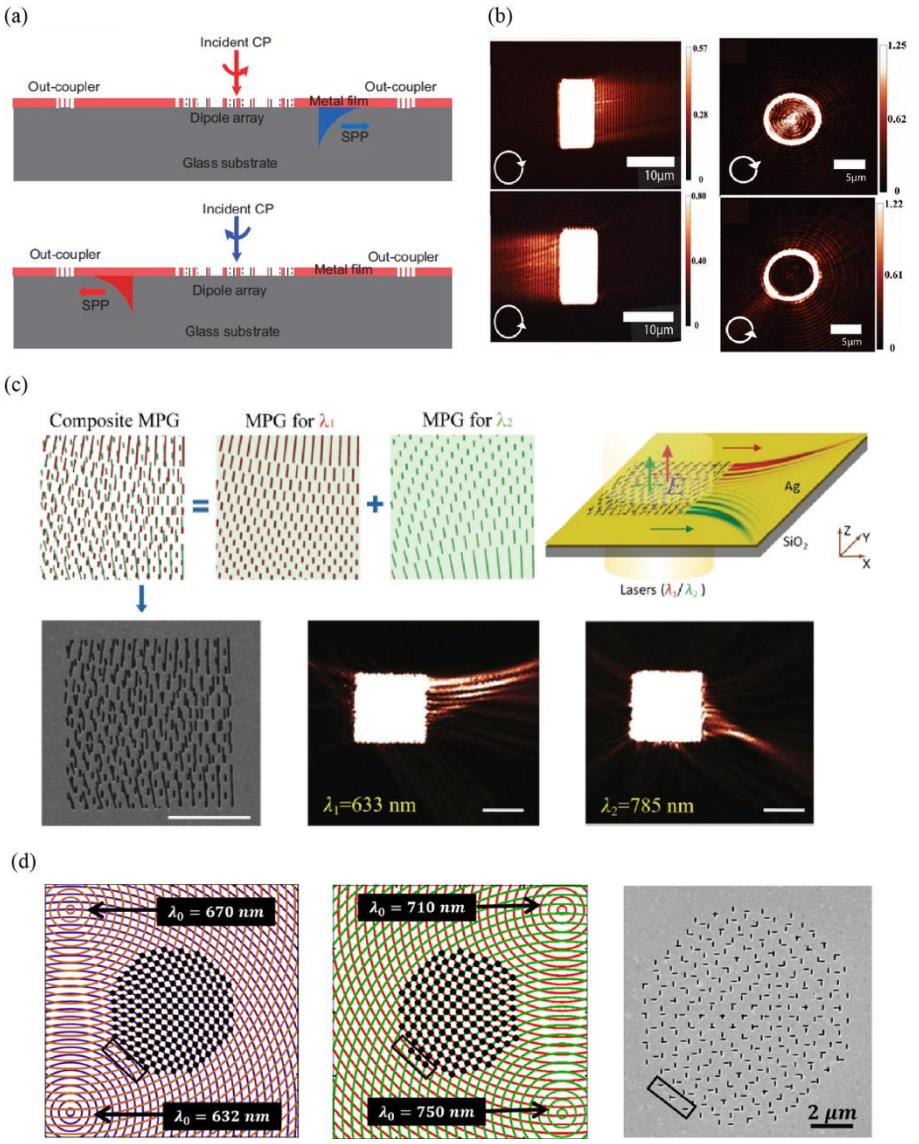

Figure 1.4. (a) Schematic of a unidirectional SPPs coupler [55]. The coupler consists of an array of rectangular apertures with spatially varying orientations on a metal film. The direction of propagation can be changed by altering the helicity of circularly polarized incident light. (b) NSOM images of the rectangle and circular structures under illumination from the back by both left handed and right handed circularly polarized light [57]. (c) Wavelength-multiplexing SPP with a mode-matching metasurface [61]. The composite metasurface is designed for the reconstruction of two excitation patterns of different effective wavelengths (613 nm and 770 nm at an Ag/air interface). (d) SPP metalens design [56]. The focal points for illuminating light wavelengths λ_0 = 632 and 670 nm are in the bottom and top left corners, respectively. Equivalent of panel but for the other two wavelengths (λ_0 = 710 nm and 750 nm) will be focused to the remaining corners.

1.1.4 Nonlinear metasurfaces

The metasurface provides the capabilities to control the phase of light not only in linear regime, but also in nonlinear regime [13, 62-66]. The local engineering of the nonlinear optical properties of light at nanoscale plays an important role in nonlinear photonics. More recently, nonlinear metasurfaces with tailored nonlinear response have provided new degrees of freedom in light-matter interaction with interesting uses in super-resolution imaging, performing efficient frequency conversion and optical control with greatly relaxed phase-matching conditions. Specially, the nonlinear Pancharatnam-Berry Metasurfaces, which consist of plasmonic nanoantennas with rotational symmetries, have the abilities to continuously control the local nonlinearity in the subwavelength range for the high-order harmonic generation. In 2015, Li *et al*. experimentally demonstrated nonlinear metasurface with spatially varying nonlinear polarizability for continuously phase control [62]. The nonlinear metasurface consisting of nanoantennas with rotational symmetries provides the phase control over the local nonlinearity. The basic principle is the nonlinear spin-rotation coupling of light. Based on the selection rules for harmonic generation under circularly polarized incident light, a nanostructure with *m*-fold rotational symmetry allows harmonic orders of $n = lm \pm 1$, where the "+" and "-" correspond to the harmonic generation of the same and opposite circular polarization in terms of that of the incident light, l is an integer (Figure 1.5(a)). In the same year, Keren-Zur *et al.* [13] demonstrated the nonlinear beam shaping by tailoring both the local phase and the amplitude of the nonlinear coefficients of metasurfaces. Figure 1.5(b) shows the illustration of the second harmonic vortex beam generation. Moreover, by carefully designing the shape and the orientation of the plasmonic nanostructures, the helicity and wavelength selective harmonic generation can also be realised due to the nonlinear spin-rotating coupling. Figure 1.5(c) shows the schematic and the experiment results of the spin and wavelength multiplexed linear and nonlinear holography [65].

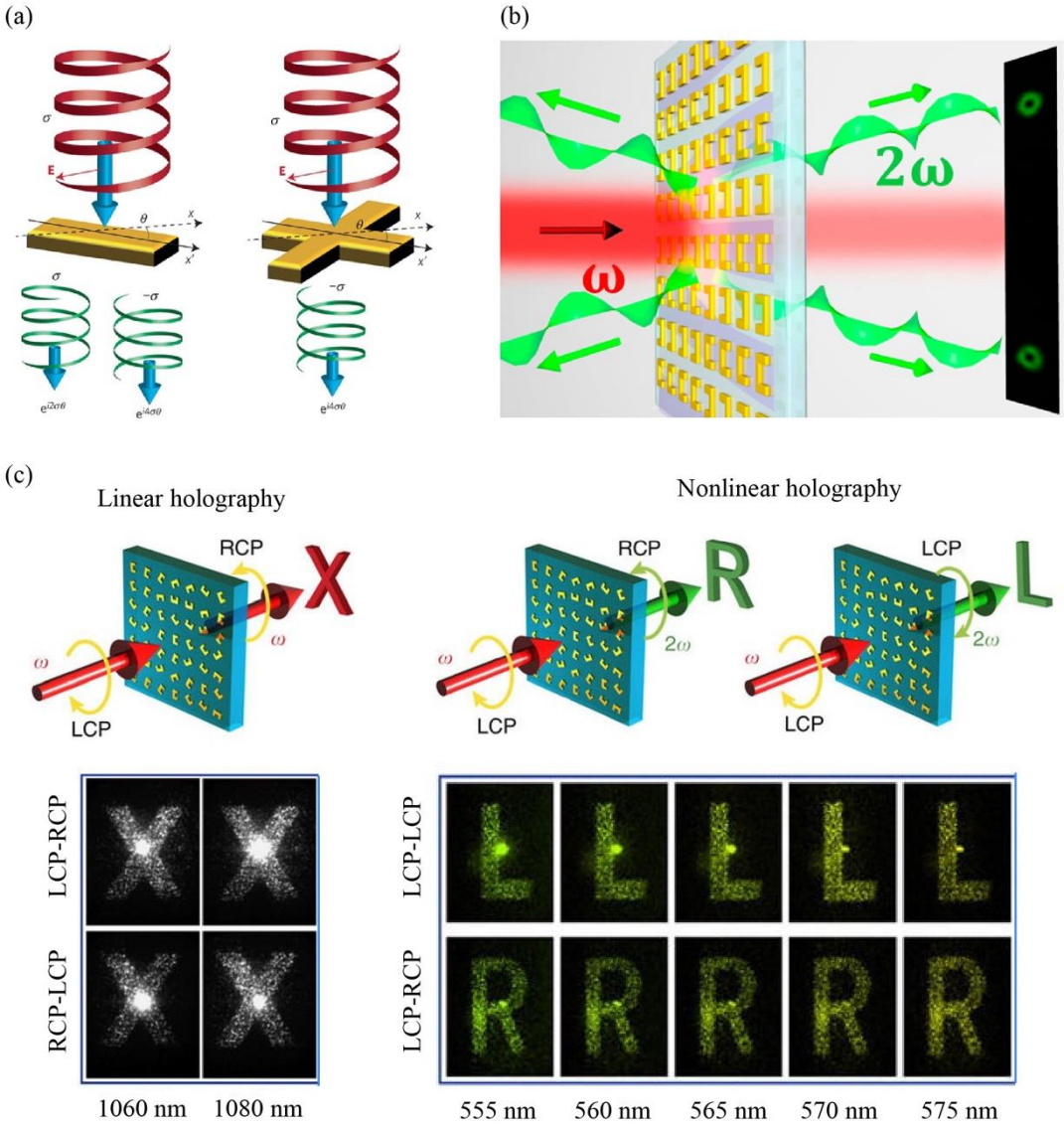

Figure 1.5. (a) Illustration of geometric phase controlled nonlinear nanostructures with C2 and C4 rotational symmetry [62]. (b) Illustration of nonlinear vortex beam generation[13]. (c) The schematic and experiment results of spin and wavelength multiplexed nonlinear holography [65].

The family of metasurfaces is actively growing. It is clear that there is a great deal of potential in this area that has yet to be realised. The research of optical metasurfaces will continue to be a very exciting field in the coming years, both in terms of fundamental scientific research and increasingly in the development of practical devices.

1.2 Thesis Overview

The thesis is organized as follows:

After a brief introduction about metasurface, we start to discuss the interaction between light and plasmonic nanostructure, and the geometric phase in Chapter 2. We build a theoretical model to analyse the conversion efficiency and the abrupt phase change due to the spin-rotation coupling. Then the fabrication process of plasmonic metasurfaces and numerical simulation for wavefront distribution are presented. The explanation of high efficiency and broadband performance of reflective metasurfaces is given in this chapter. The simulated and measured efficiency of metasurface devices are presented at the end of this chapter.

In subsequent chapters, we present the working principle of metasurfaces for phase and polarization control, and demonstrate in detail several novel metasurface approaches for various applications. In Chapter 3 we describe the application of metasurface holograms with polarization-controlled functionality. Then the simulated and experimentally obtained metasurface holograms are presented.

Chapter 4 describes our approach to generate and manipulate the orbital angular momentum of light by means of single metasurface device. We begin by introducing the orbital angular momentum (OAM) of light. A metasurface approach to generate multiple orbital angular momentum states is developed and the polarization controlled superposition of OAM states is theoretically analysed and experimentally realised.

In Chapter 5 we demonstrate the metasurface for polarization control and present two examples followed by simulated and experiment results. The first example is about vector vortex beam generation using metasurface. In second example, we propose and experimentally demonstrate a metasurface approach to control the transverse polarization profile of light beam, in which a high-resolution grayscale image can be encoded. The desired polarization profile originates from the superposition of two circularly polarized beams with opposite handedness and space-dependent phase difference emerging from a single metasurface.

In Chapter 6 we make a conclusion and discuss the possible directions of future research about metasurface.

Chapter 2 – PLASMONIC NANOSTRUCTURES AND GEOMETRIC PHASE

The metal structures with the size smaller than light wavelength have strong light enhancement due to the resonance between the electromagnetic field of light and the quasi-free electrons on the surface of the metal structures. The shape and size of the nanostructure affect the spectral selective light scattering and absorption, which provides the freedom to tailor the properties of the resulting light. In this chapter, we discuss the basic principle of plasmonic metasurface and analyse the optical properties of plasmonic nanostructures and the geometric phase. At the beginning of this chapter, the interaction of light with plasmonic nanostructures is briefly described. The Drude model and the Drude-Lorentz model are discussed to analyse the optical properties of metals. In the second part of this chapter, the abrupt phase shift (known as Pancharatnam-Berry phase) associated with the circular polarizations is introduced, which is the basis of geometric metasurface. The abrupt phase change provide the fundamental capability to control the properties of light field in a desirable manner. After that, the fabrication process of transmissive and reflective metasurface is presented. Finally, the conversion efficiency of two types of metasurface designs is analysed and simulated, and the experimentally measured results are presented and discussed.

2.1 The Interaction of Light with Plasmonic Nanostructures

2.1.1 Optical properties of metal nanoparticles

Most metals are opaque but highly reflecting; glass or pure water is transparent but weakly reflecting. The optical phenomena of the materials (e.g., reflection, transmission, and dispersion) are determined by the fundamental optical constants of microscopic structure of the matter. For example, the refractive index of a material depends on the polarizability of a single molecule and the number of molecules per unit volume [67].

To describe the optical properties of the materials, two sets of quantities are usually used, which are the complex dielectric function $\varepsilon = \varepsilon' + i\varepsilon''$ and the complex refractive index $\tilde{n} = n + ik$, respectively. Here ε' and ε'' are the real part and imaginary part of the complex relative permittivity. For the complex refractive index, the real part n is the refractive index and indicates the phase velocity, while the imaginary part k is the extinction coefficient and indicates the amount of attenuation during the electromagnetic wave propagating through the material. These two sets of optical properties are responsible for the interpretation of different optical phenomena. The reflection and transmission on an interface are analysed more simply with n and k, while the analysis of absorption and scattering by particles with subwavelength size is more simple by using ε' and ε''. The two sets of properties are related to each other, as given by

$$\varepsilon' = n^2 - k^2 \tag{1.1}$$

$$\varepsilon'' = 2nk \tag{1.2}$$

$$n = \sqrt{\frac{\sqrt{\varepsilon'^2 + \varepsilon''^2} + \varepsilon'}{2}} \tag{1.3}$$

$$k = \sqrt{\frac{\sqrt{\varepsilon'^2 + \varepsilon''^2} - \varepsilon'}{2}} \tag{1.4}$$

where we have assumed that the materials are non-magnetic, hence the relative permeability is close to 1.

A matter is formed from atoms which can be subdivided into nuclei and electrons. To analyse the optical properties of metals and understand the interaction of light and matter, some simple phenomenological models such as Drude model [68, 69]and Drude-Lorentz model [70, 71] were proposed and discussed, in which the nuclei and electrons are approximately treated as damped harmonic oscillators subject to the applied electromagnetic fields. The complex optical dielectric function of metals are related to their energy band structures. Electrons in metals at the top of the energy distribution can be excited into other energy and momentum states by photons with very small energies. Thus, they can be treated as quasi-free electrons, which refers to the intraband effects [67]. The optical response of a collection of quasi-free electrons can be obtained from the Lorentz harmonic oscillator model, in which the spring constant equal to zero. The Drude model or free-electron model can be deduced as

$$\varepsilon^{(D)}(\omega) = 1 - \frac{\omega_p^2}{\omega^2 + i\gamma\omega} \tag{1.5}$$

where γ is the damping constant, ω_p is the plasma frequency that refers to the oscillating resonant of the harmonic oscillator. In equilibrium, the centre of mass of the electrons and the centre of mass of the nuclei coincide. However, when illuminating an electromagnetic field on the matter, the centre of mass of the nuclei and the electrons shift with respect to each other. A Coulomb force arises to restore their position, initiating an oscillatory behaviour. The oscillating frequency is called the plasma frequency. The plasma frequency $\omega_p = \sqrt{\frac{Ne^2}{m\varepsilon_0}}$ is proportional to the electron density, where N is the number density of electrons, e stands for the electric charge, m is the standard mass of the electron, and ε_0 is the permittivity of free space. The plasma frequencies of gold (Au) [72], silver (Ag) [73] and aluminum (Al) [74] are given in Table 2.1.

Despite its applicability to metals such as aluminum, Drude model alone does not accurately describe the optical characteristics of many other metals. Moreover, the Drude model approximation is valid over a limited wavelength range [71]. Indeed, metals not only exhibits some quasi-free-electron type of behavior, which can be treated with the Drude theory, but also has a substantial bound-electron component, which refers to the

interband effects or bound-electron effects. The interband effect can be described by the simple semiquantum model resembling the Lorentz results for insulators:

$$\varepsilon^{(L)}(\omega) = \sum_{j=1}^{k} \frac{f_i \omega_p^2}{(\omega_j^2 - \omega^2) + i\omega\gamma_j} \tag{1.6}$$

where k is the number of oscillators with frequency ω_j and damping constant γ_j, f_j are weighting factors. By considering both the intraband (free-electron) and interband (bound-electron) transitions, the Drude model can be extended to the Drude-Lorentz model, which can broaden the range of validity of analytical approximations to metallic dielectric constants. The Drude-Lorentz model is expressed by

$$\varepsilon^{(D-L)} = 1 - \frac{f_0 \omega_p^2}{\omega^2 + i\omega\gamma_0} + \sum_{j=1}^{k} \frac{f_i \omega_p^2}{(\omega_j^2 - \omega^2) + i\omega\gamma_j} \tag{1.7}$$

In Figure 2.1, we compare the Drude and Drude-Lorentz models with experimental data for silver [75]. As illustrated on Figure 2.1, the Drude model is a valid model for the dielectric function of sliver over a limited wavelength range. Whereas, the Drude-Lorentz model provides an accurate fit with the real dielectric function of silver over the whole frequency range of interest.

Table 2.1 The plasma frequencies of Au, Ag and Al

	Au	Ag	Al
N	$5.90\times10^{28}\,\mathrm{m}^{-3}$	$5.85\times10^{28}\,\mathrm{m}^{-3}$	$1.8\times10^{29}\,\mathrm{m}^{-3}$
ω_p	$1.3\times10^{16}\,\mathrm{Hz}$	$1.37\times10^{16}\,\mathrm{Hz}$	$2.32\times10^{16}\,\mathrm{Hz}$

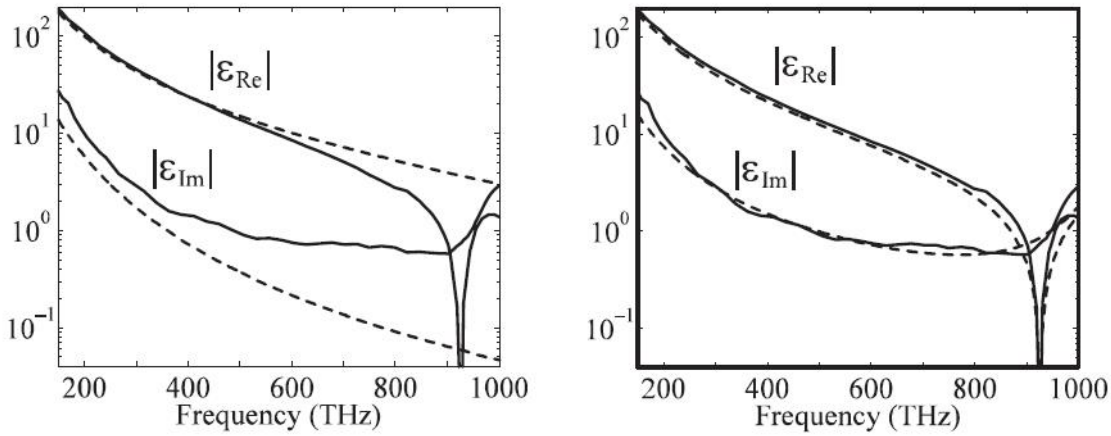

Figure 2.1. Real and imaginary part of the dielectric constant of silver at optical frequencies. The solid lines show experimental data [76]. The dashed lines show values calculated using (a) the Drude model, (b) the Drude-Lorentz model with five Lorentzian terms [71].

2.1.2 The far field scattering of metal nanostructure arrays

In the above section, the optical properties of bulk materials, especially the metal, are discussed. The light-matter interaction is successfully analysed in terms of Drude-Lorentz model. When the sizes of the metal solids fall into nanoscale regime, which are smaller than the wavelength of interest, unusual properties and physical phenomena arise due to the distinguished light-matter interaction in subwavelength scale. The striking example is the extraordinary optical transmission through subwavelength hole arrays [77]. In this section, the light-matter interaction of metal nanostructures arrays and the far field scattering are discussed.

Considering particles smaller enough compared to wavelength of the involved electromagnetic fields, the quasistatic approximation is adopted to simplify the calculation, which assumes the exciting field to be homogeneous and not retarded over the particle's volume. When a metallic nanoparticle is illuminated with an electromagnetic field (light), as shown in Figure 2.2, the conduction electrons on surface of the metal nanostructure will oscillate collectively and coherently caused by the oscillating electric field. The shift of the free conduction electrons with respect to the metal ion lattice produces a restoring local field between the two sides of the nanoparticle. The coherently shifted electrons of the metal particle together with the restoring field consequently generate an oscillator, and the oscillating frequency is determined by the

size and shape of the nanoparticle, the dielectric function of the metal and the surrounding environment. The collective oscillation of the electrons is called the surface plasmon resonance (SPR) [78].

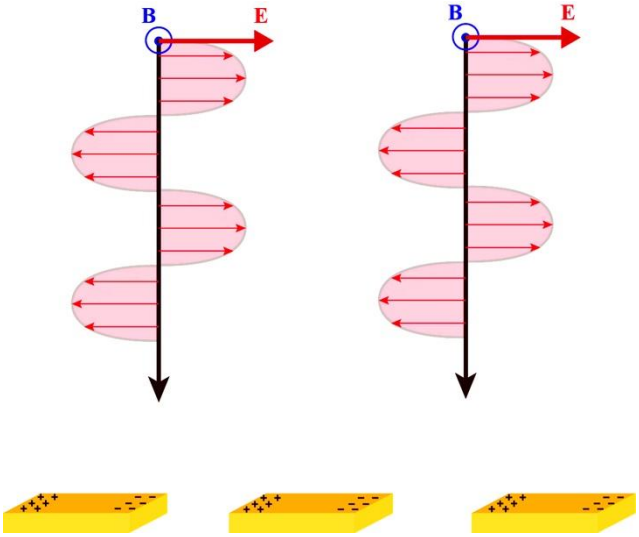

Figure 2.2. Schematic of plasmon oscillation on metal nanoparticles irradiated by an electromagnetic field.

To theoretically analyse the interaction of light with small particles, Gustav Mie developed a set of theory that described the scattering and absorption spectral performance of spherical particles with arbitrary size [67]. The Mie theory plays a fundamental role in understanding the physics of light-nanoparticle interaction in nanophotonic field. Since it is the only simple and exact solution to Maxwell's equations that is relevant to the size and shape of particles. In addition to the material, shape control of nanoparticles provides more degrees of freedom to manipulate the optical properties, which has significant impact on science and technology. To generalize the concept, Gans extended Mie's theory to the prolate and oblate spheroidal particles averaged over all orientations [79] . In this thesis, we focus on the gold rectangular solids which have long and short axes. The thickness of the rectangular solids are quite small in comparison with the long and short axes. For this shape of gold nanoparticles, the surface plasmon resonance has two modes: one longitudinal mode along the long axis of the particle and a transverse mode perpendicular to the first.

When an electric field is applied on a rectangular metal solid, the resulting surface charges of opposite sign on the opposite surface elements of the nano-strip generate an electric dipole (see Figure 2.2). The Polarizability α determines the dynamical response of the

metal nano-strip to the external oscillating electric fields. It is defined as the ratio of the induced dipole moment of nano-strip $\vec{\mathbf{P}}$ to the electric field $\vec{\mathbf{E}}$ as

$$\vec{\mathbf{P}} = \alpha \vec{\mathbf{E}} \tag{1.8}$$

According to the generalized Mie's theory extended by Gans, the polarizabilities of the metal nano-strip along the long and short axes can be given by [80]

$$\alpha_{long} = V \frac{\varepsilon_m - \varepsilon_s}{\varepsilon_s + A_{long}(\varepsilon_m - \varepsilon_s)} \tag{1.9}$$

$$\alpha_{short} = V \frac{\varepsilon_m - \varepsilon_s}{\varepsilon_s + A_{short}(\varepsilon_m - \varepsilon_s)} \tag{1.10}$$

where V is the volume of the nano-strip, ε_m and ε_s are the frequency dependent dielectric functions of the metal and the surrounding material, respectively, A_{long} and A_{short} are the shape constants of the long and short axes, which depend on the aspect ratio of the two axes [80]. For spherical particles with radius of a, the volume is $V = \frac{4}{3}\pi a^3$ and the shape constants $A_{long} = A_{short} = \frac{1}{3}$.

The absorption and scattering process of the metal nano-strip are described by the absorption cross-section C_{abs} and the scattering cross-section C_{sca} [74].

$$C_{abs} = k\,\mathrm{Im}(\alpha) \tag{1.11}$$

$$\mathrm{C}_{sca} = \frac{k^4}{6\pi}|\alpha|^2 \tag{1.12}$$

$\mathrm{Im}(\alpha)$ denotes the imaginary part of the polarizability and $|\alpha|$ is the modulus of the polarizability. k is the wave number. From equation (2.9-2.12), it can be concluded that the absorption and scattering of an incident light with electric field parallel to the long axis are different from that of the light with electric field parallel to the short axis.

Moreover, the absorption and scattering efficiency are determined by the wavelength dependent dielectric function of the metal and surrounding material, together with the size and the shape of the metal nano-strip.

If we assume the metal nano-strip is illuminated by an *x*-polarized plane wave $E_0 e^{(ikz-i\omega t)}\vec{\mathbf{e}}_x$ or *y*-polarized plane wave $E_0 e^{(ikz-i\omega t)}\vec{\mathbf{e}}_y$, the electric charges on the surface of the nano-strip are set into oscillatory motion along *x* direction or *y* direction by the electric field of the incident wave, respectively (see Figure 2.3(a) and (c)). Larmor's theorem of electromagnetism states that accelerated charges generate electromagnetic radiation [81]. Accelerated electric charges radiate electromagnetic energy in all directions. Note that, the excited elementary charges may transform part of the incident electromagnetic energy into other forms in addition to reradiating electromagnetic energy, such as thermal energy. First, we consider the case of *x*-polarized incident plane wave. The SPR along the long axis of the nano-strip has a dipole moment $\vec{\mathbf{P}} = \alpha E_0 e^{-i\omega t}\vec{\mathbf{e}}_x$. As shown in Figure 2.3(b), the reradiating wave or scattering wave at point *G* in far field can be written as follow [67]

$$\vec{\mathbf{E}}_{s-long} = E_0 \frac{e^{ikr}}{-ikr}\frac{ik^3}{4\pi}\alpha_{long}\vec{\mathbf{e}}_r \times (\vec{\mathbf{e}}_r \times \vec{\mathbf{e}}_x) \qquad (\text{kr} >> 1) \qquad (1.13)$$

where *r* is the distance from zero to the point *G*, $\vec{\mathbf{e}}_r$ is the unit vector. Here the time-dependent factor $e^{-i\omega t}$ is omitted. Analogously, for the case of *y*-polarized incident plane wave (see Figure 2.3(c) and (d)), the complex amplitude of scattering wave at point *G* can be given by

$$\vec{\mathbf{E}}_{s-short} = E_0 \frac{e^{ikr}}{-ikr}\frac{ik^3}{4\pi}\alpha_{short}\vec{\mathbf{e}}_r \times (\vec{\mathbf{e}}_r \times \vec{\mathbf{e}}_y) \qquad (\text{kr} >> 1) \qquad (1.14)$$

Therefore, from Eq. (2.13) and (2.14) we can see that the amplitude of the scattering wave is determined by the polarizabilities α_{long} and α_{short}. The polarizabilities depend on the wavelength-dependent dielectric function of metal and the shape of the nano-strip. Therefore, we can tailor the scattering properties by adjusting the shape of the nano-strip. If the polarization state of the incident plane wave has both *x* and *y* components, such as circular polarization, the amplitude of the scattering wave at point *G* is the superposition

of two scattering waves caused by the SPR along the long axis and short axis of the nano-strip, respectively.

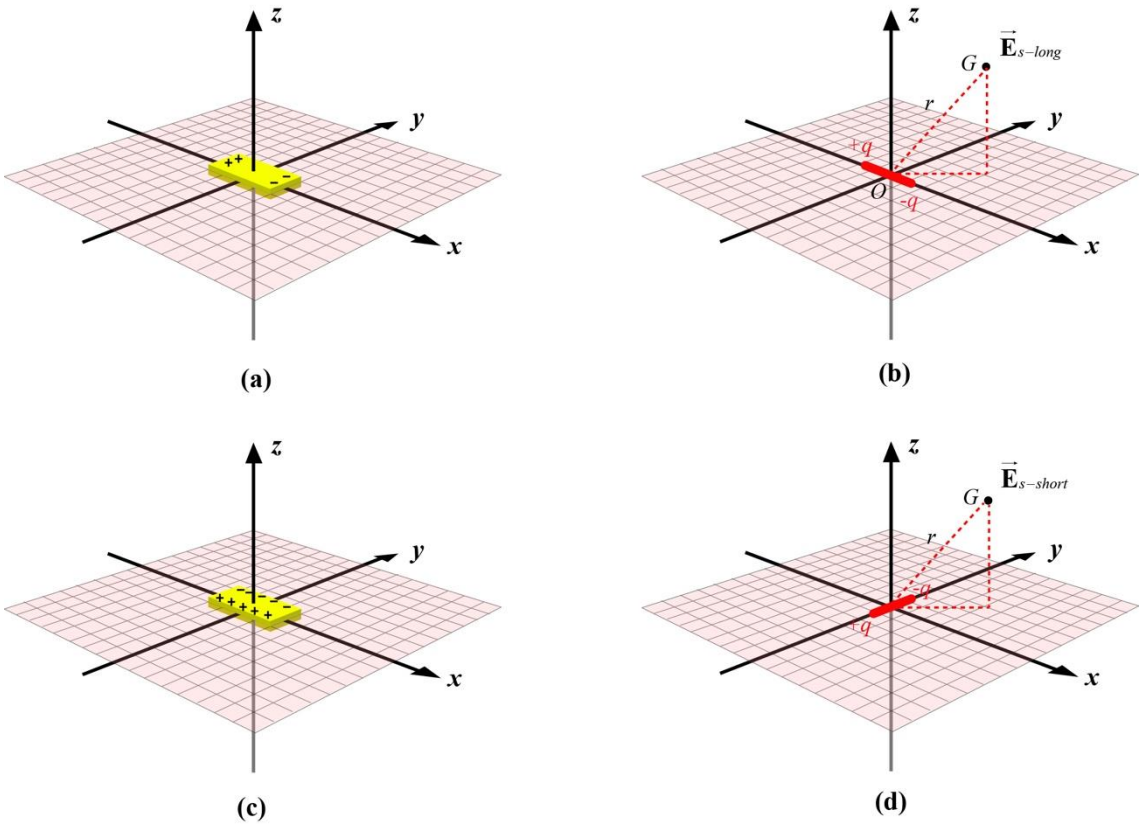

Figure 2.3. Schematic of surface plasmon resonance along long axis and short axis. (a) and (b) illustrate the dipole moment along the long axis of the metal nano-strip that arises when illuminated a *x*-polarized plane wave. (c) and (d) show the dipole moment along the short axis that arises under the illumination of *y* polarized plane wave.

For a single nano-strip, the resonance phenomenon and the far field scattering are determined by the shape and size of the nano-strip, together with the frequency-dependent dielectric function of nano-strip and the surrounding materials. For metal nan-strips arranged in regular two-dimensional patterns, the far field performance depends not only on the surface plasmon resonance of single nanoparticle, but also on the interaction between nanoparticles [82, 83]. The interaction among nanoparticles can be divided into near-field coupling which is relevant to the nearby particles with short distance and far-field collective interaction. This phenomenon has been theoretically discussed by Meier[84], and experimentally investigated by Lamprecht [83]. For grating constants d in the range of light wavelength of interest λ, there are four relevant domains as shown in Figure 2.4. When the interparticle distance d is smaller than a critical grating constant

d_c, both the evanescent field and scattering field are excited by the nanoparticle arrays (see Figure 2.4(a)). If the distance d exceeds the critical grating constant d_c, the scattering field arises because the evanescent field changes to radiative mode. For $d_c < d < \lambda$, only the zeroth scattering order is allowed and the direction of the scattering wave is along the transmission direction (see Figure 2.4(b)). For $d = \lambda$, both the zeroth and first grating order exist. The first grating order is emitted parallel to the grating plane as shown in Figure 2.4(c). For $d > \lambda$, the incident light is scattered at defined angles, which is analog to the light diffraction from a grating.

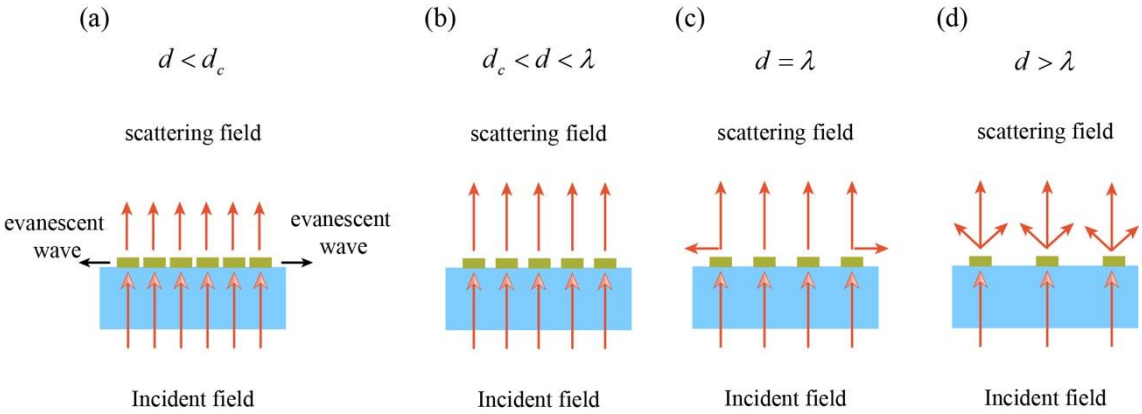

Figure 2.4. Four domains of the grating constant concerning the near field coupling and far-field scattering.

2.2 Conversion Efficiency and Geometric Phase

The geometric metasurface consisting of plasmonic nano-strip arrays provides the opportunity to manipulate the phase and polarization of light at the nanoscale. The geometry of the nano-strip is identical, but the orientation angle is space-dependent. When a circularly polarized light illuminating the nano-strip, part of the incident light will be converted to the opposite circular polarization. More importantly, the converted part will acquire an abrupt phase which is relevant to the orientation angle of the nano-strip. Thus, by engineering the nano-strip arrays with space-dependent orientation angles, the phase and wavefront of the light could be tailored in subwavelength scale. In this section, we use the Jones matrix calculus to analyse the conversion efficiency of the metasurface consisting of nano-strips. After that, the geometric phase, which arises during the interaction of circularly polarized light with rotated nano-strip, is discussed.

2.2.1 The conversion efficiency

In the past, many mathematical tools were developed to treat the physical problems regarding light and optical components, such as the set of Stokes parameters and Mueller matrices, and the set of Jones vector and Jones matrices [85]. Table 2.2 shows the differences between the two sets of mathematic tools. The Stokes parameters and the corresponding Muller matrices can describe any polarization state ranging from completely polarized light to completely unpolarized light. But they are more complicated than Jones vector and Jones matrices. The Jones vector is suitable for the treatment of completely polarized light. In this thesis, we shall deal primarily with completely polarized waves. Therefore, we use the Jones vector and the Jones matrices to describe the polarized light of interest and the transformation of polarization after the nano-strip, respectively. The plane-wave components of the optical field in terms of complex quantities can be written as

$$E_x(z,t) = E_{0x} e^{i(\omega t - kz + \delta_x)} \tag{1.15}$$

$$E_y(z,t) = E_{oy} e^{i(\omega t - kz + \delta_y)} \tag{1.16}$$

We suppress the propagator $\omega t - kz$ and arrange Equation (2.15) and (2.16) in a 2×1 column matrix:

$$E = \begin{bmatrix} E_x \\ E_y \end{bmatrix} = \begin{bmatrix} E_{0x} e^{i\delta_x} \\ E_{0y} e^{i\delta_y} \end{bmatrix} \tag{1.17}$$

Equation (2.17) is the Jones vector. First, we assume a right-handed circularly polarized (RCP) light is illuminated onto a nano-strip. It should be noted that there are two definitions of circular polarization from different literatures. In this thesis, we adopt the definition from the reference book [85] in which the polarization is right-handed when looking in the direction from which the light is coming, the end point of the electric vector would appear to describe the ellipse in the clockwise sense. The normalized Jones vector of the RCP is $E_{in} = \begin{bmatrix} 1 \\ i \end{bmatrix}$. We first consider the case that the long axis of the nano-strip is parallel to the *x* axis, and the short axis is parallel to the *y* axis. As discussed in above section, the polarizabilities for the long and short axis of nano-strip are different due to asymmetric shape. Therefore, the electric field vibration along the long and short axes of the nano-strip experiences different scattering and phase shift. Considering the nano-strip is sufficiently small in comparison with the wavelength, it is reasonable to assume that the absorptions of electric fields parallel to the long and short axes are same.

Table 2.2 The differences between the set of Stokes parameters & Muller matrices, and the set of Jones vector & Jones matrices

	Jones vector	Jones matrices	Stokes parameters	Mueller matrices
The dimensions of the row and	2×1	2×2	4×1	4×4
Applicable targets	Polarized light	Optical components	Polarized and unpolarized light	Optical components

When a RCP light is illuminated on the nano-strip, the *x* and *y* components experience different phase delay. The nano-strip is similar as a retarder (phase shifter), and the Jones matrix can be written as $J_{(\varphi)} = \begin{bmatrix} e^{i\varphi/2} & 0 \\ 0 & e^{-i\varphi/2} \end{bmatrix}$, where φ is the total phase shift between *x* and *y* components. At the beginning, we consider the case that the *x* and *y* direction are parallel to the long and short axes, respectively. For the case of rotated nano-strip, it is

analysed on the following section. The Jones vector specifying the emerging field is obtained when E_{in}^{RCP} is multiplied by $J_{(\varphi)}$. This gives

$$E_{out} = J_{(\varphi)} \bullet E_{in}^{RCP} = \begin{bmatrix} e^{i\varphi/2} & 0 \\ 0 & e^{-i\varphi/2} \end{bmatrix} \begin{bmatrix} 1 \\ i \end{bmatrix} = \begin{bmatrix} \cos\frac{\varphi}{2} + i\sin\frac{\varphi}{2} \\ i(\cos\frac{\varphi}{2} - i\sin\frac{\varphi}{2}) \end{bmatrix} \tag{1.18}$$
$$= \cos\frac{\varphi}{2}\begin{bmatrix} 1 \\ i \end{bmatrix} + i\sin\frac{\varphi}{2}\begin{bmatrix} 1 \\ -i \end{bmatrix}$$

From Eq. (2.18) we find that the emerging field consists of two parts. The first part has the same circular polarization with the incident light, which refers to the non-converted light, the second part has the opposite circular polarization, which is the converted light. The ratio between these two parts is only determined by the total phase shift φ. When $\varphi = \pi$, all the input light is converted to the light with opposite circular polarization. This coincides with the half-wave plate. It is well known that a half-wave plate producing a phase delay of π between the light components parallel and perpendicular to the optical axis, leads to fully convert a circularly polarized beam into the oppositely polarized one in transmission. Note that there is a phase delay of $\frac{\pi}{2}$ between the converted and non-converted field, which is manifested by the factor *i* on the second term of Equation (2.18). Similarly, the Jones vector of emerging field under the illumination of left-handed circularly polarized (LCP) light $\begin{bmatrix} 1 \\ -i \end{bmatrix}$ can be given as

$$\mathrm{E}_{out} = \cos\frac{\varphi}{2}\begin{bmatrix} 1 \\ -i \end{bmatrix} + i\sin\frac{\varphi}{2}\begin{bmatrix} 1 \\ i \end{bmatrix} \tag{1.19}$$

From Eqations (2.18) and (2.19), we can conclude that the conversion efficiency of geometric metasurface consisting of metal strip arrays depend on the phase retardation between the SPR modes along the long and short axes of the strips. When the phase retardation is close to π, the conversion efficiency is close to 100%.

2.2.2 The geometric phase

We now consider the passage of circularly polarized light through the rotated nano-strip using the Jones formalism. The Jones matrix for the rotated nano-strip with rotation angle θ can be deduced using the familiar rotation transformation [85], namely,

$$J_{(\varphi)}^{(\theta)} = R_{(-\theta)} J_{(\varphi)} R_{(\theta)} \tag{1.20}$$

where $R_{(\theta)}$ is the rotation matrix:

$$R_{(\theta)} = \begin{bmatrix} \cos\theta & \sin\theta \\ -\sin\theta & \cos\theta \end{bmatrix} \tag{1.21}$$

Then we find that the Jones matrix for the rotated nano-strip can be deduced by carrying out the matrix manipulation of Eqation (2.20), which is given by

$$J_{(\varphi)}^{(\theta)} = \begin{bmatrix} \cos\frac{\varphi}{2} + i\sin\frac{\varphi}{2}\cos 2\theta & i\sin\frac{\varphi}{2}\sin 2\theta \\ i\sin\frac{\varphi}{2}\sin 2\theta & \cos\frac{\varphi}{2} - i\sin\frac{\varphi}{2}\cos 2\theta \end{bmatrix} \tag{1.22}$$

We assume a RCP light beam $\begin{bmatrix} 1 \\ i \end{bmatrix}$ is illuminated onto the rotated nano-strip, the Jones matrix of the emerging light can be written as

$$\begin{aligned} E_{out}' = J_{(\varphi)}^{(\theta)} \bullet \begin{bmatrix} 1 \\ i \end{bmatrix} &= \begin{bmatrix} \cos\frac{\varphi}{2} + i\sin\frac{\varphi}{2}\cos 2\theta & i\sin\frac{\varphi}{2}\sin 2\theta \\ i\sin\frac{\varphi}{2}\sin 2\theta & \cos\frac{\varphi}{2} - i\sin\frac{\varphi}{2}\cos 2\theta \end{bmatrix} \bullet \begin{bmatrix} 1 \\ i \end{bmatrix} \\ &= \cos\frac{\varphi}{2}\begin{bmatrix} 1 \\ i \end{bmatrix} + i\sin\frac{\varphi}{2} e^{i2\theta} \begin{bmatrix} 1 \\ -i \end{bmatrix} \end{aligned} \tag{1.23}$$

From the second term of Equation (2.23), we find an interesting thing that the converted light acquires an abrupt phase 2θ introduced by the rotated nano-strip. The abrupt phase is known as geometric phase or Pancharanam-Berry phase [2, 24, 25]. Similarly, for the case of LCP light, the output light can be given as

$$E_{out}' = \cos\frac{\varphi}{2}\begin{bmatrix}1\\-i\end{bmatrix} + i\sin\frac{\varphi}{2}e^{-i2\theta}\begin{bmatrix}1\\i\end{bmatrix} \tag{1.24}$$

From Equations (2.23) and (2.24), we are led to the important conclusion that by rotating the nano-strip, the phase of the output light can be manipulated in an easy and efficiency manner. Moreover, the geometric phase is independent on the wavelength. The array of nano-strips with space-dependent rotation angles, namely plasmonic metasurface, provides the ability to control the phase and even the polarization of the light due to the light-matter interaction and rotation-determined abrupt phase change. The advantages of high resolution and the miniature size make the plasmonic metasurface for a plenty of applications, such as lensing, hologram, ultrathin waveplate, spin-hall effect, invisibility cloak, etc.

2.3 The Generalized Snell's Law

In above section, we have described the abrupt phase change of the light introduced by the rotated nano-strip. In this section, we will give an example to demonstrate the robustness of the metasurface. In the following chapters, more applications including hologram, vortex beam generation, and imaging are presented and analysed.

Reflection and refraction refer to optical surface phenomena which occur when waves pass through an interface between two media with different refractive indices. The surface phenomena are governed by the law of conservation of energy and momentum. The direction of reflected and refracted waves is determined by Snell's Law. Considering a metasurface with nanorod structures in array with a lattice constant and a constant orientation angle step along one direction. The metasurface can be treated as an anisotropic interface between two different media. The plasmonic nanostructures introduce abrupt phase changes to the involved beam rays. When a circularly polarized light beam passes through the metasurface, Snell's law becomes inapplicable because of the special characteristic of the interface. Then the Generalized Snell's Law was proposed and demonstrated by Yu, et al. from Capasso's group [1] and Huang, et al. from Shuang Zhang's group [2]. They derived the Generalized Snell's Law with considering the abrupt phase changes at the interface. The Generalized Snell's Law of refraction and reflection are given by:

$$\begin{cases} n_t \sin(\alpha_t') - n_i \sin(\alpha_i) = \dfrac{\lambda_0}{2\pi} \dfrac{d\Phi}{dx} \\ \sin(\alpha_r') - \sin(\alpha_i) = \dfrac{\lambda_0}{2\pi n_i} \dfrac{d\Phi}{dx} \end{cases} \tag{1.25}$$

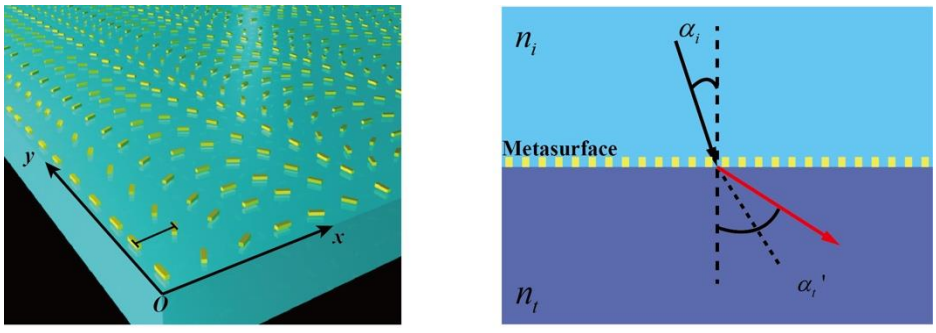

(a) (b)

Figure 2.5. (a) The nano-strip arrays with spatial-dependent orientation angles. (b) The anomalous refraction of the Generalized Snell's law.

From Eq. (2.25), we can see that the refraction and reflection angle are determined by incident angle together with the phase gradient $\frac{d\Phi}{dx}$. The phase gradient can be realised by gradually rotating the nano-strip arrays with certain angle step along one direction as shown in Figure 2.5(a) and (b). It should be mentioned that the phase gradient is dependent on the helicity of the incident light.

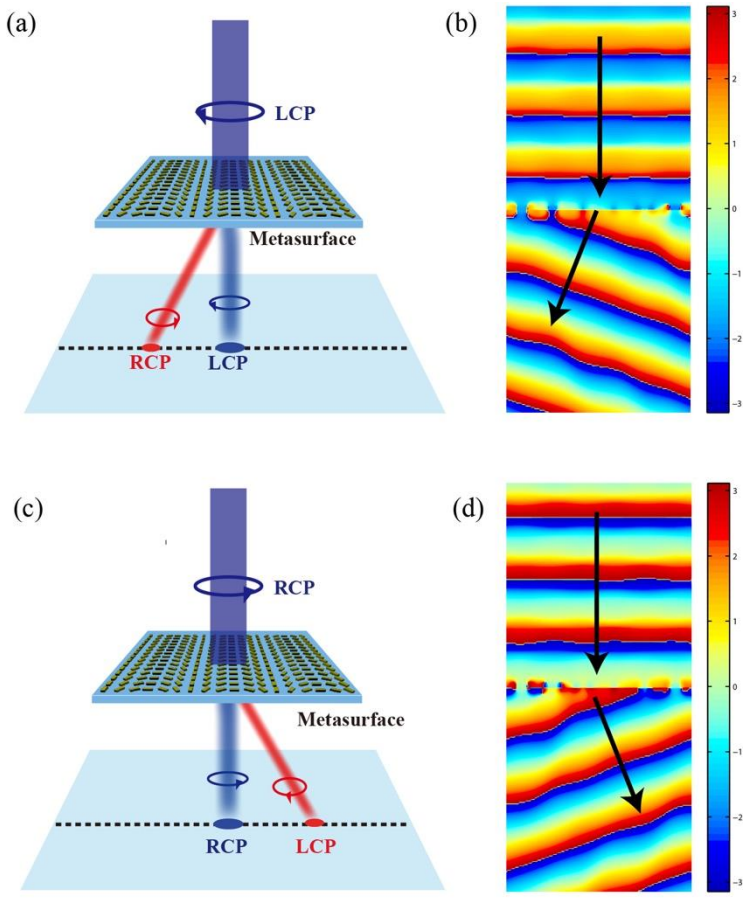

Figure 2.6. Schematics of anomalous refraction and the simulated phase distributions of both the input light and the refracted light by full wave simulation using CST microwave studio. (a) Schematics of anomalous refraction for the left-handed circularly polarized (LCP) light. (b) The simulated phase distribution for the case of LCP incident light. (c) Schematics of anomalous refraction for the right-handed circularly polarized (RCP) light. (d) The simulated phase distribution for the case of RCP incident light.

Firstly, we assume a LCP light beam is incident onto the phase gradient metasurface as shown in Figure 2.6(a). Part of the incident light is converted and the wavefront is tailored

due to the rotation-dependent abrupt phase change. We carried out the simulation of the refraction using Full 3D finite-difference time-domain CST Microwave Studio. One period of metasurface with six gold nano-strips is modelled at periodic boundary condition. The rotation angle step is $30°$ and the corresponding phase difference between two neighbouring nano-strips is $\frac{\pi}{3}$. Therefore, the abrupt phase changes in one lattice cover from 0 to 2π. A LCP light beam is normal incident onto the gold structures. The anomalous refraction is clearly observed from the wavefront distribution illustrated in Figure 2.6(b). For the case of right-handed circularly polarized light, the refraction direction is flipped because of the opposite sign of the phase difference for the opposite helicity. The schematic and the simulation of the wavefront distribution are shown in Figure 2.6(c) and (d).

2.4 Fabrication Process of Plasmonic Metasurface and The Efficiency.

The standard electron-beam lithography and lift-off process are used to fabricate the plasmonic metasurface. Firstly, a ITO-coated glass substrate is cleaned in Acetone and isopropyl alcohol (IPA) with ultrasound, respectively. Then a thin layer of positive resist PMMA (polymethyl methacrylate) 950 A2 which is sensitive to the electron beam, is spin-coated on the substrate. The spin speed of the spinner is 1000 rpm with 60 secs, which will result a PMMA layer with thickness of 120 nm. After that, the PMMA coated substrate is baked on hotplate at 180 ^{o}C for 5 mins.

The nanopatterns are designed and plotted using MATLAB, and saved as txt file. Then the txt file is loaded to the E-beam writer (Raith PIONEER). The nanopatterns are defined on the PMMA resist using E-beam writer. After the exposure, the sample is developed in the developer (Methyl isobutyl ketone (MIBK): IPA = 1:3) for 45 secs following by IPA (stopper) for 45 secs. A gold layer with thickness of 30 nm is deposited on the sample using electron-beam evaporator. The vacuum of the chamber during deposition is 4×10^{-6} mbar. Finally, the gold nanopatterns are realised after lift-off process. The whole process is presented in Figure 2.7. Figure 2.8 shows the scanning electron microscope (SEM) images of one fabricated sample.

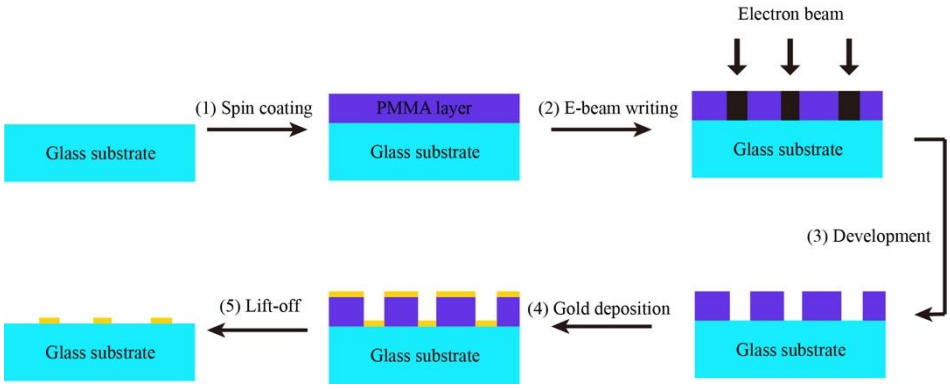

Figure 2.7. Fabrication process of gold nanopatterns.

The performance of this plasmonic metasurface is characterized and the conversion efficiency is measured. Before that, it is necessary to give the parameters of this metasurface. The size of nano-strip is 200 nm length by 80 nm width, and the thickness of the pattern layer is 30 nm. The distance between two neighbouring nano-strips is 300 nm. The rotation angle step is 30 ° . Because of the phase gradient generated by the

metasurface, the converted beam is deflected away from the non-converted part. It is easy to measure the power of the converted beam and the incident beam at different wavelengths. The conversion efficiency is defined as the ratio of the power of the converted beam and the total incident beam.

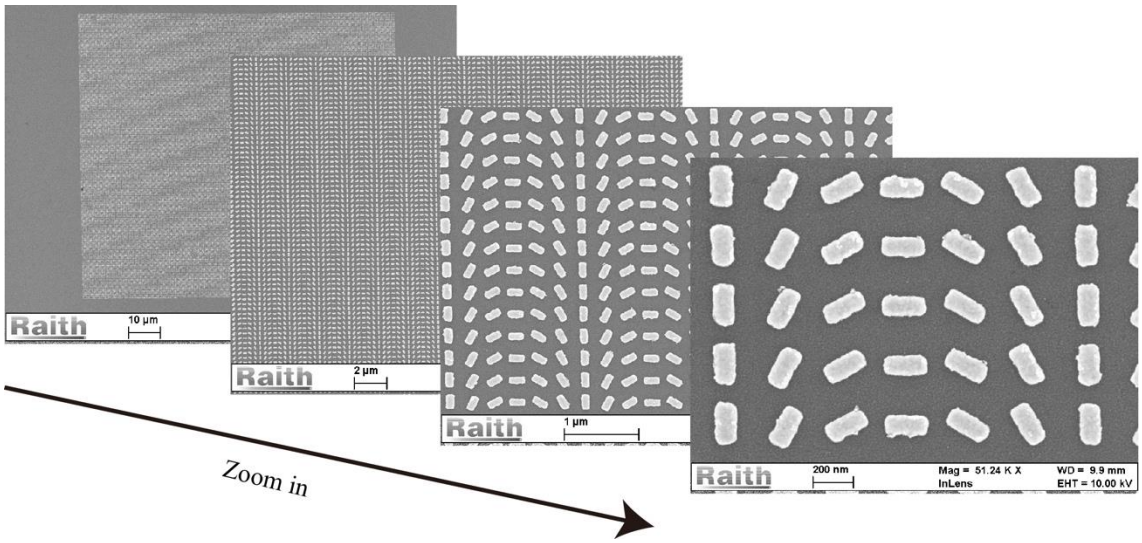

Figure 2.8. Scanning electron microscope (SEM) images of fabricated phase gradient gold metasurface.

Figure 2.9(a) shows the experimentally obtained image of transmission spots with different polarization states of incident light. The middle bright spot is the non-converted light and the spots at the both sides are the converted light. The experimental results verify the generalized Snell's law of refraction described in Equation (2.26). As we can see from Figure 2.9(a), under the normal illumination of a LCP light beam, the converted light which has the opposite circular polarization, is deflected to the left side of the axis of incident light (Top image in Figure 2.9(a)). Similarly, under the normal illumination of a RCP light beam, the converted light is deflected to the right side (Bottom image in Figure 2.9(a)). It is well known that the linear polarization can be viewed as the superposition of a LCP component and a RCP component with equal weight. Therefore, two spots can be observed at both sides under the normal illumination of a linear polarized (LP) light beam as shown in the middle image of Figure 2.9(a). The anomalous transmission angle is determined by the phase gradient and the wavelength. This effect provides an efficient way to measure the polarization state of the incident light [29, 81]. The measured conversion efficiency at different wavelengths is presented at Figure 2.9(b). Although the metasurface approach has a broadband performance, the low efficiency limits its practical applications.

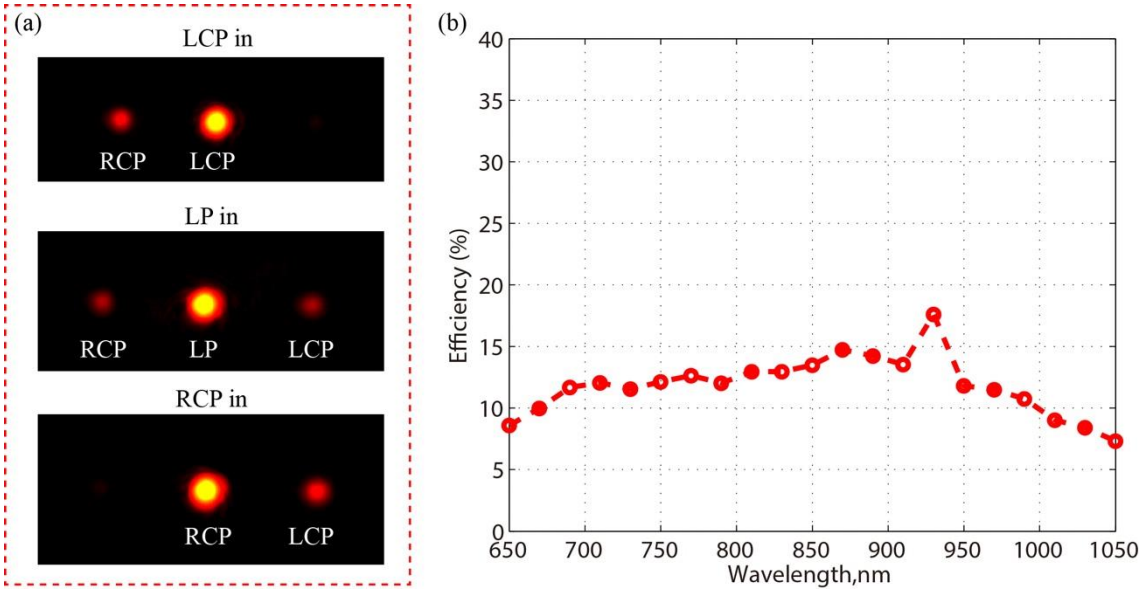

Figure 2.9. The characterization of the phase gradient metasurface. (a) The observed spots under the illumination of light with different polarization states. (b) The measured conversion efficiency over a broad wavelength range.

To increase the conversion efficiency, a reflective-type metasurface with three-layer structure is developed and demonstrated [15, 16, 86, 87]. The reflective-type metasurface is composed of a gold ground layer, a silicon dioxide spacer layer, and a top layer of gold nano-strip arrays. On the one hand, the thickness-dependent dispersion of the dielectric layer compensates the intrinsic dispersion of the gold nano-strips, which provides the capability of ultra-broadband performance [87]. On the other hand, the conversion efficiency can be greatly enhanced by the Fabry-Pérot effect of the multilayer structure [86].

For metallic nanostructures, free electrons at the surface of structures can be excited collectively and coherently under the illumination of electromagnetic field due to the resonant electronic-electromagnetic oscillation. The output light can be modulated by the response of the localized plasmonic resonance. In the case of gold, the plasma frequency is at the visible wavelength range. However, the resonance occurred on gold or other metal is highly dispersive, which limits the broadband performance. If a dielectric layer is sandwiched between the metallic nanostructure layer and a ground metal layer, then the thickness-dependent dispersion of the dielectric layer may compensate the intrinsic dispersion of the gold nanostructures [87]. By appropriately optimizing the thickness of the dielectric layer and the parameters of the nanostructure, the broadband performance of the reflective metasurface can be realised. Moreover, the conversion efficiency of the

metasurface can be significantly enhanced due to the Fabry-Pérot effect of the multilayer structure [86]. We assume an incident light beam $\mathbf{E}_{in}$, the total output light is the sum of all the reflected light from the nanostructure layer and the transmitted light after propagation in the dielectric layer as shown in Figure 2.10. The output light is expressed as

$$\mathbf{E}_{out} = \mathbf{E}_1 + \mathbf{E}_2 + \mathbf{E}_3 + \mathbf{E}_4 + ... \tag{1.26}$$

Now, we need to derive two sets of the coefficients, which are the complex transmission and reflection coefficients at the interface between air and the nanostructure layer r and t, and the complex transmission and reflection coefficients the interface between the nanostructure and the dielectric layer r' and t'. For simplicity of the physical model, the sheet of ultrathin nanostructures is treated as a homogeneous layer [16].

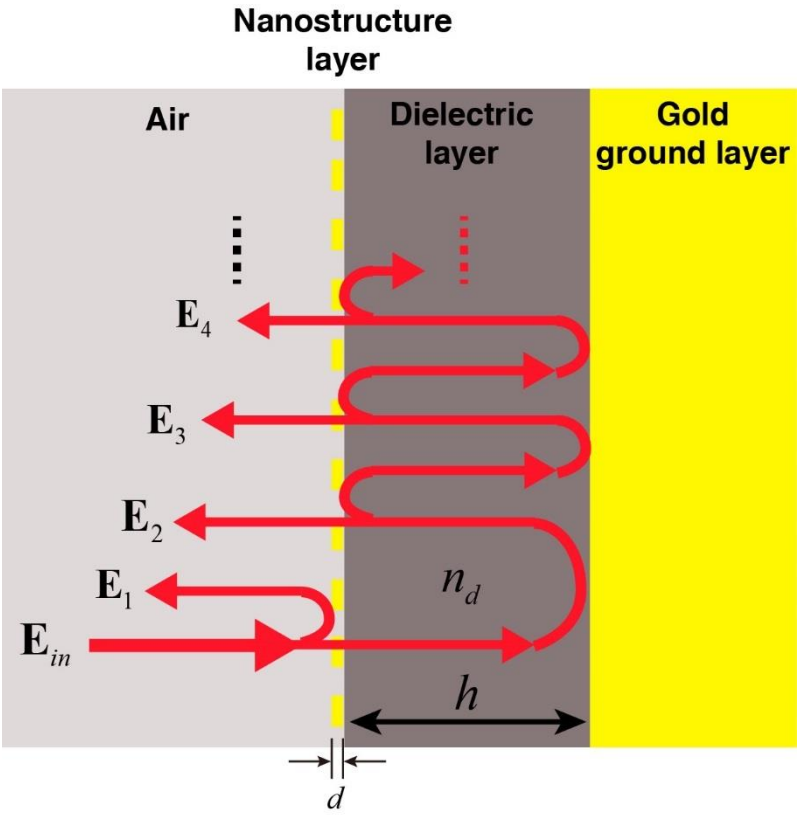

Figure 2.10. Schematic of the multiple reflections from the multi-layer metasurface.

The susceptibility of nanostructure layer is related to the polarizability of the individual nanostructure as [16]

$$\chi_g = \frac{\alpha_g}{a^2 d} \tag{1.27}$$

where α_g is the antenna polarizability, which can be assumed to have a Lorentzian form as $\alpha_g \propto \frac{1}{\omega - \omega_0 + i\gamma}$ due to the localized plasmon resonance of the antennas. Here, the antenna polarizability is obtained with the assumption that the sheet of ultrathin antennas is treated as a homogeneous layer. It differs from the polarizability of the metal nano-strip described in Equations (2.8) and (2.9). More details can be found in reference [16]. *a* is the in-plane lattice constant, d is the thickness of gold nanostructure layer. For sufficiently small d, the complex transmission and reflection coefficients can be derived as [16]

$$r = \frac{\frac{1-n_d}{2} + \frac{i}{2}\frac{k_0\alpha_g}{a^2}}{\frac{1+n_d}{2} - \frac{i}{2}\frac{k_0\alpha_g}{a^2}} \tag{1.28}$$

$$t = \frac{1}{\frac{1+n_d}{2} - \frac{i}{2}\frac{k_0\alpha_g}{a^2}} \tag{1.29}$$

$$r' = \frac{\frac{n_d-1}{2} + \frac{i}{2}\frac{k_0\alpha_g}{a^2}}{\frac{1+n_d}{2} - \frac{i}{2}\frac{k_0\alpha_g}{a^2}} \tag{1.30}$$

$$t' = \frac{n_d}{\frac{1+n_d}{2} - \frac{i}{2}\frac{k_0\alpha_g}{a^2}} \tag{1.31}$$

We assume all the light is reflected on the gold ground layer but get a phase shift φ. The thickness of dielectric layer is h. So the total output light can be given as

$$\begin{aligned} \mathbf{E}_{out} &= \mathbf{E}_{in} r + \mathbf{E}_{in} tt' e^{i(2n_d k_0 h + \varphi)} + \mathbf{E}_{in} tt' r' e^{2i(2n_d k_0 h + \varphi)} + ... \\ &= \mathbf{E}_{in}\left(r + \frac{tt' e^{i2n_g k_0 h + \varphi}}{1 - r' e^{i2n_g k_0 h + \varphi}}\right) \end{aligned} \tag{1.32}$$

By properly choosing the thickness of the dielectric layer h, the dispersion of the complex coefficients can be cancelled by the thickness-dependent dispersion of the dielectric layer. Furthermore, the conversion efficiency can be significantly enhanced due to the Fabry-Pérot effect in the three-layer structure. The simulated and experimentally measured efficiency have been presented in Chapter 2.

Here, the three-layer design is adopted and the simulation and fabrication are performed as well. The schematic of each pixel is shown in Figure 2.11(a) (the inserted image). We sweep the related parameters, including the size of the gold strip, the thickness of the SiO_2 layer and the pixel size, to find the best performance of this design using CST microwave studio software. Figure 2.11(a) shows the simulated conversion efficiency with optimized parameters. The length and width of the nanostrip is 220 nm, 80 nm, respectively. The thickness is 30 nm. The thickness of SiO_2 spacer layer and gold ground layer are 85 nm and 150 nm, respectively. The refractive index of SiO_2 is 1.45. The Drude model where Epsilon infinite is 1, the plasma frequency is 1.37×10^{16} *rad/s*, and the collision efficiency is 1.215×10^{14} *rad/s*, is used for the simulation of material parameters of gold [88]. Periodic boundary is applied in both the *x* and *y* directions. Firstly, the *x* and *y* polarized plane wave are normally incident onto the pixel, respectively. The metasurface works at reflection. Then the spectra of reflection coefficients r_{xx} (*x* polarization in, *x* polarization out), r_{xy} (*x* polarization in, *y* polarization out), r_{yy} (*y* polarization in, *y* polarization out), r_{yx} (*y* polarization in, *x* polarization out) are obtained from the simulation [82]. Finally, the reflection coefficients for circularly polarized light can be deduced from the reflection coefficients of linear polarized light, which are given as $r_{RR} = ((r_{xx} + r_{yy}) + i\times(r_{xy} - r_{yx}))/2$, $r_{RL} = ((r_{xx} - r_{yy}) + i\times(r_{xy} + r_{yx}))/2$. Figure 2.11(a) shows the simulated conversion efficiency ($r_{RL}^{\ 2}$) of the single pixel with optimized parameters. We can see that the conversion efficiency is over 80% at a broad wavelength range.

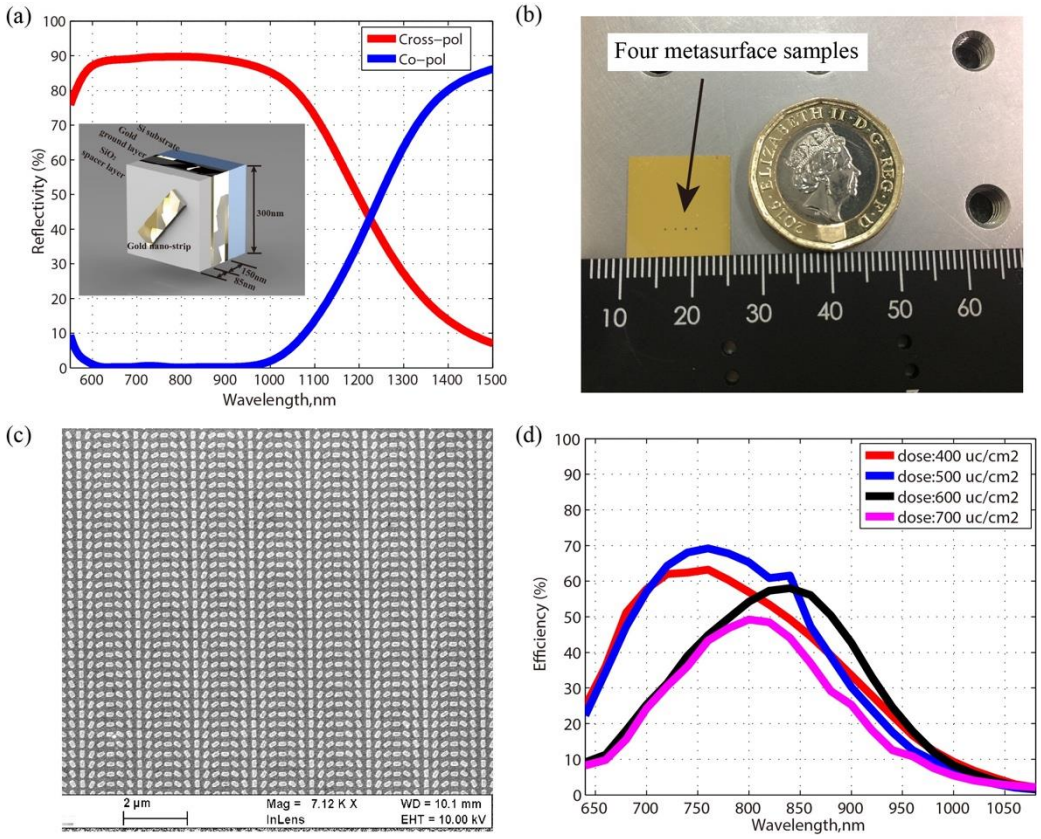

Figure 2.11. The reflective-type metasurface. (a) The simulated conversion efficiency using CST microwave studio. Cross-pol and Co-pol represent the converted and non-converted component, respectively. (b) The image of the fabricated metasurface samples. (c) The SEM image of the reflective-type phase gradient metasurface. (d) The measured conversion efficiency at different fabrication doses.

Based on these optimized parameters, the reflective-type phase gradient metasurfaces are also fabricated and characterized. Prior to the nano-strip array layer define, a gold ground layer with thickness of 150 nm is deposited on the silicon substrate followed by a SiO_2 layer with thickness of 85 nm. Figure 2.11(b) shows the picture of four samples (four black dots) sitting on the silicon substrate. The SEM image of one sample is presented in Figure 2.11(c). Four samples are fabricated with different current doses. Despite the four samples have the same design, the sizes of the resultant structures are different under different current doses. The higher dose, the bigger size. Figure 2.11(d) shows the measured conversion efficiency of all the four samples. We can see that the sample with dose of 500 µc/cm^2 has the highest efficiency. It should be noted that an ultrathin Titanium layer with thickness of 4 nm is deposited between the pattern layer and the SiO_2 spacer layer for adhesion purpose. This layer could slightly decrease the conversion efficiency. The size of each metasurface sample is 400 µm, which is smaller than the size

of incident beam (about 2 mm)In experiment, the incident beam is focused by a lens to make sure all the input beam is shining onto the metasurface sample. This can also cause a reduction of conversion efficiency because of the converge light field. By enlarging the size of metasurface sample, this effect can be eliminated. Moreover, the bigger sample consisting more pixels can further increase the fidelity of diffraction patterns according to the Huygens-Fresnel principle. The reflective metasurface exhibits high conversion efficiency compared with the transmissive plasmonic metasurface. Therefore, the reflective-type metasurface is adopted for the applications described in the following chapters.

2.5 Conclusion

In this chapter, we have discussed the principle of plasmonic metasurface with arrays of nano-strips. The properties of the interaction of a light field with single nano-strip and nano-strip arrays are analysed in the first section. We have shown that the shape and size of nano-strips determine the far-field scattering and absorption. Then we analysed the conversion efficiency of metasurface consisting of nano-strips using the Jones matrix calculus. The geometric phase or Pancharanam-Berry phase, which arises from the interaction of the circularly polarized light and the rotated nano-strip, are discussed in detail. We have theoretically introduced the Generalized Snell's Law corresponding to the phase gradient metasurface. After that the fabrication process of metasurface is presented. We fabricated several metasurface samples to verify the Generalized Snell's Law. Specially, the conversion efficiency of reflective metasurfaces are theoretically analysed and experimentally characterized. In the following chapters, we adopt the reflective metasurface to demonstrate our proposed approaches for phase and polarization manipulation.

Chapter 3 – GEOMETRIC METASURFACE FOR PHASE CONTROL AND ITS APPLICATION IN HOLOGRAMS

In the previous chapter we discussed the interaction between the electromagnetic field and the plasmonic nanostructures. The optical properties of the light can be efficiently tailored by the metasurface consisting of nanostructure arrays. Metasurfaces have been widely used in various research areas, including invisibility cloaking, photonic spin Hall effect, holography, and lensing. In chapter 3, 4, 5, we start to demonstrate the applications of plasmonic metasurfaces based on the phase and polarization control at subwavelength scale. Miniaturization and integration are two continuing trends in the production of photonic devices. Great effort has been made to incorporate multiple functions into a single device [89, 90]. As one of the important multifunction optical elements, polarization selective optical elements can achieve multiple functionalities according to the polarization states of the incident beam; these have been applied in optical encryption, image processing, and so on. In this chapter, we focus on the application of metasurface holograms with polarization-controlled functionality [15, 91]. This chapter is organized as follows. First, the background of the hologram is presented. Then, the simulated and experimental results are demonstrated and analysed.

3.1 Introduction to Holograms

Since its creation in the late 1940s, holograms have been applied in many fields including 3D-projection, design, medicine, and entertainment. Specially, the computer-generated holograms (CGH) attract increasing attentions because there is no need for a real object [92, 93]. By encoding the digitally computed holographic interference pattern to an engineered surface, a holographic image can be generated under the illumination of the coherent light onto the surface. Conventional encoding methods, such as those based on spatial light modulator (SLM), rely on transmitting light through a medium of varying thickness or refractive index. Then the phase front of light is manipulated due to the slight changes in the optical path, which allows for the generation of holograms. However, the phase resolution is limited by the fabrication methods. Moreover, it suffers from the shade effect, twin image, and narrow working bandwidth. Benefiting from the unprecedented manipulation of the phase of light at subwavelength scales, metasurfaces have been employed for the application of holography [21], including colourful holograms [94-96], and broadband holograms [97-99]. The holograms generated by metasurfaces not only have the advantages of high resolution and high conversion efficiency, but also provide the capability to generate and manipulate different holograms by changing the polarization of the incident light through a polarization-sensitive phase control [15, 100].

Here, we adopt the geometric metasurface to generate helicity multiplexed holograms. As shown in Figure 3.1 (bottom right), we design a metasurface which can reconstruct an off-axis “Rubin face” located at left side or right side of the viewing screen upon the illumination of right-handed or left-handed circularly polarized light. Since a linearly polarized light beam can be decomposed into two opposite circularly polarized light beams with equal components. Then, two “Rubin face” can be observed on the screen, and an additional image named “vase” can be perceived between the two faces.

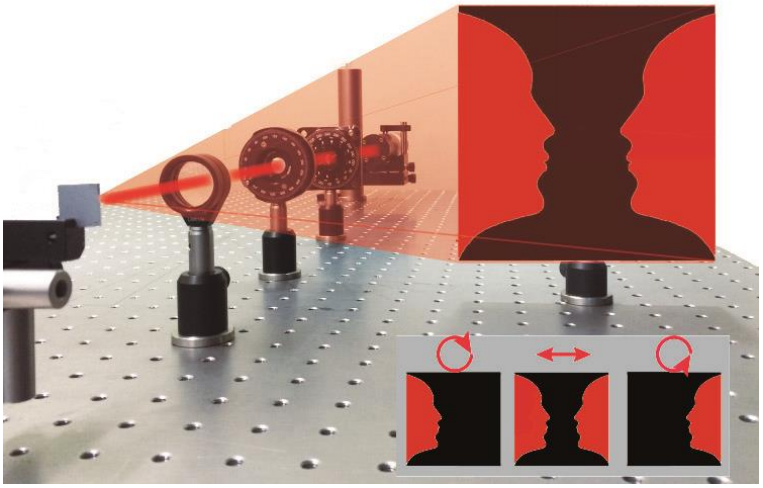

Figure 3.1 Schematic of the polarization-controlled holograms for illusion. A polarizer and a quarter-wave plate are used to generate the required polarization states for the incident light.

The phase profile of the phase-only hologram is obtained using the Gerchberg−Saxton algorithm [101] via the Fourier transform function with multiple iterations. The input data to the algorithm are the amplitudes of the sampled incident beam profile and the intensity distribution of target image at the diffraction plane. The amplitudes are proportional to the square roots of the intensities. In the beginning, an initial array of phase generated by a random number generator (between π and $-\pi$) are multiplied by the respective sampled amplitudes of the incident beam. Then the Fourier transform of this synthesized complex discrete function is done by means of the Fast Fourier Transform. After that, the phases of the resultant discrete complex function are calculated and combined with the corresponding intensity distribution of target image. Then the inverse Fourier Transform of this new synthesized complex function is done. The phase profile is computed and combined with the sampled incident beam profile to form a new complex function for the next iteration. After multiple iterations, the required phase profile is obtained. The polarization-controllable functionality can be explained by the basic principle of the geometric metasurface and the general feature of the Fourier transformation. Suppose the intensity profile of the target image is $I(x, y)$, and the corresponding phase distribution obtained by the Gerchberg−Saxton algorithm is $\phi(x_0, y_0)$. The relation between the intensity profile and the phase distribution is given by

$$I(x, y) = \left| F(A_0 e^{i\phi(x_0, y_0)}) \right|^2 \tag{3.1}$$

where A_0 is the amplitude of the incident light. Here, we assume that the incident light is a uniform planar wave. *F* refers to the Fourier transformation. As discussed in the previous chapter, the sign of the phase generated by the metasurface is dependent on the helicity of the incident light. When the phase distribution changes from $\phi(x_0, y_0)$ to $-\phi(x_0, y_0)$, the resultant intensity profile $I'(x, y)$ can be deduced by

$$\begin{aligned} I'(x,y) &= \left|F(A_0 e^{-i\phi(x_0,y_0)})\right|^2 \\ &= \left|\int\int_{-\infty}^{\infty} A_0 e^{-i\phi(x_0,y_0)} e^{-i2\pi(f_x \cdot x_0 + f_y \cdot y_0)} dx_0 dy_0\right|^2 \\ &= \left|\int\int_{-\infty}^{\infty} A_0 e^{i\phi(x_0,y_0)} e^{-i2\pi(-f_x \cdot x_0 - f_y \cdot y_0)} dx_0 dy_0\right|^2 \\ &= I(-x,-y) \end{aligned} \tag{3.2}$$

where $f_x=x/\lambda z$ and $f_y=y/\lambda z$ (λ is the wavelength and *z* is the reconstruction distance). From Equations (3.1) and (3.2) we can see that the resultant hologram generated under the phase $-\phi(x_0, y_0)$ is the centrosymmetric image of the hologram from $\phi(x_0, y_0)$. Therefore, the feature of polarization-dependent phase generation from the geometric metasurface provides an alternative way to realise the image-switchable functionality of the holograms.

3.2 The Simulated and Experimental Results of The Metasurface Holograms

In this section, we will firstly discuss the design method. Then the simulated and experiment results will be presented. Figure 3.2 shows the design of the target image. The two off-axis "Rubin faces" are designed asymmetrically, which is different from the previous polarization-controlled metasurface holograms with symmetrically distributed target images . Under the illumination of a RCP light, two "Rubin faces" (one upright and one inverted) are reconstructed on two sides of the zero-order spot. When the polarization state of the incident light changes from RCP to LCP, the two "Rubin faces" are rotated 180° counter clockwise and horizontally flipped around point *O*. This is because of the phase-conjugation induced by different helicities of the incident light, which is analysed in the previous section. It is known that the linearly polarized light can be decomposed into RCP and LCP light with the same components. Therefore, the upright and inverted "Rubin's vase" illusions are generated on the both sides for the case of LP incident light.

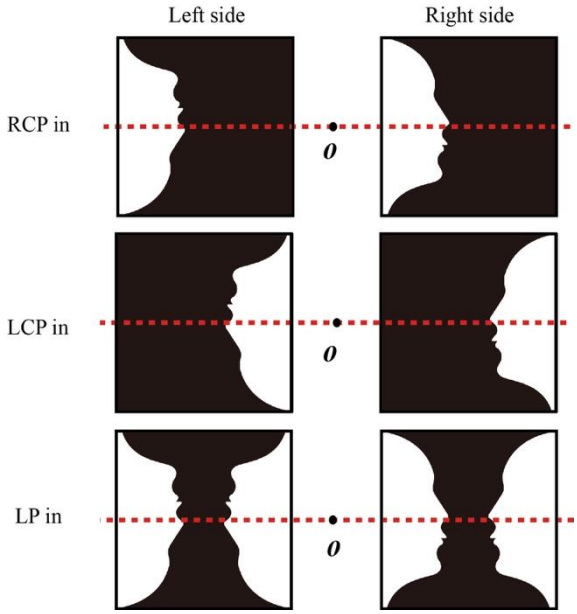

Figure 3.2 Schematic design of the polarization-controlled holograms.

To avoid the unnecessary overlap of the holographic image and the non-converted light, an off-axis design is adopted. The off-axis angle of this target image is $\beta_1 = 9.75°$, and the field of view are $60° \times 23°$ along horizontal and vertical directions, respectively. The Gerchberg-Saxton algorithm is utilized to obtain the expected phase profile of the phase-only hologram. The encoding process from the phase profile into pixelated nanoantennas of the metasurface is straightforward. It should be noted that the coupling effect exists

between neighbouring nanorods. The coupling will be strongest if the corners of the two nearest rods are closest to each other and weakest when they are most apart from each other [16]. Although arbitrary phase levels can be achieved, we choose 32-phase levels (as shown in Figure 3.3(a)) instead of continuous phase distribution to minimize the near field coupling between neighbouring nanorods. Here, a 2×2 periodic array of the phase ("Rubin face") pattern with pixel size of 300 nm × 300 nm and pixel number of 2000×2000 is designed to improve the fidelity of constructed image (Figure 3.3(b)). The whole size of sample is 600 μm.

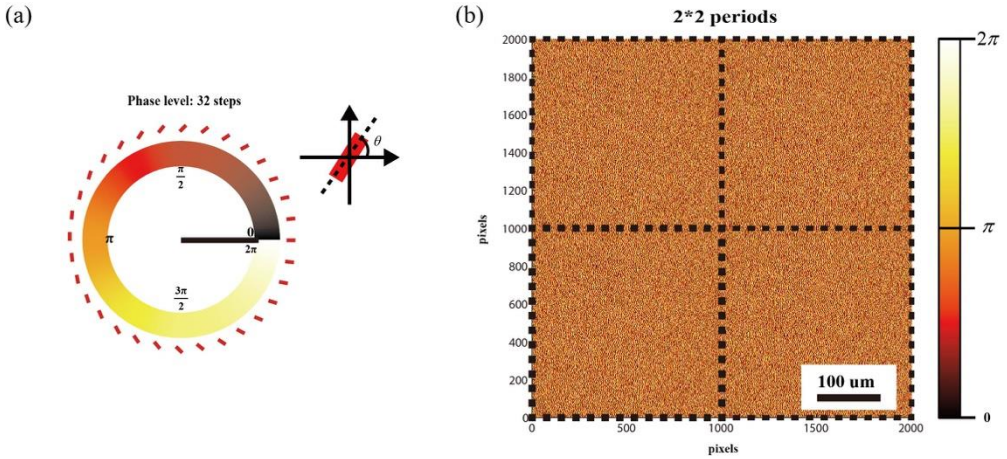

Figure 3.3. (a) The 32 steps of phase level design. (b) The phase distributions generated by the Gerchberg-Saxton algorithm.

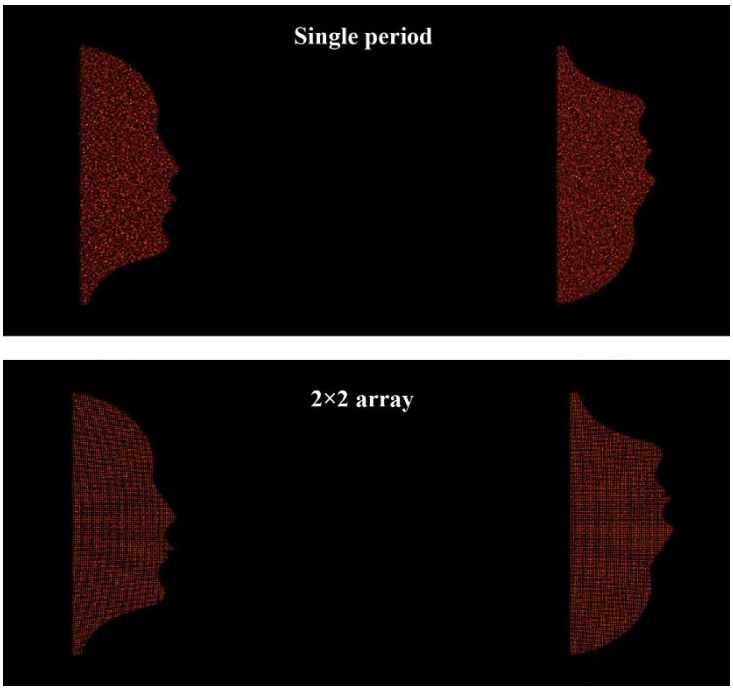

Figure 3.4. The reconstructed image based on phase distribution with single period and 2x2 array, respectively.

The concept of Dammann grating is adopted in design to increase the fidelity of the hologram images. The difference between 2x2 array and a single period is shown in Figure 3.4. In comparison with a single period, which produces a continuous image with lower image fidelity (i.e. more laser speckles), the 2x2 periodic hologram generates an image consisting of discrete spots. The design can be further optimized by a N × N (N is an integer) Dammann grating, which can increase the image quality sharply. However, this will in turn require the need for longer fabrication time.

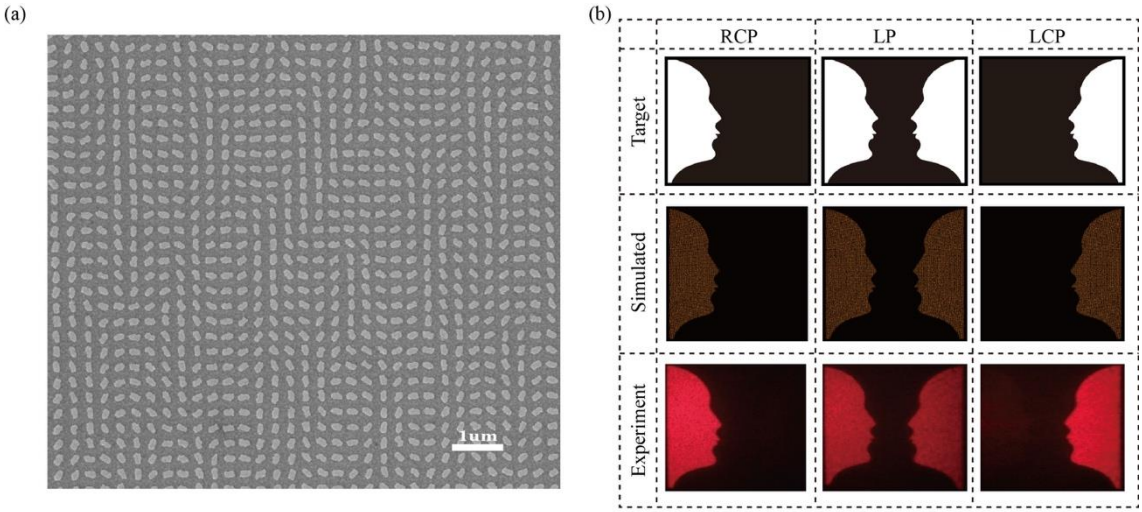

Figure 3.5. (a) The scanning electron microscopy (SEM) image of the fabricated sample. (b) The target, simulated and experimental images.

The reflective metasurface is fabricated using standard electron beam lithography and a subsequent lift-off procedure. The detailed fabrication process can be found in Chapter 2. The scanning electron microscopy (SEM) image of the fabricated metasurface is shown in Figure 3.5(a). The top row on Figure 3.5(b) are the original target images ("Rubin faces") upon different polarization states of the incident light (RCP, LP, LCP). These target images of "Rubin face" can be simulated by considering light emission from all the discretized point sources, as shown in the middle row. The Huygens-Fresnel principle states that every point on the object plane is a source of spherical waves with the same frequency. The resulting field on the diffraction plane is a superposition of these secondary waves defined by their complex amplitude and/or wavefunction. Thus, the complex amplitude at any point of hologram image can be numerically obtained as a sum

of complex amplitudes of all the secondary wavelets. Then the hologram image is reconstructed. To experimentally verify the method and inspect the performance of the fabricated metasurface samples, a polarizer and a quarter-wave plate are located after the tuneable laser source to generate the required polarized states. Then, a plano-convex lens (f=150 mm) is used to weakly focus the light beam with a beam size of 2 mm onto the fabricated sample. The setup is shown in Figure 3.1. The off-axial holographic images are reconstructed under the illumination of the light with certain polarizations. Here, a viewing screen is used to display the holographic images. The bottom row on Figure 3.5(b) present the experimentally captured holographic images for RCP, LP and LCP of the incident light at the wavelength of 633 nm. The distance between the screen and the metasurface is 60 mm. Upon the illumination of RCP light, a holographic image named "Rubin face" with high signal-to-noise is reconstructed on the left side of the screen. Due to the design method, the size of the "Rubin face" is proportional to the reconstructed distance between the sample and the screen. When the polarization of incident beam is changed from RCP to LCP, a horizontally flipped image of "Rubin face" is displayed on the right side, which clearly shows that the position of the holographic image is dependent on the polarization state of the incident light. Under the illumination of LP light that is the superposition of LCP and RCP light with equal components, two pairs of different centrosymmetric "Rubin faces" (one upright and one inverted) are generated. Even more intriguingly, an additional image of "vase" is also perceived between these two "Rubin faces".

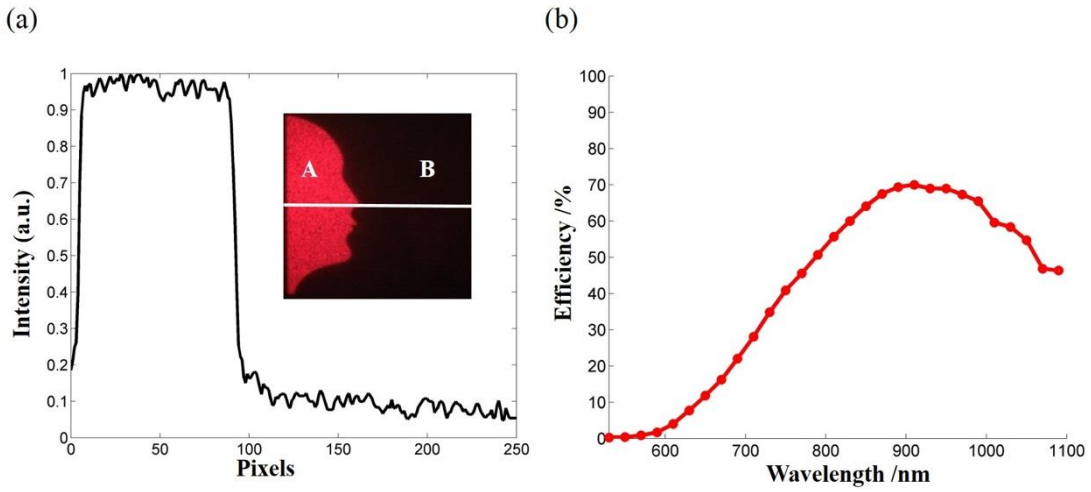

Figure 3.6. (a) The Signal-to-noise ratio of the experimentally obtained hologram at wavelength of 633 nm. (b) The measured conversion efficiency of the metasurface sample.

To further characterize the performance of the metasurface approach, we inspect the experimentally obtained hologram and calculate the signal-to-noise ratio (SNR). The SNR is defined as the ratio between the mean power of area A and the standard deviation of area B as shown in Figure 3.6(a). The measured SNR of the optical hologram is 7.6. The noise is mainly caused by the irregularity of nanorods, and non-rigid of the plane-wave incidence. The SNR can be further improved by optimising the fabrication process and optical experimental setup. We also measured the conversion efficiency of the metasurface over a broadband wavelength in the range from 530 nm to 1090 nm. The conversion efficiency is defined as the ratio of the power of all the reconstructed images and the input power. In experiment, a condenser lens with focal length of f=32 mm is used to collect the generated images. The conversion efficiency in experiment is 69.94% at the wavelength of 910 nm. It is worth to note that conversion efficiency is limited by the fabrication error of nanorods, and the absorption of the titanium layer between nanorods and SiO_2 layer. No twin images are observed in our experiment since the pixel size (300 nm) is much smaller than the wavelength of the incident light.

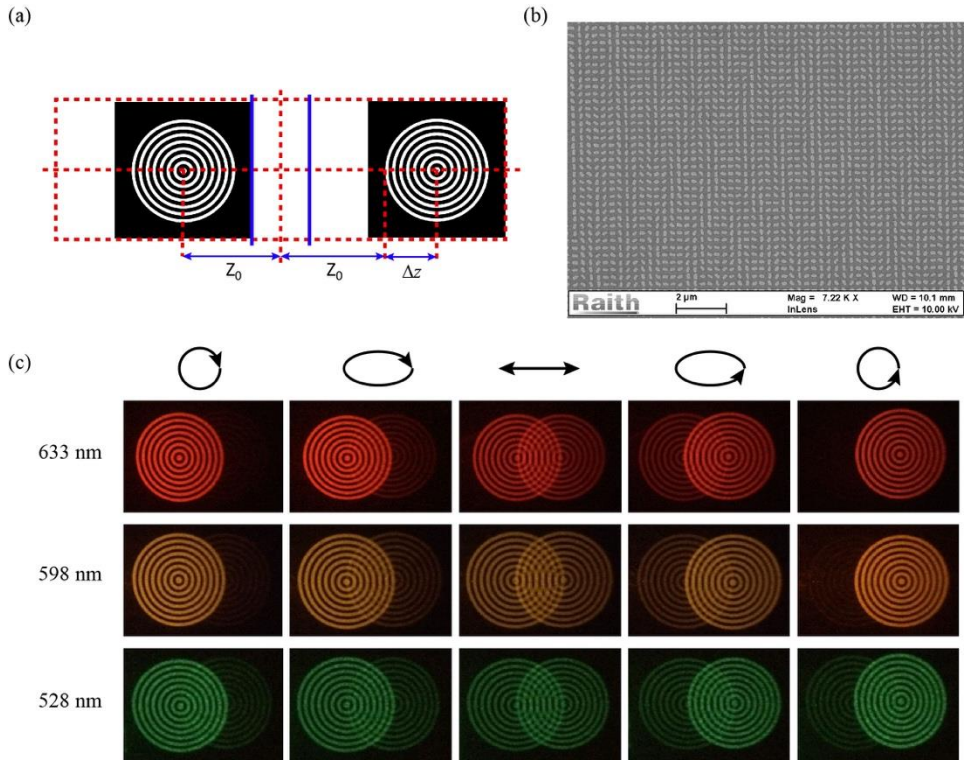

Figure 3.7. (a) The design of the target image. (b) The scanning electron microscopy (SEM) image of the fabricated metasurface. (c) The experimentally captured images at different polarization states and wavelengths.

To demonstrate the versatility of the metasurface for the realization of optical holograms based on the phase control, we also developed other metasurface devices to generate Moiré fringes. Figure 3.7 shows the design of the target image and the experiment results. In this case, the original target images are two identical concentric annuluses located on the two sides (see Figure 3.7(a)). But the location of the two images are asymmetric. Therefore, for the LP light illumination, both the concentric annuluses are partially overlapped with each other on the display screen. Moiré fringe is generated by the superposition of the light intensities of these overlapped concentric annuluses. Figure 3.7(b) is the SEM image of the fabricated metasurface. The samples are characterized at different polarization states including right-handed circular polarization (RCP), right-handed elliptical polarization (REP), horizontal linear polarization (HLP), left-handed elliptical polarization (LEP), and left-handed circular polarization (LCP). The intensity evolution of the holograms can be observed from the experiment results. Figure 3.7(c) presents the experimental results at different wavelengths and different polarization states.

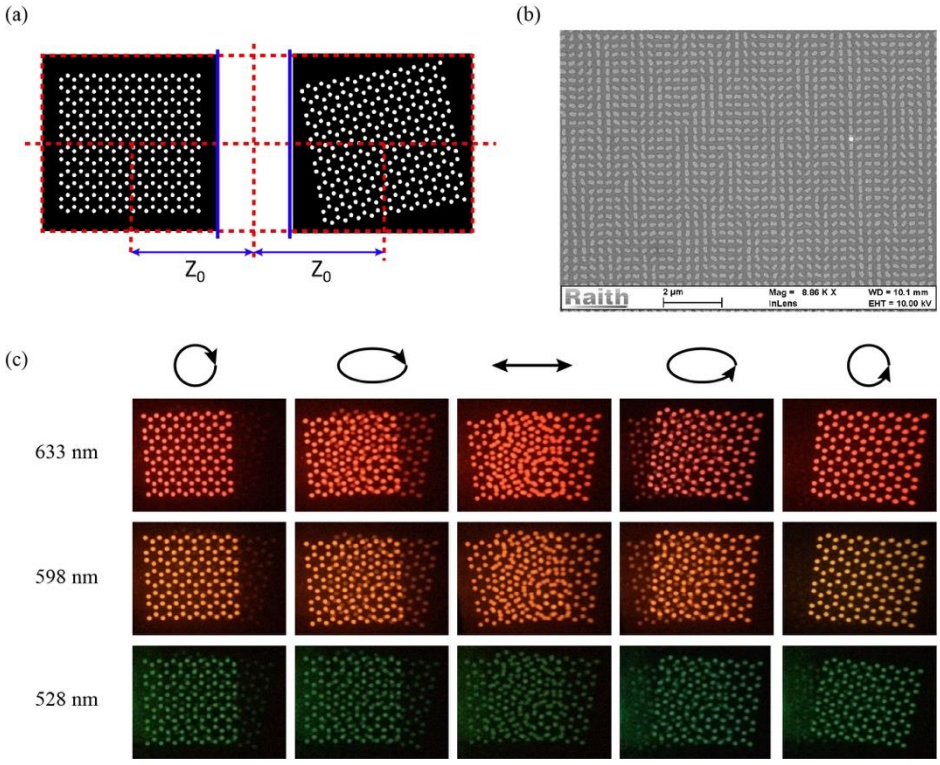

Figure 3.8. (a) The design of the target image. (b) The scanning electron microscopy (SEM) image of the fabricated metasurface. (c) The experimentally captured images at different polarization states and wavelengths.

Figure 3.8 shows another example of the metasurface hologram. Different from the design of the previous two holograms that are asymmetry, the two images are symmetry in terms

of the zero point. Moreover, the image pattern on the right side is rotated 20^{o} to generate different overlap fringe. The design method is shown in Figure 3.8(a). The fabricated SEM image and the experimental results are presented on Figure 3.8(b) and (c).

The geometric metasurface provides arbitrary phase control at the nanoscale. Moreover, with the optimized design, it can work at a broad wavelength range with high efficiency. This approach proposed in this chapter is compatible with standard semiconductor fabrication process. More importantly, the polarization multiplexed functionalities are realised by combining two sets of holograms operated with opposite incident helicities, which provides a new methodology to integrate multiple optical functionalities into one single optical element.

Chapter 4 – GEOMETRIC METASURFACE FOR VORTEX BEAM GENERATION AND MANIPULATION

It is known that light can carry both the spin angular momentum (SAM) and orbital angular momentum (OAM). The SAM and OAM are manifested as circular polarization and azimuthal phase structure of light beam, respectively. Since the first report in 1992 by Allen *et al.* that light beams with an azimuthal phase dependence of $\exp(i\ell\varphi)$ carry the OAM [102], it draws extensive attention since the OAM can be many times greater than the SAM and such beam carrying OAM is easily realizable. The OAM of light has been found in various applications including optical tweezers [103], quantum memories [104], optical communication [105-107], and metrology [108, 109].

In the previous chapter, we described the polarization-controlled holograms realised by the geometric metasurface. We now turn our attention to the generation and manipulation of orbital angular momentum of light using geometric metasurface. Firstly, the background of orbital angular momentum of light is presented, and the vortex beams with different topological charges of orbital angular momentums are experimentally demonstrated using reflective metasurfaces. Then a novel approach to realise the superposition of orbital angular momentum states in multiple channels using a single metasurface device is proposed and experimentally demonstrated [31]. With this principle, not only the phase but also the polarization states can be controlled at the nanoscale. Vector beams and Poincaré beams with inhomogeneous phase and polarization distribution on the transverse plane of the beams could be easily realised and manipulated. This approach solves several major issues associated with OAM research: multichannel OAM generation, polarization-controllable OAM superposition, higher resolution, broadband, and compactness, rendering this technology very attractive for diverse applications such as photonics, quantum science, and fundamental physics.

4.1 The Orbital Angular Momentum of Light

4.1.1 The introduction of orbital angular momentum of light

Polarization, defined as the vibration direction of the electric field vector, plays crucial role in light characterization. The fundamental state of polarization of light beam such as linear polarization, elliptical polarization and circular polarization could be described as a superposition of two orthogonal circular eigenstates (left- and right-handed) and represented on the surface of fundamental Poincaré sphere. These two circular eigenstates correspond to the spin angular momentum (SAM) of light. Circularly polarized light carries the spin angular momentum of $\pm\hbar$ per photon. The sign of the SAM is determined by the helicity of the circular polarization. The SAM of light was firstly anticipated by Poynting [110] in 1909. He theoretically predicted that circularly polarized light should possess an angular momentum to energy ratio of $\sigma\hbar$. 27 years later, Beth *et al.* successfully demonstrated the transformation between the circularly polarized light and the rotational motion of a birefringent wave plate suspended on a filament [111].

Indeed, light beam can carry not only spin angular momentum (SAM), but also orbital angular momentum (OAM) which is manifested as azimuthal phase structure of light beam. Light carrying OAM (namely optical vortex), also known as Laguerre-Gaussian mode, has a helical phase structure described by $\exp(i\ell\varphi)$, where φ is the azimuthal angle, ℓ is the topological charge of optical vortex corresponding to an orbital angular momentum of $\ell\hbar$ per photon [102]. A striking difference between the SAM and the OAM is the range of allowed values. SAM can only have two values, $\pm\hbar$ per photon, expressed as left or right circular polarization. While OAM has an unbounded value of $\ell\hbar$ per photon, $\ell = 0,\ \pm 1,\ \pm 2,\ \pm 3.....$. In 1992, Allen *et al.* theoretically demonstrated that all the helically phased beams carry the OAM [102], which opens a new window for the study of OAM and its applications.

The OAM states of light can be mathematically represented as Laguerre-Gaussian (LG) modes which are solutions of the paraxial Helmholtz equation in cylindrical coordinates. The LG mode is characterized by two indices ℓ and p . ℓ refers to the azimuthal phase dependence, and p refers to the radial nodes in its amplitude. Here, we limit to the case of singly-ringed modes with $p = 0$. The field distribution of LG modes with topological charge ℓ can be given as [102]

$$LG^{\ell}(r,\phi,z)=\left(\frac{2}{\pi\,|\,\ell\,|\,!}\right)^{1/2}\frac{1}{w(z)}\left(\frac{r\sqrt{2}}{w(z)}\right)^{|\ell|}e^{-r^2/(w(z))^2}e^{-i\ell\phi}e^{i(kz-kr^2/(2R(z)))}e^{i\varphi(\ell)} \qquad (4.1)$$

where $w(z)=w_0\sqrt{2+z^2/z_R^2}$ is the beam radius at a propagation distance z . r,ϕ,z are the cylindrical coordinates, k is the wave number, the constant w_0 is the beam waist, $R(z)=(z_R^2+z^2)/z$ denotes the radius of curvature of the wavefront, $\varphi(\ell)=(|\,\ell\,|+1)\tan^{-1}(z/z_R)$ is the ℓ -dependent Gouy phase [112], and $z_R=kw_0^2/2$ is the Raleigh range. The LG mode has a 'doughnut' intensity profile due to the phase singularity at the beam axis. The distance from the centre to points where the intensity is maximum is given by $\Omega=\sqrt{\frac{\ell}{2}}w(z)$, which denotes the radius of the 'doughnut' ring. Figure 4.1 shows sample examples of OAM beams with different topological charges. The wavefront, the phase distribution, and the intensity profile are presented in this Figure.

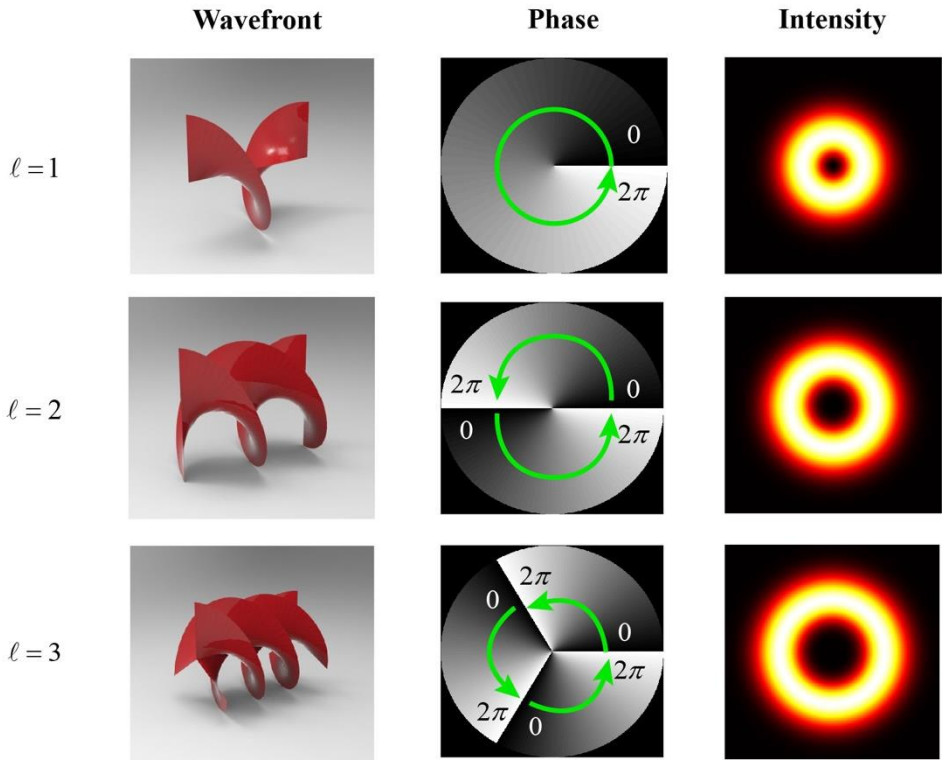

Figure 4.1 The wave front, the phase distribution, and the intensity profile of OAM beams with topological charges of $\ell=1,\ell=2$, and $\ell=3$.

4.1.2 The generation of OAM beams

The common approach to generate the helically phased beam is to pass a plane wave beam through an optical element that can manipulate the wave front of the incident beam, such as spiral phase plate, spatial light modulator cylindrical lenses, and the q-plate.

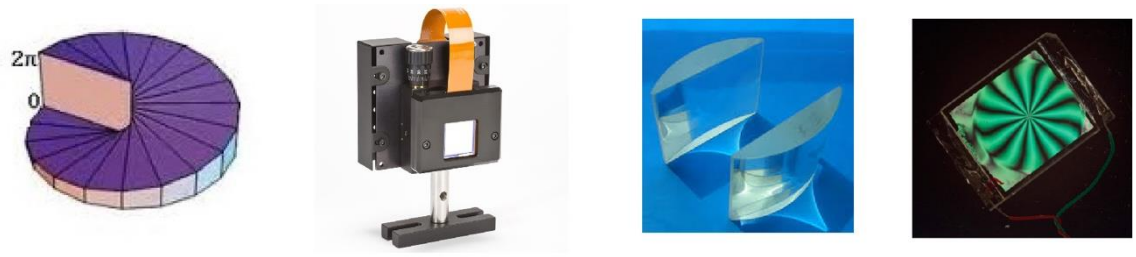

(a) spiral phase plate (b) spatial light modulator (c) cylindrical lenses (d) q-plate

Figure 4.2. The common optical approaches to generate the OAM beams. (a) Spiral phase plate. (b) Spatial light modulator. (c) Cylindrical lenses. (d) The q-plate.

The spiral phase plates are a type of optical component with azimuthal position dependent optical thickness according to $\ell\lambda\theta/2\pi(n-1)$, where n is the refractive index of the medium (see Figure 4.2(a)). The advantage of the type of elements is that it is not dependent on the polarization state of the incident light. An alternative approach to generate the OAM of light is the diffractive optical elements such as the spatial light modulator (SLM) as shown in Figure 4.2(b). The SLMs are based on translucent or reflective liquid crystal micro-displays, which can be programmed by a computer to spatially modulate the amplitude or phase of the light. Usually the SLM has certain working directions for the linearly polarized beams. It has maximum efficiency for the incident light with certain linear polarization. The cylindrical lens mode converters can also be used to transform the LG modes from the Hermite-Gaussian (HG) modes (see Figure 4.2(c)). These mode converters consist of two components: the $\pi/2$-converter and the π-converter. The advantage of this approach over SLMs is high conversion efficiency which is only limited by the quality of the cylindrical lenses.

More recently, another optical device named q-plate provides the researchers with an alternative tool to generate the OAM of light [113]. The q-plate (as shown in Figure 4.2(d)) is a liquid crystal cell with a thin liquid crystal film sandwiched between two glasses, which can be electrically controlled. The q-plate allows the generation of light with OAM from ordinary light with circular polarization, which has found various applications in classical and quantum photonics [114, 115].

Despite many approaches and methods [116-118] have been proposed to generate the OAM beams, these systems could not be straightforwardly downsized, preventing from widespread applications in integrated optics. Moreover, the limitations of poor resolution of the SLM, low damage threshold of the q-plate still need to be overcame for practical applications.

Nano-fabrication advances have enabled the development of metasurfaces capable of controlling the wave front of the incident light in the subwavelength domain. To experimentally demonstrate the OAM beams generation using metasurface, several samples with single gold pattern layer are fabricated and characterized. The required phase profiles (see examples in Figure 4.1) are realized by changing the orientation angles of the nanorods according to the Pancharatnam-Berry phase mechanism. Figure 4.3 shows the experimental results of OAM beams with different topological charges by geometric metasurfaces. The SEM images of the fabricated samples are shown in the top column of Figure 4.3. In experiment, a linear polarizer and a quarter-wave plate are inserted in front of the sample to generate the required circular polarization. Then the light is weakly focused by a lens to ensure that the beam size on the sample plane is smaller than the sample. It is worth to mention that the alignment between the incident beam and the metasurface is very important. The best performance happens when the centre of the beam and the metasurface sample coincide.

The metasurface sample is mounted on a 2D translational state to adjust the position. Another pair of a linear polarizer and a quarter-wave plate is used to pass the converted light with opposite circular polarization and isolate the nonconverted light with the same circular polarization. A charge coupled device (CCD) camera is used to record the intensity profile of the output beam.

The intensity profiles of the OAM beams are shown in the middle column of Figure 4.3. The doughnut shapes of the resultant beams confirm the existence of optical vortices. The vortex beams contain intensity null at the beam axis because of the phase singularity. The radius of the ‘doughnut’ ring depends on the absolute value of the topological charge of the OAM. To further confirm the topological charge of the resultant OAM beams, the angle of the linear polarizer after the metasurface is slightly tuned to let both the converted and residual beam partially pass. Then the nonconverted beam serves as the reference spherical wave to interfere with the converted vortex beam. The helical intensity profiles

and the number of branches stemming from the singularity confirm the topological charge of the resultant beam generated by the metasurface (see Figure 4.3 bottom column) [119].

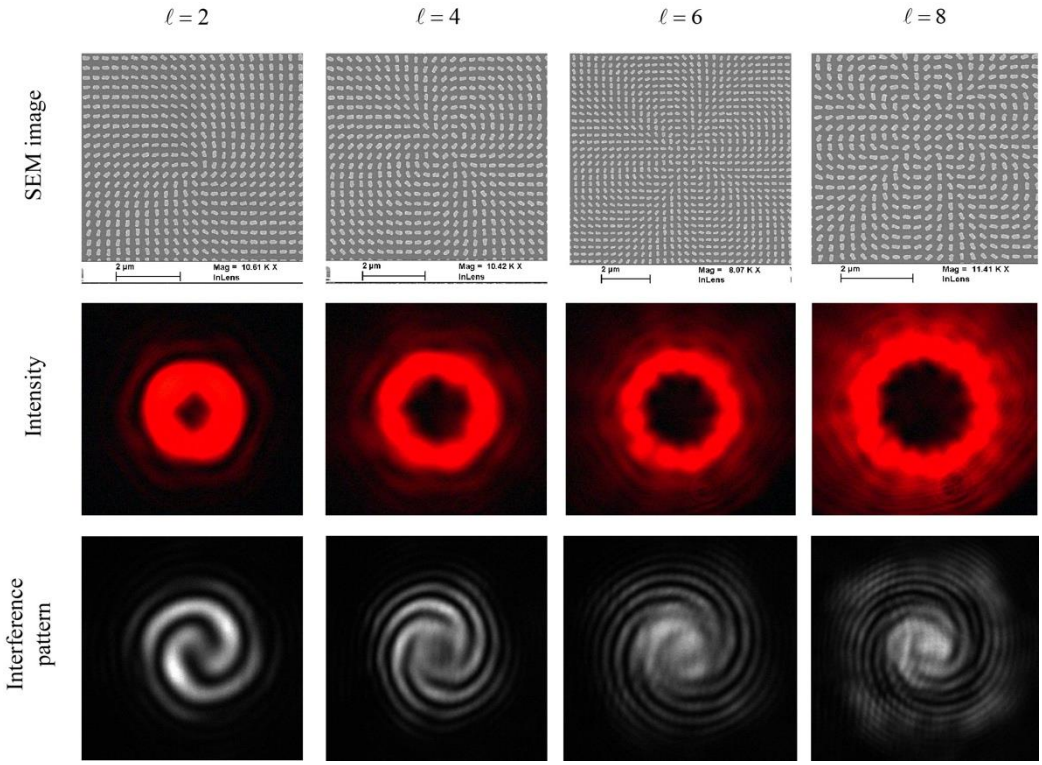

Figure 4.3. The experimental results of OAM beams generation using geometric metasurfaces.

4.2 The Superposition of OAM States Using Single Metasurface

Arbitrary state of polarization of light beam such as linear polarization, elliptical polarization could be described as a superposition of two orthogonal circular eigenstates (left- and right-handed). The amplitude coefficients and the phase difference of the two components determine the ellipticity and azimuthal angle of the resultant polarization. As discussed in above section, the light beam carrying orbital angular momentum or vortex beam has azimuthal dependent phase distribution and 'doughnut' shape intensity profile on the transverse plane of the beam. If we superimpose two vortex beams with different topological charges and orthogonal circular polarizations, the resultant beam with complex phase and polarization distribution can be generated, such as cylindrical vector beam [120, 121], vector vortex beam [116, 119], and Poincaré beams [122, 123]. In this section, the metasurface approach for the realization of superposition of OAM states are discussed, and the intensity profile and polarization distribution of the resultant beams are analysed theoretically and experimentally.

4.2.1 The background

Light can carry SAM and OAM, which corresponded with circular polarization and azimuthal phase structure of light beam, respectively. Light possessing OAM has a helical phase structure described by $\exp(i\ell\theta)$, where ℓ is the topological charge of optical vortex, corresponding to an orbital angular momentum of $\ell\hbar$ per photon. The superposition of OAM states with orthogonal circular polarizations is of importance both in classical physics and quantum sciences. For instance, linear combination of OAM modes with equal components and opposite circular polarizations and opposite signs of topological charges $\ell = 1$ and $\ell = -1$ gives rise to the cylindrically vector beam that has radially or azimuthally distributed polarization. The cylindrically vector beam has distinguished features. The radially polarized beam leads to a strong longitudinal electric field component around the focus under strong focusing by an objective with a high numerical aperture. In contrast, the azimuthally polarized beam generates a strong magnetic field at the optical axis of the beam [124]. The cylindrically vector beam has been applied in high-speed kinematic sensing [125] and improved focusing [124]. Moreover, superposition of OAM modes with high-order topological charges can be used for ultra-sensitive angular measurement [109] , rotational Doppler effect [126], and spin object detection [108]. The electromagnetic field with Multi-OAM-state can also be used to

generate arbitrary superposition of atomic rotational states in a Bose-Einstein condensate (BEC) [127, 128]. In addition, light beams with entangled OAM states and orthogonal circular polarizations are prime candidates for fundamental characterizations of quantum entanglements [129], especially the spin-orbit hybrid entanglement [130-132].

Despite the diverse applications of OAM beams, there are fundamental or technical challenges for current techniques to efficiently generate and manipulate the superposition of OAM states. As discussed in the previous section, the optical OAM beams can be generated using cylindrical lenses, computer generated holograms, and spiral phase plates. However, all these devices are polarization independent. Thus, it cannot be adopted in the promising quantum photonic applications related to the spin-to-OAM conversion. The q-plates have been developed and employed in many research fields such as transformation of qubits between photons, and polarization-controlled OAM beam generation [114, 133, 134]. Nevertheless, q-plates are susceptible to chemical degradation and sensitive to temperature. The q-plates also have the disadvantage of poor spatial resolution and complicated operation.

The interferometer [104, 135] consisting of OAM generator, beam-splitters and mirrors can be employed to realise various superpositions of OAM states in quantum experiments. However, such an approach significantly increases the complexity and volume of experimental systems. In addition, the system performance may greatly be affected by the aberrations and the misalignment of the optical elements. Consequently, an efficient and compact approach to realise artificially controlled generation and coherent superposition of OAM states, even in multichannels, is desirable, because of the broad range of applications. Due to the exotic electromagnetic properties and potential breakthroughs for light manipulation, metasurface provides the ability to generate the superposition of OAM states in multichannels. By changing the polarization state of the incident light, the superposition can be simply controlled. The advantages of multiple OAM generation, polarization-controlled superposition, and subwavelength resolution, renders this metasurface approach attractive for various applications both in classical physics and quantum optics.

4.2.2 Design and method

The basic principle of this approach is based on the fact that arbitrary polarization state is the superposition of orthogonal circular polarizations. The key point of this method for

the realization of superposition of two OAM states is to generate the phase structure that two OAM bases are generated simultaneously by shining a RCP light. Moreover, the two generated OAM beams are propagated along symmetry-equivalent directions with respect to the axis of incident light. This can be realised by the phase-merge method described by the following equation [105, 136]

$$\Phi(x, y) = \arg(\sum_{i=1}^{N} E_i(\exp(i\ell_i\theta) + \Delta\varphi_x + \Delta\varphi_y)) \tag{4.2}$$

where N is the total number of OAM states, E_i is the power of OAM state ℓ_i with respective to the total power, θ is the azimuthal angle. $\Delta\varphi_x$ and $\Delta\varphi_x$ are phase gradients in x and y directions, which introduce the off-axis deflection for the OAM modes of interest, respectively [2].

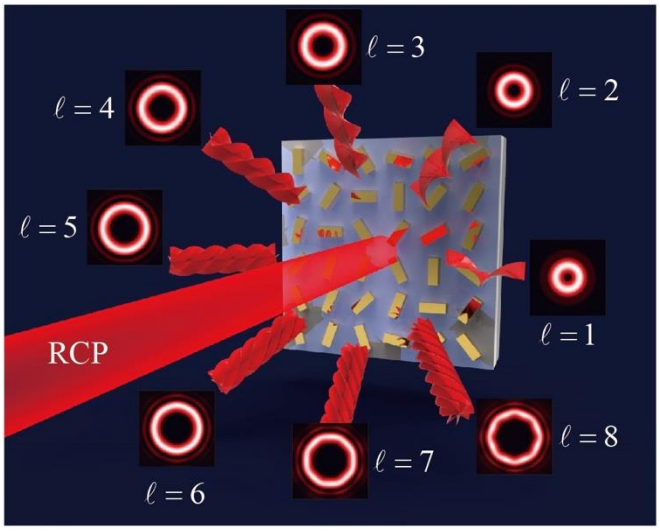

Figure 4.4. Schematic of eight OAM states from $\ell = 1$ to $\ell = 8$ generation under illumination of RCP light using equation (4.2). Considering the practical application, the off-axis design is employed in this approach. By changing the handedness of incident light from RCP to LCP, all the OAM beams are flipped to the symmetric position with respect to the axis of incident light. Meanwhile, the sign of topological charges become negative from positive.

Equation (4.2) can be used to generate spatial multiplexed OAM states. Figure 4.4 shows the schematic for generation of eight OAM beams with topological charges form $\ell = 1$ to $\ell = 8$ under a RCP Gaussian beam illuminating upon the designed metasurface. It is noted that, by changing the handedness of incident light from RCP to LCP, all the OAM beams

are flipped to the symmetric position with respect to the axis of incident light. Meanwhile, the sign of topological charges become negative from positive.

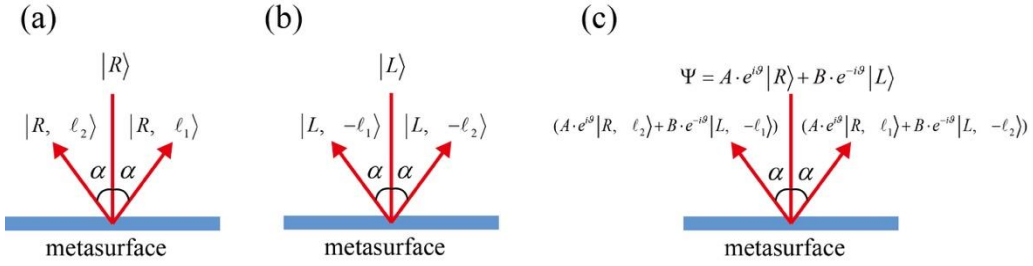

Figure 4.5. Method of polarization-controlled superposition of OAM states. The polarization state of incident light is (a) RCP and (b) LCP, respectively. (c) The case of incident light with arbitrary polarization state which is superposition of RCP and LCP light with different components (*A* for RCP and *B* for LCP) and phase difference $e^{i2\vartheta}$.

Figure 4.5 presents the principle of this approach. When a RCP Gaussian beam ($|R\rangle$) is illuminated upon the metasurface with designed phase structures, two OAM beams $|R,\ \ell_1\rangle$ and $|R,\ \ell_2\rangle$ are generated, with the symmetry-equivalent propagating directions (see Figure 4.5(a)). The explanation about the polarization conservation can be found in other references [16]. By switching the handedness of incident light, the propagating directions of two resultant OAM beams are swapped with respect to the incident axis. In addition, the signs of topological charges are changed from positive to negative since the abrupt phase change introduced by nanorods is handedness-dependent [2] (see Figure 4.5(b)). Arbitrary polarized light can always be decomposed into a superposition of the two circular polarized waves with opposite handedness which are eigenstates of Poincaré sphere (see Figure 4.5(c)). It is described as

$$|\Psi\rangle = \cos\theta\cdot e^{i\vartheta}\cdot|R\rangle + \sin\theta\cdot e^{-i\vartheta}\cdot|L\rangle \tag{4.3}$$

where $\cos\theta$ and $\sin\theta$ are the amplitudes of RCP and LCP light, and ϑ is the phase difference of two components. When a light beam with polarization state of $|\Psi\rangle$ is shining on the metasurface, two kinds of superpositions with different OAM states and orthogonal circular polarizations are generated in two channels, which are $(\cos\theta e^{i\vartheta}|R,\ \ell_2\rangle + \sin\theta e^{-i\vartheta}|L,\ -\ell_1\rangle)$ and $(\cos\theta e^{i\vartheta}|R,\ \ell_1\rangle + \sin\theta e^{-i\vartheta}|L,\ -\ell_2\rangle)$. This is shown in Figure 4.5(c). Now we can see that the superposition of two OAM beams is

realised under the incident beam with polarization state of $|\Psi\rangle$, such as linear polarization or elliptical circular polarization. Moreover, by changing the polarization state of the incident light, the superposition can be manipulated.

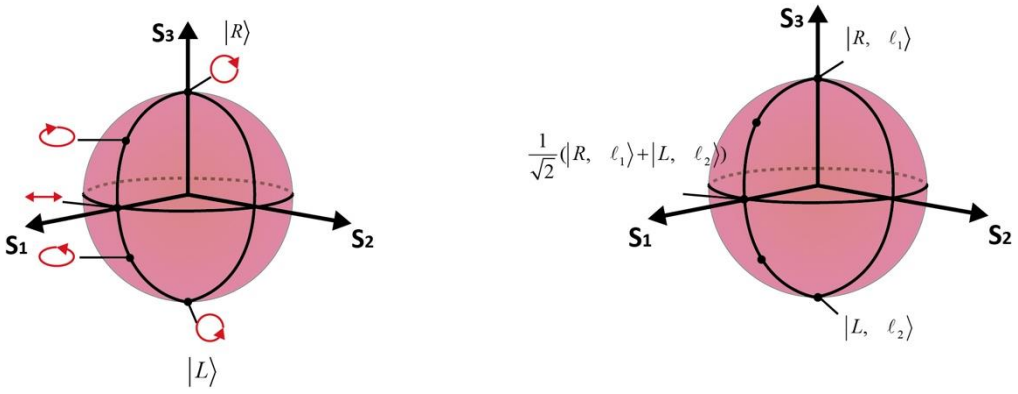

(a) Poincaré sphere (b) Higher-order Poincaré sphere

Figure 4.6. (a) Illustration of the Poincaré sphere representation of polarization state of incident light (b) and the higher-order Poincaré sphere representation of superposition of OAM eigenstates ℓ_1 and ℓ_2.

To describe the evolution of OAM superposition, we introduce the recent concept of the Higher-order Poincaré sphere [137, 138]. In analogy to the well-known Poincaré sphere for polarization (or SAM) state description, any state in a given O_ℓ subspace can be represented as a point on the Higher-order Poincaré sphere. The poles of the sphere are the OAM eigenvalues $\pm\ell_{1,2}$ and correspond to Laguerre-Gauss (LG) transverse modes. It should be mentioned that the value of OAM eigenstates ℓ_1 and ℓ_2 can be different [139].

The superposition of LG modes with orthogonal circular polarization states produces structured beams with inhomogeneous phase and polarization distribution [140]. As described in above section, arbitrary pure polarization state can be represented with circular polarization bases. When a Gaussian beam with polarization state described by equation (4.3) illuminates the metasurface, the resultant beam is the superposition of two LG modes with orthogonal circular polarization. Consider the superposition of two LG modes with topological charges ℓ_1 and ℓ_2, the resultant beam can be expressed as

$$V = \frac{1}{\sqrt{2}}(\cos\theta \cdot LG^{\ell_1} \cdot e^{i\alpha} |R, \quad \ell_1\rangle + \sin\theta \cdot LG^{\ell_2} \cdot e^{-i\alpha} |L, \quad \ell_2\rangle) \tag{4.4}$$

To clearly analyse the properties of the resultant beam, the discussions are divided into two cases: when $\ell_1 = -\ell_2$ and $\ell_1 \neq -\ell_2$.

For the case of $\ell_1 = -\ell_2$, we can rewrite equation (4.4) with Jones vector as

$$V = \frac{G^{\ell}}{\sqrt{2}}(\cos\theta e^{i(\ell\phi+\alpha)}\left|R\right\rangle + \sin\theta e^{-i(\ell\phi+\alpha)}\left|L\right\rangle) \tag{4.5}$$

where

$$\ell = \ell_1 = -\ell_2 \tag{4.6}$$

$$G^{\ell} = \left(\frac{2}{\pi|\ell|!}\right)^{1/2} \frac{1}{w(z)}\left(\frac{r\sqrt{2}}{w(z)}\right)^{|\ell|} e^{-r^2/(w(z))^2} e^{i(kz-kr^2/(2R))} e^{i\varphi(\ell)} \tag{4.7}$$

When $\theta = \frac{\pi}{4}$, the two circular bases have equal components. Then, the polarization states at the beam's transverse plane is linear. But the orientation angles of the linear polarization are spatial dependent in terms of $\ell\phi + \alpha$. The polarization distributions of two example cases are presented in Figure 4.7. Considering the case of $\ell = 1$, the structured beam is the well-studied radial vector beam for $\alpha = 0$, and the azimuthal vector beam for $\alpha = \frac{\pi}{2}$.

Since the resultant beam has inhomogeneous polarization distribution, which is determined by the design of the metasurface together with the polarization state of the incident light. The resultant beam generated by the superposition of LG modes with orthogonal circular polarization states can be diagnosed by passing it through a linear polarizer with orientation angle χ (with the horizontal). Accordingly, the transmitted intensity is proportional to $\cos^2(\ell\phi + \alpha - \chi)$, and it has 2ℓ minima at angles [140]

$$\phi_m = \frac{(2a-1)\pi}{2\ell} - \frac{\alpha}{\ell} + \frac{\chi}{\ell} \tag{4.8}$$

where $a = 1, 2, ...2\ell$. The simulated intensity profiles of the resultant beams after passing through a horizontal linear polarizer are presented in Figure 4.7 as well.

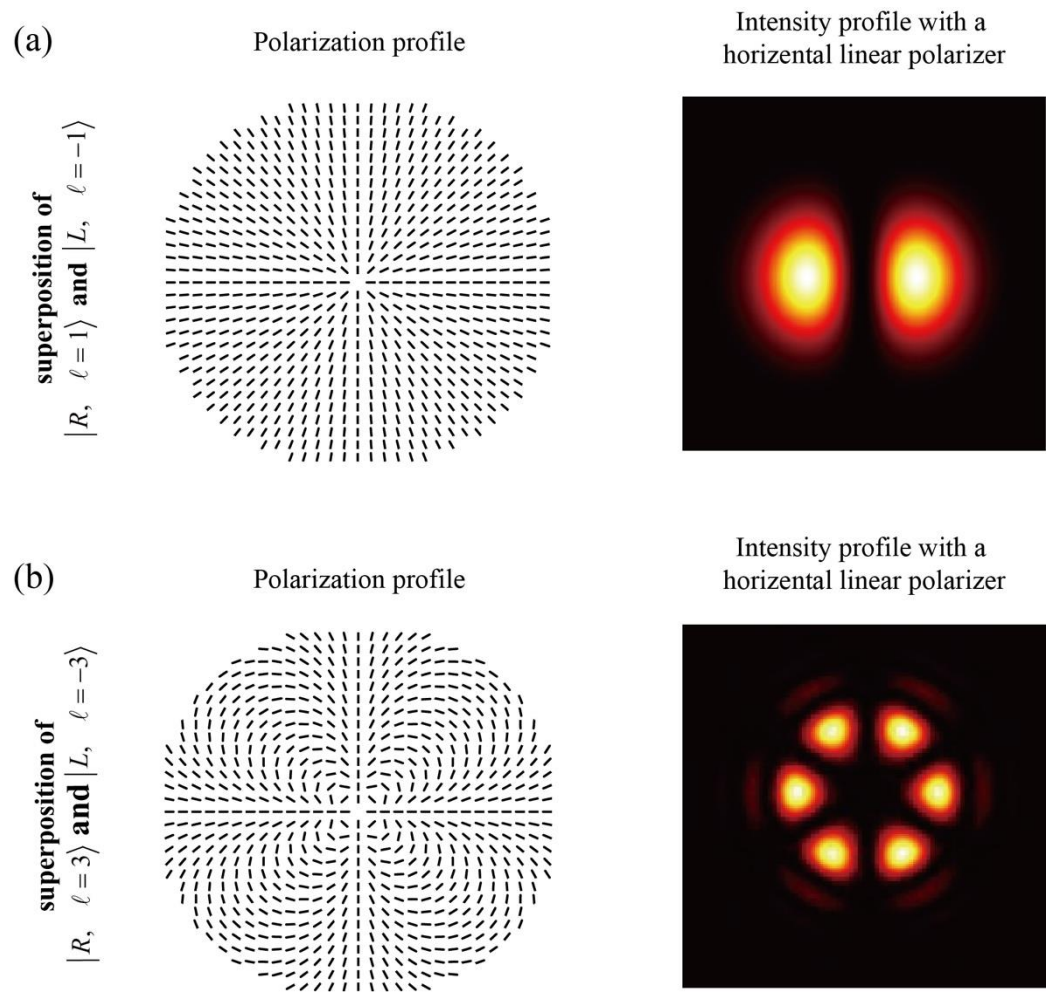

Figure 4.7. The polarization profile and the intensity profile of the resultant beam with the superpositions of (a) $|R,\ \ell=1\rangle$ and $|L,\ \ell=-1\rangle$, (b) $|R,\ \ell=3\rangle$ and $|L,\ \ell=-3\rangle$.

When θ is within the range of (0, π/4) or (π/4, π/2), the polarization states at every point of the light's transverse plane is elliptical. Moreover, the ellipticity is determined by θ, which is same with that of the incident light. The azimuthal angles of the spatial dependent elliptical polarization are determined by $\ell\phi + \alpha$. When $\theta = 0$ or $\theta = \pi/2$, the resultant beam is right- or left-handed circularly polarized Laguerre-Gauss modes, or vortex beams.

For the case of $\ell_1 \neq -\ell_2$, the equation (4.4) can be rewritten as

$$V = \frac{1}{\sqrt{2}} e^{i(\ell_1+\ell_2)\phi/2} (e^{i\delta} \cos\theta \cos\beta \left|R\right\rangle + e^{-i\delta} \sin\theta \sin\beta \left|L\right\rangle) \tag{4.9}$$

where

$$\beta = \tan^{-1}(\frac{G^{\ell_2}}{G^{\ell_1}}) \tag{4.10}$$

$$\delta = \frac{(\ell_1 - \ell_2)\phi}{2} + \alpha \tag{4.11}$$

Therefore, the polarization state at every point of the transverse plane of the beam is determined by the three parameters θ, β, δ. If $|\ell_1| < |\ell_2|$, the polarization state evolves from right circularly polarized to left circularly polarized when moving the position from centre to the edge of the beam (see Figure 4.8). Interestingly, when $\ell_1 = 0$ and $\ell_2 = 1$, the resultant beam refers to as full Poincaré beam, which has all states of polarization represented on the Poincaré sphere [122, 141].

By passing the resultant beam through a linear polarizer, the output beam becomes composite-vortex beam which contains a vortex of charge ℓ_1 in the centre of the beam surrounded by $|\ell_1 - \ell_2|$ singly charged peripheral vortices with the same sign of ℓ_2 located at the same radial distance [112]

$$d = \frac{w(z)}{\sqrt{2}} \left(\frac{\ell_2!}{\ell_1!} (\tan\theta)^2 \right)^{\frac{1}{2(|\ell_2|-|\ell_1|)}} \tag{4.12}$$

The right column of Figure 4.8 shows the intensity profile of the resultant beam with superpositions of $\left|R, \quad \ell = 1\right\rangle$ and $\left|L, \quad \ell = -3\right\rangle$, and $\left|R, \quad \ell = 2\right\rangle$ and $\left|L, \quad \ell = -4\right\rangle$ after passing through a horizontal linear polarizer.

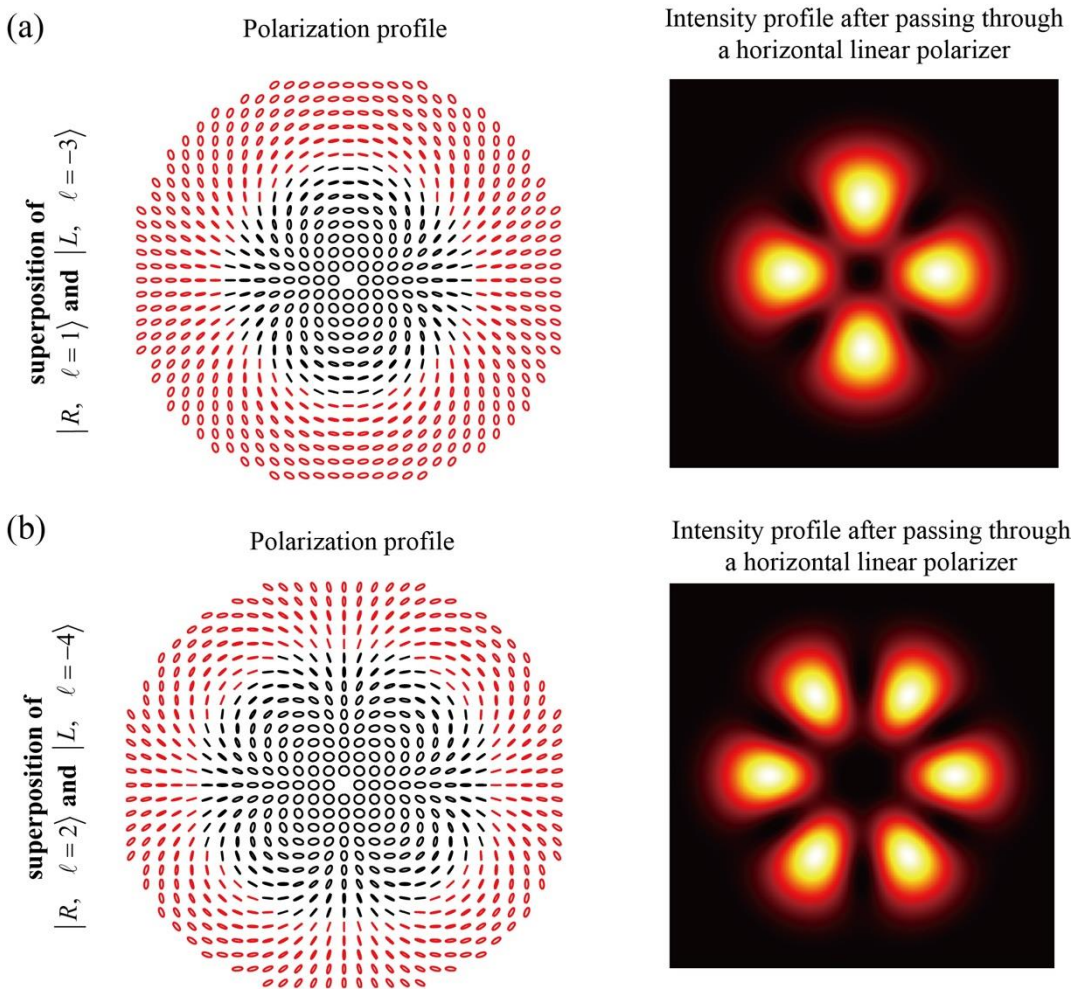

Figure 4.8. The polarization profile and the intensity profile of the resultant beam with the superpositions of (a) $|R,\ \ell=1\rangle$ and $|L,\ \ell=-3\rangle$, (b) $|R,\ \ell=2\rangle$ and $|L,\ \ell=-4\rangle$. The symbols with black colour represent the polarization state with right-handed helicity, and that of red colour represents the left-handed helicity.

4.2.3 The experimental results

To experimentally verify the proposed approach and inspect its flexibility, several metasurface samples for generating multiple OAM states are fabricated. The manipulations of the superposition of different OAM states in multiple channels are also characterized theoretically and experimentally. To clearly demonstrate the functionality of polarization controllable OAM modes superposition, the fundamental Poincaré sphere and Higher-order Poincaré sphere are employed to describe the polarization states of incident light and the Higher-order states of output light, respectively.

In experiment, the metasurface samples are mounted on a three-dimensional translation stage and exposed to the light from tuneable supercontinuum laser source (NKT-SuperK EXTREME) which covers a broad wavelength range. A Glan polarizer and a quarter-wave plate are inserted following the laser to generate the required polarization states. Then the collimated Gaussian beam impinges upon metasurface at normal incidence with a weak focus by a lens with a focal length of 100 mm. The measured intensity profiles of reflected output beams are captured using a colour CCD camera.

The first kind of metasurfaces realise superposition of OAM states with the same value but opposite signs in four output channels. The design is shown in Figure 4.7(a). Under the illumination of RCP light, two pairs of off-axis OAM beams are generated, i.e., (represented by black dots in horizontal direction) and (represented by red dots in vertical direction), respectively (see Figure 4.9(a))). Here ℓ_i and ℓ_j are the topological charges. By changing the incident circularly polarized light from RCP to LCP, the sign of topological charges of output OAM states is flipped from positive to negative (see Figure 4.9(b)), and the positions are swapped with respect to the centre (In practical, the propagating direction of two resultant OAM beams are swapped with respect to the incident axis.), accordingly. For a linearly polarized (LP) incident light which is the superposition of RCP and LCP components with equal weight, the states of the output beams generated by metasurface are $|R,\ \ell_i\rangle+|L,\ \ell_i\rangle$ and $|R,\ \ell_j\rangle+|L,\ \ell_j\rangle$, respectively. Then, the superpositions of OAM states are realised.

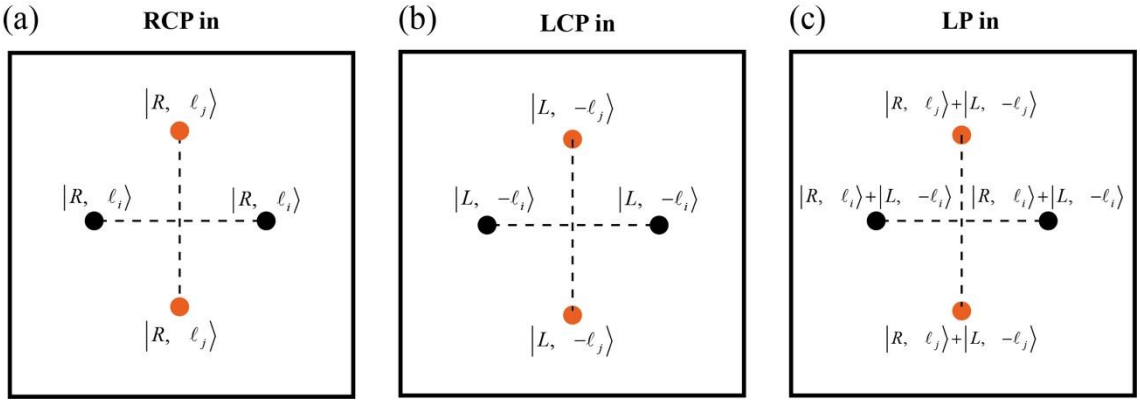

Figure 4.9. Schematic of the generation of two kinds of OAM modes and their superpositions in four channels. (a) For the case of incident beam with RCP, two pairs of off-axis OAM beams are generated, i.e., $|R,\ \ell_i\rangle$ (denoted by black dots) and $|R,\ \ell_j\rangle$ (denoted by yellow dots), respectively. (b) The signs of the topological charges of OAM

states and their positions are changed for the case of LCP input light. (c) OAM superpositions occur under the illumination of linearly polarized (LP) input light which is the superposition of LCP and RCP.

Figure 4.10 shows the metasurface that achieves two channels, i.e., channel 1 is the superposition of right-handed LG mode ($\ell=1$) and left-handed LG mode ($\ell=-1$), and channel 2 is the superposition of right-handed LG mode ($\ell=3$) and left-handed LG mode ($\ell=-3$). The scanning electron microscope (SEM) image of the metasurface is presented in Figure 4.10(a). In our experiment, we measure the resultant beams by recording the intensity profile at wavelength of 650 nm. It should be mentioned that these metasurface devices work in broad wavelength. Initially, the polarization state of the incident light is set with linear polarization. The output beam in channel 1 is the superposition of OAM modes with equal weight and opposite topological charges $\ell=1$ and $\ell=-1$. Moreover, the two OAM components have opposite circular polarizations. The output beam in channel 2 has the similar superposition states, but the topological charges are $\ell=3$ and $\ell=-3$. The combination of OAM beams with opposite topological charges and circular polarizations generate vector beams. The calculated polarization distribution can be found in Figure 4.7.

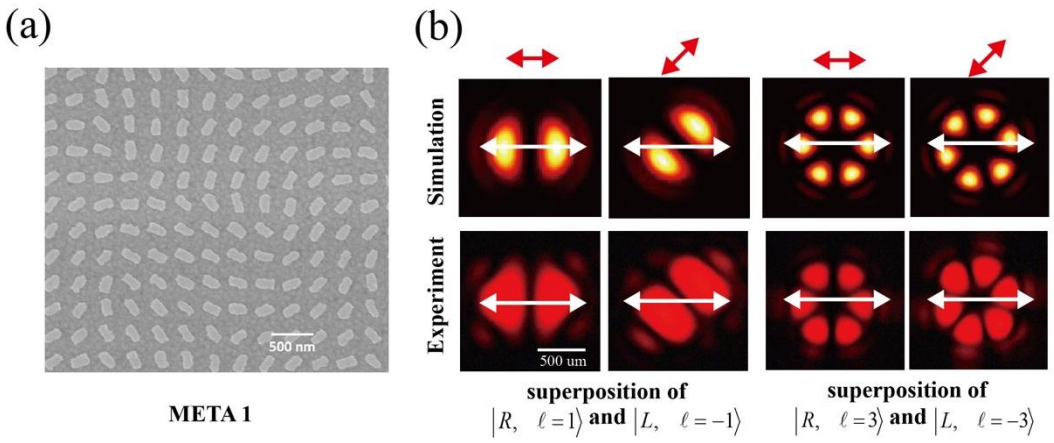

Figure 4.10. (a) The SEM image of the fabricated metasurface sample META 1. (b) The simulated and the experimentally observed intensity profiles of the superposition of OAM states after passing through a linear polarizer. The polarization angle of the incident linear polarized light and the transmission axis of the second polarizer in front of the CCD camera are denoted by the red and white double-headed arrows, respectively.

The superimposed OAM beams can be diagnosed by passing through a linear polarizer. We set the angle of the transmission axis of the polarizer is χ regarding *x*-axis. The Jones matrix can be written as

$$\begin{bmatrix} \cos^2\chi & \sin\chi\cos\chi \\ \sin\chi\cos\chi & \sin^2\chi \end{bmatrix} \tag{4.13}$$

Then the intensity profile after the polarizer can be calculated by [138]

$$\mathrm{E} = \frac{1}{2}\left[1+\cos^2\left(\ell\varphi+\vartheta+\chi\right)\right] \tag{4.14}$$

ϑ is the polarization angle of the incident linear polarized light. The transmitted intensity finds its minima at the azimuth angle $\varphi_n = \dfrac{(2n-1)\pi}{2\ell} - \dfrac{\vartheta}{\ell} - \dfrac{\chi}{\ell}$ and has $2|\ell|$ lobes, where $n = 1, 2, ...2\ell$. The number of lobes is double the absolute value of the topological charge. The positions of the minima are determined by the polarization angle of the incident light ϑ and the angle of the polarizer in front of the camera χ. A good agreement between the simulated and measured results are observed as shown in Figure 4.10. Note that the combination of $|R,\quad \ell=1\rangle$ and $|L,\quad \ell=-1\rangle$ with equal component can generate a radial or azimuthal vector beam, which has been found in various applications due to the unique properties [124, 125, 142].

Then we use a Glan polarizer (GP) and a quarter-wave plate oriented as suitable angles to generate the required polarization state as will. First, we generate five polarization states, i.e., 1) right-handed, 2) right-handed elliptically polarized, 3) horizontal linearly polarized, 4) left-handed elliptically polarized and 5) left-handed, which are geometrically represented on Poincaré sphere shown in Figure 4.11(a). The experimentally obtained results of resultant beams in two channels are also shown in this figure, which agree very well with numerical prediction. To further characterize the capability of arbitrary controlled superposition, we then set the Glan polarizer and the quarter-wave plate to introduce a retardation of $\pi/2$ between the circular polarization components of the input beam. By adjusting the Glan polarizer and a quarter-wave plate, the polarization states depicted in Figure 4.11(b) are generated at will. Consequently, the

introduced phase difference of $\pi/2$ between the eigenstates causes the rotation of the intensity profiles, which are theoretically predicted and experimentally verified.

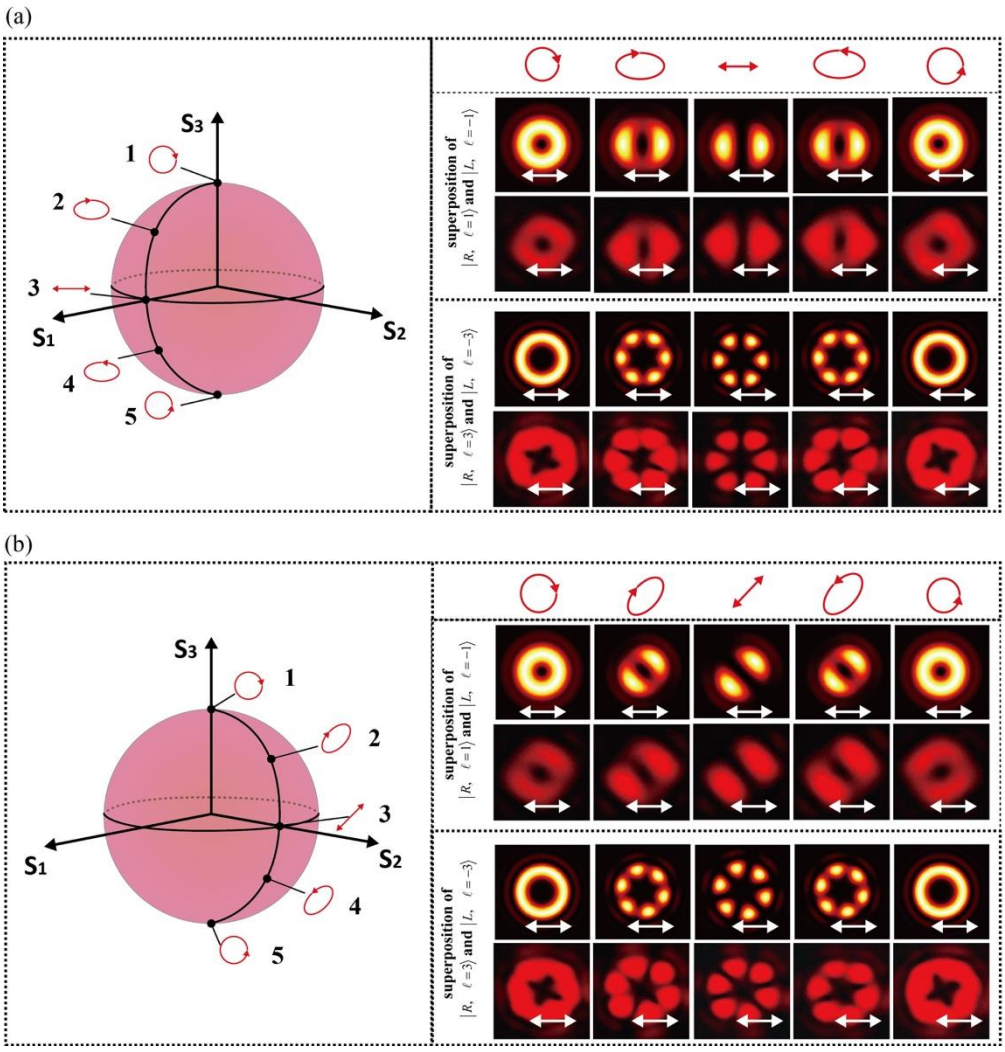

Figure 4.11 Simulated and experimental results of the polarization-controlled superposition of OAM modes. A linear polarizer is used to characterize the output beam. The transmission axis of this polarizer is denoted by the white double-headed arrows. Ten polarization states of the incident light are chosen along two different trajectories on the Poincaré sphere. The red symbols represent the polarization states.

To further confirm the metasurface approach for the realization of polarization-controlled OAM superposition, metasurface 2 (META 2) is fabricated to generate different superpositions from the first metasurface. Figure 4.12 illustrates the experimental results of the second metasurface which produce superpositions of OAM modes $\ell = \pm 2$ and $\ell = \pm 4$ in two channels, respectively. Figure 4.12(a) shows the SEM image of this metasurface. The experimental characterization for this sample is in a similar manner with

the first metasurface. Both the simulated and experiment intensities of resultant beams are presented in Figure 4.12 and 4.13. A superposition of equal intensities of left-handed and right-handed LG modes with topological charge ℓ forms a Hermite-Gaussian mode after a polarizer, which consists of $2|\ell|$ intensity lobes [138]. From Figure 4.10-4.13, we can see that the experiment results are in excellent agreement with the anticipated intensities.

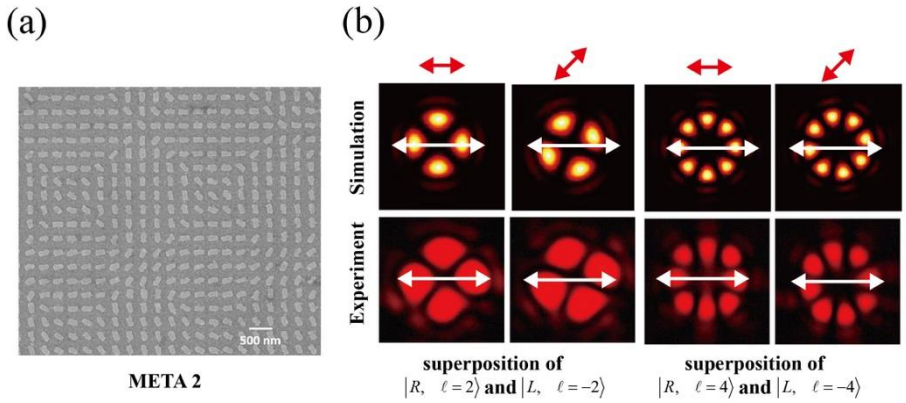

Figure 4.12. (a) The SEM image of the fabricated metasurface sample META 2. (b) The simulated and the experimentally observed intensity profiles of the superposition of OAM states, which are $|R\ \ \ell=2\rangle$ and $|L\ \ \ell=-2\rangle$, $|R\ \ \ell=4\rangle$ and $|L\ \ \ell=-4\rangle$, after passing through a linear polarizer. The polarization angle of the incident linear polarized light and the transmission axis of the second polarizer in front of the CCD camera are denoted by the red and white double-headed arrows, respectively.

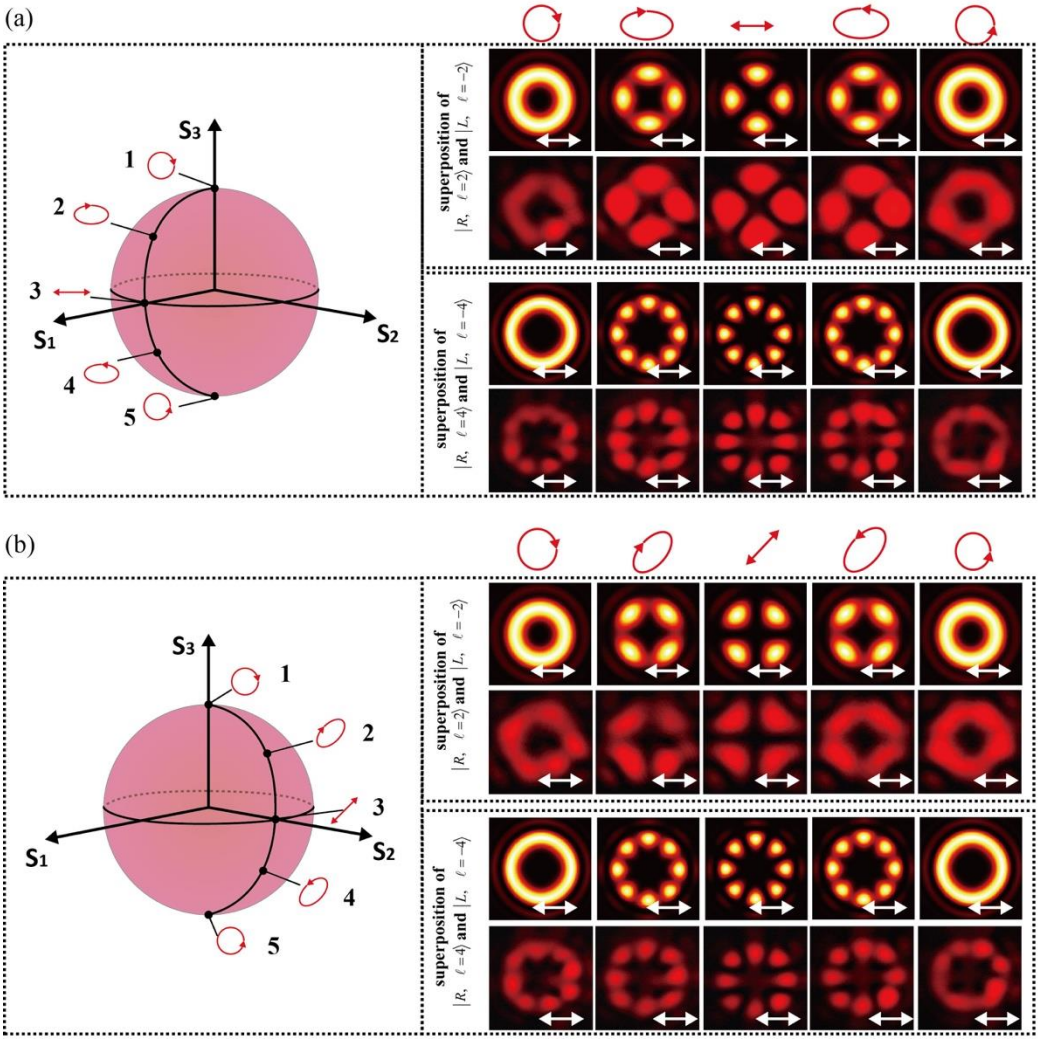

Figure 4.13 Simulated and experimental results of the polarization-controlled superposition of OAM modes in two channels, which are $|R \quad \ell=2\rangle$ and $|L \quad \ell=-2\rangle$, $|R \quad \ell=4\rangle$ and $|L \quad \ell=-4\rangle$, respectively. A linear polarizer is used to characterize the output beam. The transmission axis of this polarizer is denoted by the white double-headed arrows. Ten polarization states of the incident light are chosen along two different trajectories on the Poincaré sphere. The red symbols represent the polarization states.

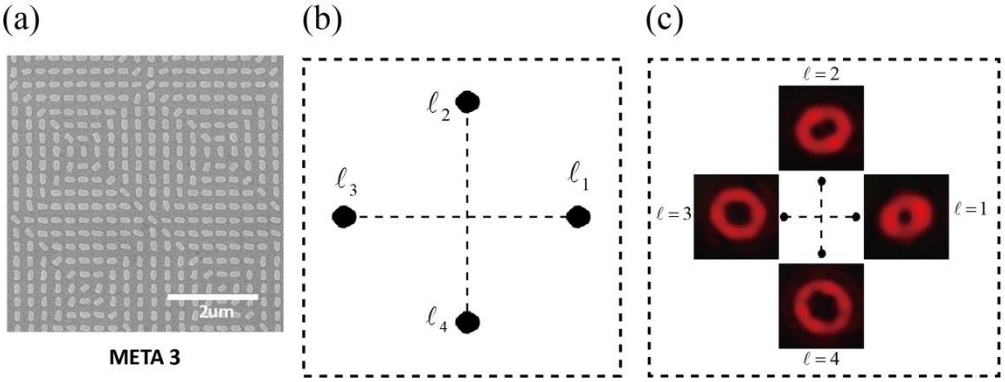

Figure 4.14. (a) The SEM image of the third metasurface sample for the generation of hybrid superpositions of OAM states. (b) Under the illumination of RCP light, four OAM beams with topological charges of ℓ_i ($i = 1, 2, 3, 4$) are generated. (c) The experimentally observed intensity profiles of four OAM beams.

In order to further explore the high performance and extend the functionality of this approach, the third metasurface is designed and fabricated, which not only generates four OAM modes from $\ell = 1$ to $\ell = 4$ for RCP Gaussian beam illumination (see Figure 4.14), but also four channels of hybrid superpositions of OAM states are realised. The SEM image is presented in Figure 4.14(a). Firstly, we measured the intensity profiles of the four OAM beams in four channels under the illumination of RCP Gaussian beam. Figure 4.14(c) shows the observed doughnut beams corresponding to four OAM modes from $\ell = 1$ to $\ell = 4$. Upon the illumination of linearly polarized light, the four channels correspond to four cases of superposition of SAM and OAM states, i.e.,

$$(\cos\theta \left| R, \quad \ell = 1 \right\rangle e^{-i\vartheta} + \sin\theta \left| L, \quad \ell = -3 \right\rangle e^{-i\vartheta}) \tag{4.15}$$

$$(\cos\theta \left| R, \quad \ell = 2 \right\rangle e^{-i\vartheta} + \sin\theta \left| L, \quad \ell = -4 \right\rangle e^{-i\vartheta}) \tag{4.16}$$

$$(\cos\theta \left| R, \quad \ell = 3 \right\rangle e^{-i\vartheta} + \sin\theta \left| L, \quad \ell = -1 \right\rangle e^{-i\vartheta}) \tag{4.17}$$

$$(\cos\theta \left| R, \quad \ell = 4 \right\rangle e^{-i\vartheta} + \sin\theta \left| L, \quad \ell = -2 \right\rangle e^{-i\vartheta}) \tag{4.18}$$

which are represented on different Hybrid-order Poincaré spheres. We characterize this metasurface under the similar process with previous experiment. Both the simulation and measurement results about the superposition of OAM modes $\left| R \quad \ell = 1 \right\rangle$ and $\left| L \quad \ell = -3 \right\rangle$ are illustrated in Figure 4.15. The upper rows show the simulated and measured intensity profiles without a polarizer in front of the camera. We can see from the results that the diameter of dark hole in the centre of the obtained profiles increases with continuously changing the polarization state of the incident light from RCP to LCP, which indicates that the output beam evolves from the OAM state with $\ell = 1$ to OAM state with $\ell = 3$. For the case of incident light with elliptical and linear polarization, the resultant beam is the

superposition of the two OAM modes. Since the polarization states of the two components are orthogonal, there is no interference between them. The doughnut shape of the intensity profile remains during the change of polarization.

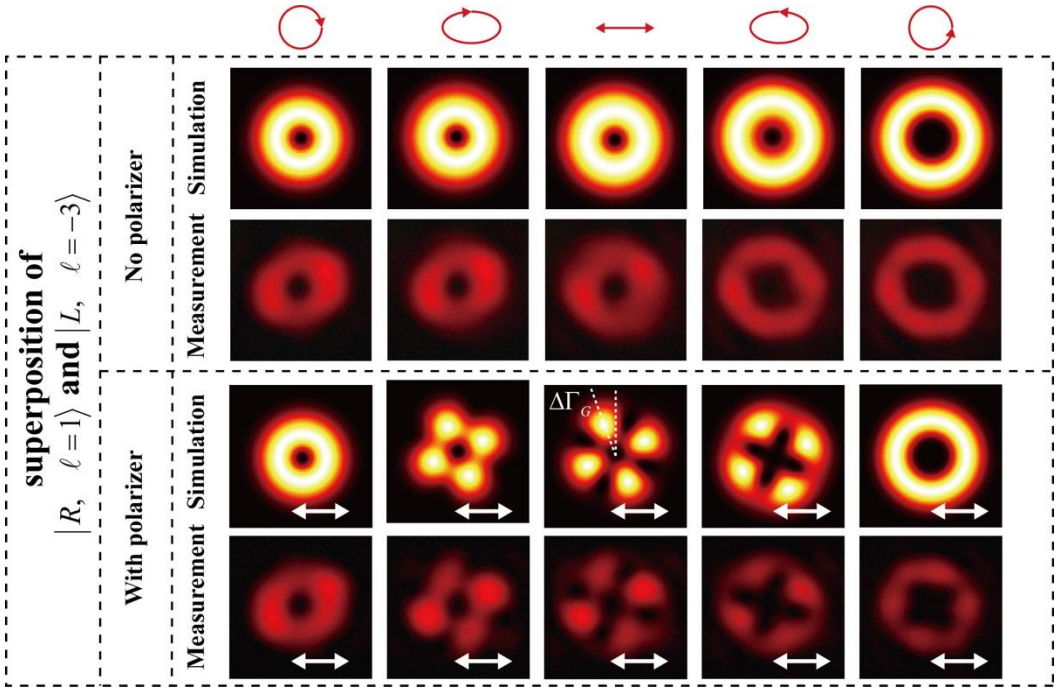

Figure 4.15 Simulated and experimentally recorded intensity profiles of the hybrid superposition of OAM modes $|R\ \ \ell=1\rangle$ and $|L\ \ \ell=-3\rangle$. $\Delta\Gamma_G$ is the Gouy rotation introduced by the Gouy phase difference between the two OAM components during propagation.

The performance of the approach is further verified by transmitting the output beam through a horizontal linear polarizer as shown in the bottom rows of Figure 4.15. The experiment results agree well with the simulated results. It should be noted that the rotation of the intensity profile $\Delta\Gamma_G$ is observed, which is caused by the ℓ-dependent Gouy phase [143, 144]. The Gouy phase shift is the axial phase shift that a converging light wave experiences as it passes through its focus in propagating from $-\infty$ to $+\infty$ [144]. During the propagation of the LG beam along the optical path after focus, it acquires a ℓ-dependent Gouy phase which is proportional to the fundamental Gouy phase $\tan^{-1}(z/z_R)$. The ℓ-dependent Gouy phase can be given by

$$\Phi_G = (2p+|\ell|+1)\tan^{-1}(z/z_R) \tag{4.19}$$

Here we consider the case of $p=0$, the field distribution of the beam is a single ring that contains a phase vortex of charge ℓ at the beam axis. When the composite beam formed by collinear superpositions of LG beams with topological charges of ℓ_1 and ℓ_2 propagates, the intensity profile rotates about the beam axis if $|\ell_1| \neq |\ell_2|$. Since there is Gouy phase difference between the component beams. When $|\ell_1| = |\ell_2|$, there is no rotation, which is verified in Figure 4.12. More details about the explanations can be found in Ref. [112]. The simulated and experiment results on the superposition of $|R \quad \ell=2\rangle$ and $|L \quad \ell=-4\rangle$ are shown in Figure 4.16.

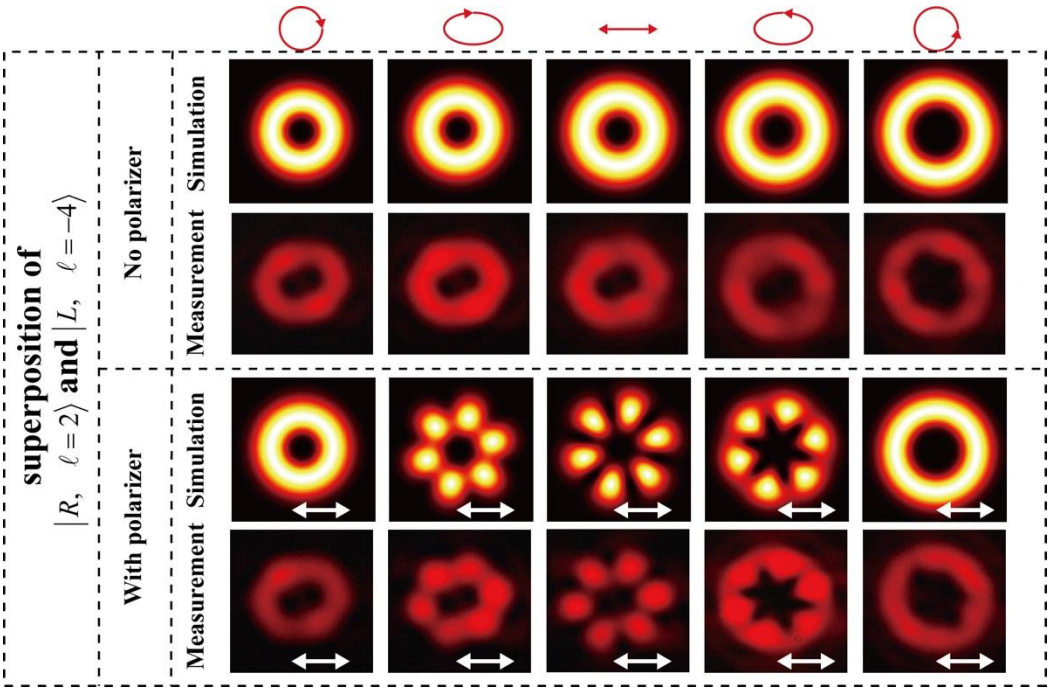

Figure 4.16. Simulated and measured intensity profiles of superposition of OAM states $|R, \quad \ell=2\rangle$ and $|L, \quad \ell=-4\rangle$. The polarization state of the incident light is denoted by red symbols. The direction of the polarizer's transmission axis in front of the CCD camera is denoted by the white double-headed arrows.

This approach also provides the capability for multiplexing massive individual orbital angular momentum beams using single metasurface with miniature size, paving the way for highly compact meta-devices in optical communication systems [105]. Furthermore, this approach offers the opportunity to explore the physical process about multipartite quantum entanglement of photons both in their spin and orbital angular momentum degrees of freedom [145].

Chapter 5 – GEOMETRIC METASURFACE FOR POLARIZATION CONTROL

The coherent superimposition of two orthogonal circular polarizations can generate arbitrary polarization by adjusting the intensity ratio and phase difference between them. This basic rule provides the capability to control the polarization state of the output light at the subwavelength scale in the manner of phase and amplitude change introduced by nanoantennas. Considering the example of geometric metasurface consisting of nanopattens with identical geometry but different orientations. Due to the spin-rotation coupling, the phase of the output light is determined by the orientation of the nanoantenna. Moreover, the sign of the phase change depends on the helicity of the light. Thus, the polarization angle and phase of the linear polarization can be controlled in subwavelength scale through governing the phase difference between the two circular components. It should be noted that the ellipticity cannot be engineered in this way since the amplitude of the scattering field remain same for both the two circularly polarized light. To demonstrate the linear polarization control using metasurface, we proposed and designed two different approaches using metasurfaces. The first is about the generation of vector vortex beam with a single metasurface [119]. This method features the spin-rotation coupling and the superposition of two circular components which are the converted part with an additional phase pickup and the residual part without a phase change. Both the orbital angular momentum and polarization distribution in the transverse plane about the propagation axis are manipulated by a single metasurface consisting of nanorods with spatially variant orientation. As this approach solves several major issues typically associated with vector vortex beam generation such as poor resolution, low damage threshold, bulky size, and complicated experimental setup, it opens a new window for future practical applications of the structured beams in the relevant research fields such as optical communication, particle trapping, microscopy, and quantum optics. The second approach is to spatially manipulate the phase of the two circular components simultaneously to control the polarization distribution of the resultant beam [146]. Based on this method, we propose and experimentally demonstrate a metasurface approach to encode a high-resolution image in a laser beam. This approach provides a novel route to hide a high-resolution grayscale image in the polarization topology of a laser beam that has not previously been reported in the literature. The uniqueness of image-hidden functionality and precise polarization manipulation, and high performance in resolution,

bandwidth, and compactness renders this technology very attractive for diverse applications such as encryption, anti-counterfeiting, and optical communications.

5.1 Vector Vortex Beam Generation Using Single Metasurface

Vortex beams and vector vortex beams have been widely investigated due to their distinguished features. Vortex beams have a distribution of azimuthal phase and homogeneous polarization, while vector vortex beams have azimuthal phase and polarization dependence at the transverse plane of the light beams. Vortex beams and vector vortex beams have been found in various applications including particle trapping quantum memories, high-resolution lithography, and optical communication. In this section, we demonstrate an approach to generate the vector vortex beam using metasurface. The designed metasurfaces can generate cylindrical vector vortex beams carrying orbital angular momentum. The vector vortex beams are obtained using the superposition of the converted part and the residual part of the output beam [119]. Figure 5.1 shows the schematic of the vector vortex beam generation. For an incident light beam with right-handed circular polarization (RCP), part of the input beam is converted and acquired spatially dependent abrupt phase changes. In contrast, the residual beam has no phase change but the opposite helicity polarization in comparison with that for the converted part. The output beam is therefore a superposition of two components, and the polarization distribution is transformed to a radial vector field. The generated vector vortex beam (VVB) carries OAM $\ell = 1$.

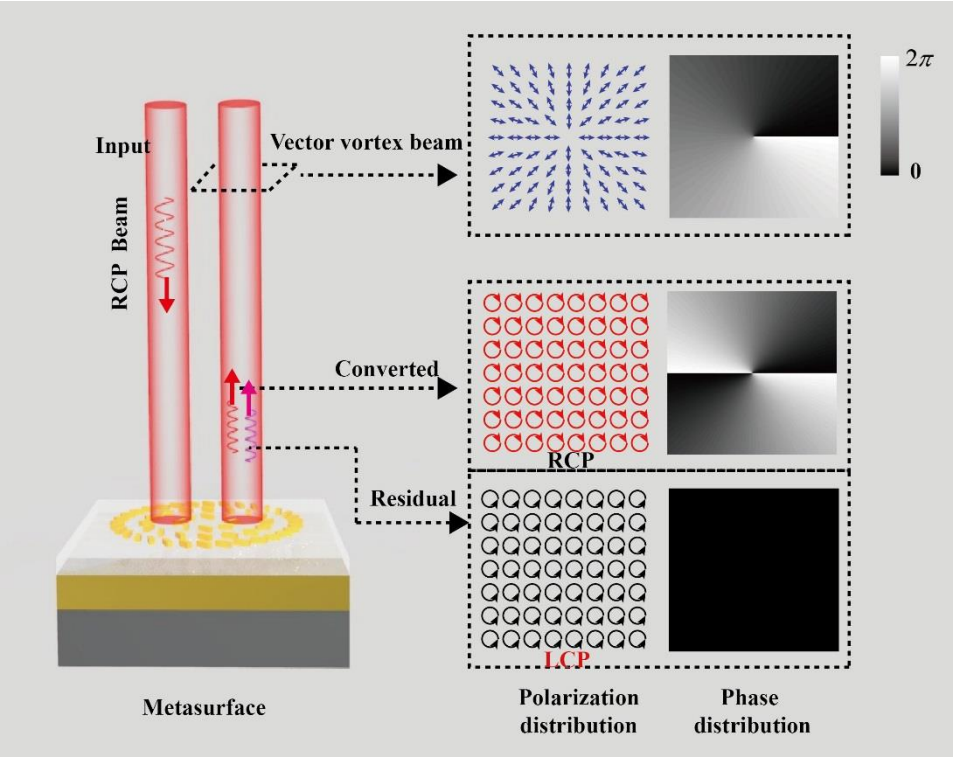

Figure 5.1 Schematic of the vector vortex beam generation through a metasurface. The resultant beam is a superposition of the converted part and the residual part. The converted part has the same circular polarization as that of the incident beam and obtains an additional phase pickup. Whereas the residual part has the opposite helicity but no phase change. With the RCP incident light, the converted beam has a helical wavefront with a topological charge of $\ell = 2$ and the resultant beam has radial polarization distribution with the OAM of $\ell = 1$.

5.1.1 Design of the metasurface

It is evident that any state of complete polarization on the fundamental Poincaré sphere can be described as a superposition of left- and right-handed circularly polarized light, which refer to spin eigenstates. By extending the basis of states in terms of the optical SAM to the total optical angular momentum that includes the higher dimensional orbital angular momentum (OAM), the vector vortex beam can be constructed from a coaxial superposition of two spin-orbital eigenstates with different values.

To generate VVB, we design and fabricate a reflected-type metasurface that simultaneously generate two eigenstates, i.e., the converted part and residual part, with pre-designed phase difference between them. The metasurface has the metal-dielectric-metal configuration with the top layer of nanorods with space-variant orientation. The high efficiency of this configuration has already been discussed in Chapter 2 and 3. The detailed information can be found in Ref. [16] and [15].

Here, the orientation angle of nanorods can be specified by the following expression

$$\alpha(r,\phi) = q\phi + \alpha_0 + \frac{\pi}{4} \tag{5.1}$$

where (r,ϕ) is the polar coordinate representation, and q is an integer related to the difference of topological charge for two eigenstates($|\ell_2| - |\ell_1| = \pm 2q$). α_0 is the initial angle related to the phase difference of two eigenstates. When a circularly polarized Gaussian beam impinges onto the metasurface, part of incident light will be converted into the opposite circularly polarized light. The change in the SAM is transformed into OAM [12]. Therefore, the emerging beam is converted into Laguerre-Gauss beam carrying orbital angular momentum, whereas the intensity distribution of residual beam

is still Gaussian. This process is inherently geometry dependent and occurs in a sub-wavelength scale. By carefully designing the structure of the metasurface, the converted beam and residual beam serve as two eigenstates. Hence, the resultant beam can be expressed as

$$E_{output}(r,\phi) = LG_{0,0}(r,\phi)\begin{bmatrix}1\\ \sigma i\end{bmatrix} + LG_{0,2\sigma q}(r,\phi)\bullet\exp(-i\alpha_0)\begin{bmatrix}1\\ -\sigma i\end{bmatrix} \tag{5.2}$$

where $LG_{0,0}(r,\phi)$ and $LG_{0,2\sigma q}(r,\phi)$ represent the intensity distributions of fundamental Gaussian beam with zero topological charge and Laguerre-Gauss beam with topological charge of $2\sigma q$, respectively. α_0 is the phase difference between these two modes. $\sigma = \pm 1$ stand for the cases of right- and left-handed circularly polarized light, respectively.

5.1.2 Polarization and phase evolution on a single-pixel cell structure.

A single-pixel cell structure is functionally similar with a reflective-type half-wave plate with fast axis parallel to the major axis of nanorod as shown in Figure 5.2. The Jones matrix of reflective-type half-wave plate is given by

$$J_{(\lambda/2,\ \phi)} = i\begin{bmatrix}\cos 2\phi & \sin 2\phi\\ \sin 2\phi & -\cos 2\phi\end{bmatrix} \tag{5.3}$$

where ϕ is the angle between the fast axis of half-wave plate and the horizontal axis. In normal case, the factor i is usually suppressed since we only consider the converted part. However in this case it can't be ignored since the phase difference with regard to incident wave is the key point. When a pure circularly polarized light impinges normally upon the half-wave plate, the reflection beam is in general a superposition of two components with orthogonal circular polarization states: the converted part with an abrupt phase change, and the non-converted part with no phase change. First we consider the RCP incident light. Its normalized Jones vector is $E^{RCP} = \frac{1}{\sqrt{2}}\begin{bmatrix}1\\ i\end{bmatrix}$. The Jones vector of converted light could be derived by multiplying the Jones vector and equation (5.3). Assuming that part of incident light is converted and we find that

$$E_{Con}^{RCP} = J_{(\lambda/2,\ \phi)} \bullet \frac{A}{A+B} E^{RCP} = \frac{1}{\sqrt{2}} \frac{A}{A+B} e^{i(2\phi+\frac{\pi}{2})} \begin{bmatrix} 1 \\ -i \end{bmatrix} \tag{5.4}$$

where A and B represent the amplitudes of converted and residual light, respectively. From equation (5.4), we can see that the incident RCP light is converted to LCP light with an additional phase $(\frac{\pi}{2} + 2\phi)$.

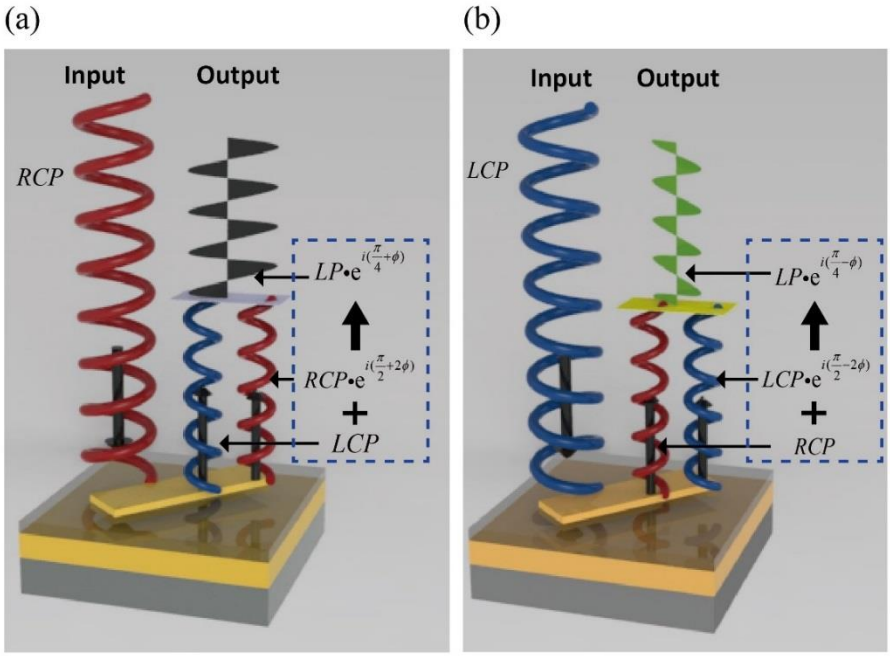

Figure 5.2. Illustration of polarization and phase evolution of emerging light on a single-pixel cell structure. For the circularly polarized incident light, the emerging light is the superposition of two orthogonal circularly polarized beam which are the converted wave (same handedness with that of incident beam) and non-converted wave (opposite handedness with that of incident beam), respectively. Spiral curved line in red colour stands for right-handed circularly polarized light (RCP), and that in blue colour stands for left-handed circularly polarized light (LCP). (a) The case of RCP input light. (b) The case of LCP input light.

The term 2ϕ is the Pancharatnam-Berry phase. The term $\frac{\pi}{2}$ is an overall phase delay introduced by the half-wave plate. It should be noted that the handedness of polarized light is reversed when it is reflected by an ideal mirror because of opposite direction of

propagation. Thus, the converted wave maintains the handedness of incident light as RCP but with additional phase $(\frac{\pi}{2}+2\phi)$. The Jones vector is

$$E_{Con}^{RCP}=\frac{1}{\sqrt{2}}\frac{A}{A+B}e^{i(2\phi+\frac{\pi}{2})}\begin{bmatrix}1\\ i\end{bmatrix} \tag{5.5}$$

The non-converted wave only experience handedness flip and the Jones vector can be given by

$$E_{Non-con}^{RCP}=\frac{1}{\sqrt{2}}\frac{B}{A+B}\begin{bmatrix}1\\ -i\end{bmatrix} \tag{5.6}$$

The emerging beam is the superposition of converted (E_{Con}^{RCP}) and non-converted wave ($E_{Non-con}^{RCP}$). If the converted and residual component have equal intensity ($A=B$), the resultant beam gives rise to linearly polarized light and also acquires a phase change. It can be expressed as follows (see Figure 5.2(a))

$$E_{out}^{RCP}=\frac{1}{2}(E_{Con}^{RCP}+E_{Non-con}^{RCP})=\sqrt{2}e^{i(\frac{\pi}{4}+\phi)}\begin{bmatrix}\cos(\frac{\pi}{4}+\phi)\\ -\sin(\frac{\pi}{4}+\phi)\end{bmatrix} \tag{5.7}$$

A similar derivation takes place when the polarization state of incident light is LCP (Figure 5.2(b)). The Jones vector of emerging beam is

$$E_{out}^{LCP}=\sqrt{2}e^{i(\frac{\pi}{4}-\phi)}\begin{bmatrix}\cos(\frac{\pi}{4}-\phi)\\ \sin(\frac{\pi}{4}-\phi)\end{bmatrix} \tag{5.8}$$

The superscripts in equations (5.4-5.8) represent the polarization state of incident light. From equations (5.7) and (5.8), we can see that the resultant beam gives rise to linearly polarized light and acquires a phase change under the illumination of LCP or RCP light. More importantly, both the polarization angle and phase change are dependent on the

orientation angle of nanorods and the handedness of incident light. In addition, an overall $\frac{\pi}{4}$ shift is introduced by the half-wave plate [120].

5.1.3 The simulation and experimental results

To verify the idea, two metasurface samples with different values of α_0 are designed and fabricated by means of the similar fabrication process. Here $q=1$. Initially, the first sample with $\alpha_0 = 0°$ is characterized. Figure 5.3(a) shows the measured normalized power of the two eigenstates over a wide range of wavelengths. The inset is the SEM image of the fabricated sample. The two curves overlap at the wavelength of 697 nm, which means that the converted and residual part have equal components at this wavelength and the VVB is realised. By passing through a linear polarizer with different transmission angles, the generated structured beams from the fabricated metasurface are characterized and validated. Figure 5.3(b) shows the simulated and measured intensity distribution of vectorial vortex beam after passing through an analysing polarizer in horizontal, 45°, vertical, and -45 ° orientations at the wavelength of 697 nm. The appearance of '*s*' shape patterns is theoretically predicted and experimentally confirmed. The observed patterns indicate that the resultant beams indeed have an inhomogeneous polarization distribution and a helical wavefront. The simulated intensity patterns of vector beams with different OAM can be found in Figure 5.4. Moreover, the twisted direction of the '*s*' shape varying with the helicity of circular polarization are also experimentally confirmed from the obtained intensity patterns.

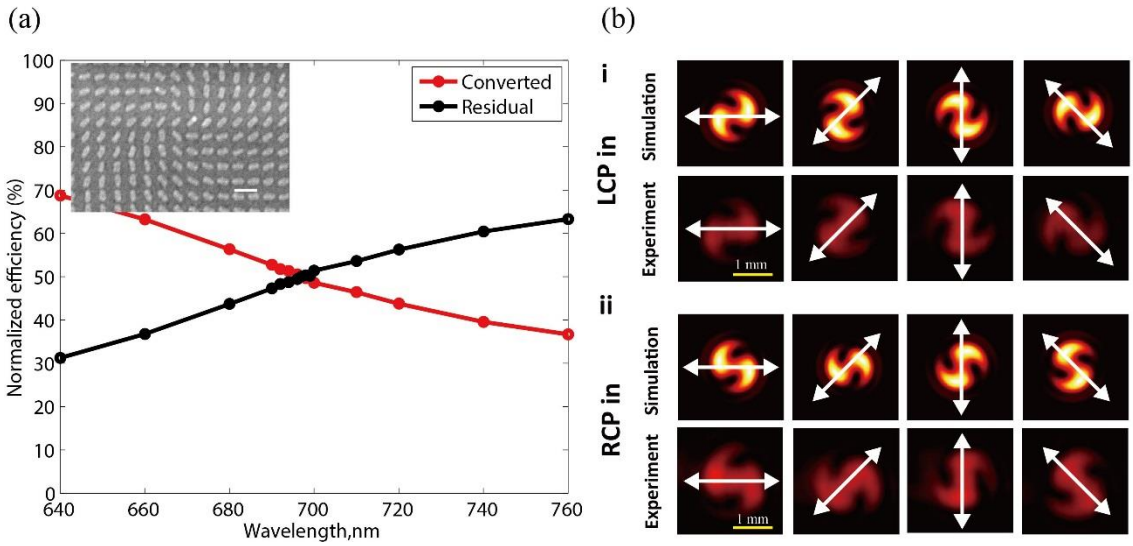

Figure 5.3. Measured power (normalized) of converted and residual parts at various wavelengths, and intensity patterns of vector vortex beam after passing through a linear polarizer. (a) The measured power (normalized) of converted and residual parts at various wavelengths. The inset is the SEM image of the metasurface for vector vortex beam generation. The scale bar is 500 nm. (b) Simulated and experimentally recorded intensity profile of the vector vortex beam after passing through a polarizer with different polarization angles including horizontal, diagonal, vertical, and antidiagonal directions. The polarization angles are denoted by white double-headed arrows. i, LCP light input, ii, RCP light input.

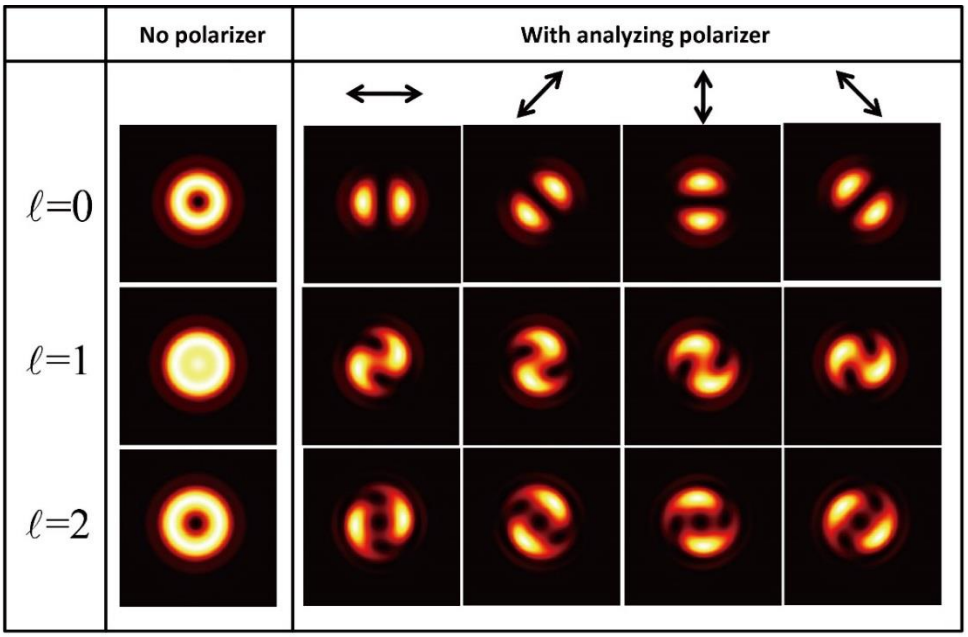

Figure 5.4. Simulated intensity distributions of vector beams with different topological charges.

5.1.4 The validation of the OAM

In Chapter 2, we discussed that the Generalized Snell's law and the phase gradient metasurface (PGM). Due to the spin dependent phase manipulation, the PGM can work as a circular beam splitter. Here, we employ a PGM in experimental setup that allow us, without the need of any additional polarizer and waveplate, to simultaneously decompose the output beam from the metasurface. Since the two eigenstates have the opposite circular polarization states.

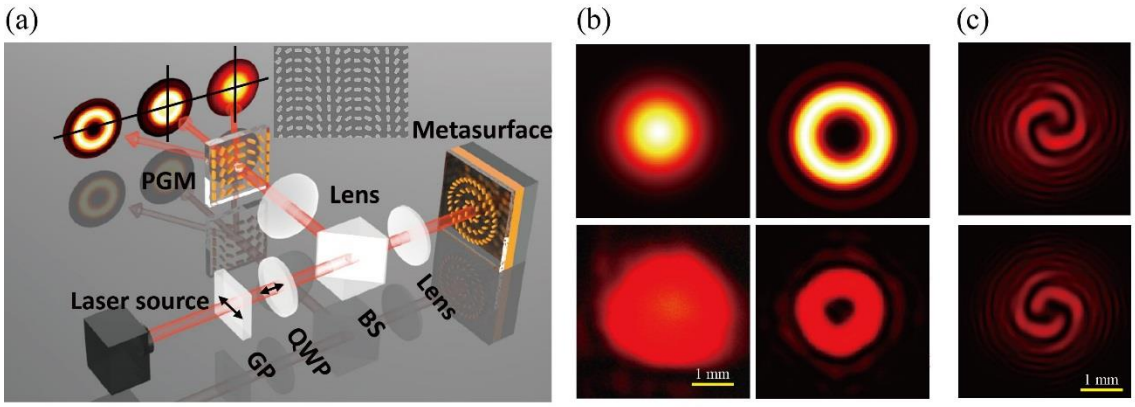

Figure 5.5. Experimental setup, and the theoretically predicted and measured intensity distribution of the two components. (a) Schematic of the experimental setup. A charge coupled device (CCD) camera is used to image the output beams. The inset is the SEM image of fabricated phase-gradient metasurface. (b) Simulated (top) and measured (bottom) intensity profiles of the two components. (c) Spiral patterns created by the interference of the vortex beam and a co-propagating Gaussian beam. The polarization states of incident light are LCP (upper image) and RCP (lower image), respectively.

The schematic of experimental setup is depicted in Figure 5.5(a). The metasurface sample for the VVB generation is mounted on a three-dimensional translation stage and exposed to the laser beam. A Glan polarizer and a quarter-wave plate are used to generate the required circularly polarized light. In order to collect the reflected light, a polarization-insensitive beam-splitter (BS) is inserted between the QWP and the lens. The reflected vector vortex beam is either projected to PGM to decompose the resultant beam, or propagates in the free space for further application. The SEM image of the PGM is shown in Figure 5.5(a) (see inset). The simulated and obtained intensity distributions of two components are shown in Figure 5.5(b). The doughnut shape and singular point confirm the existence of optical vortex (right in Figure 5.5(b)), which corresponds to the converted light. The residual part (left in Figure 5.5(b)), on the other hand, is confirmed by the shape without a singularity in the light spot. To further reveal the spiral wavefront and verify the OAM of optical vortex, the PGM is replaced by the circular polarization filter consisting of a quarter-wave plate and a linear polarizer. We deliberately let both the converted and residual beam partially pass the filter by tuning the angle of the quarter-wave plate and linear polarizer. The residual beam serves as the reference spherical wave to interfere with the converted vortex beam. The double helical intensity profile and the number of branches stemming from the singularity confirm that the converted beam carries orbital angular momentum of $2\hbar$.

The proposed method provides an unusual way to generate vector vortex beam carrying orbital angular momentum using a single metasurface, which will inspire the pursuit of further novel functionalities. To our knowledge, this is the first time that the converted part and the residual part are used together to realise new functionalities. Both the phase and polarization are manipulated at subwavelength scale by the artificial array of engineered nanorods over the metasurface. We develop two metasurfaces with different initial angles ($\alpha_0 = 0$ and $\alpha_0 = \pi$), which can generate radially and azimuthally polarized vortices carrying orbital angular momenta, respectively. The SEM image of the second metasurface with $\alpha_0 = \pi$ and results are shown in Figure 5.6. The good agreement between predicted and experimental results confirms the proposed methodology. It has been reported that azimuthally polarized beams with helical wavefront could effectively achieve a significantly smaller spot than normal azimuthally polarized beams when focused with a high-numerical-aperture lens.

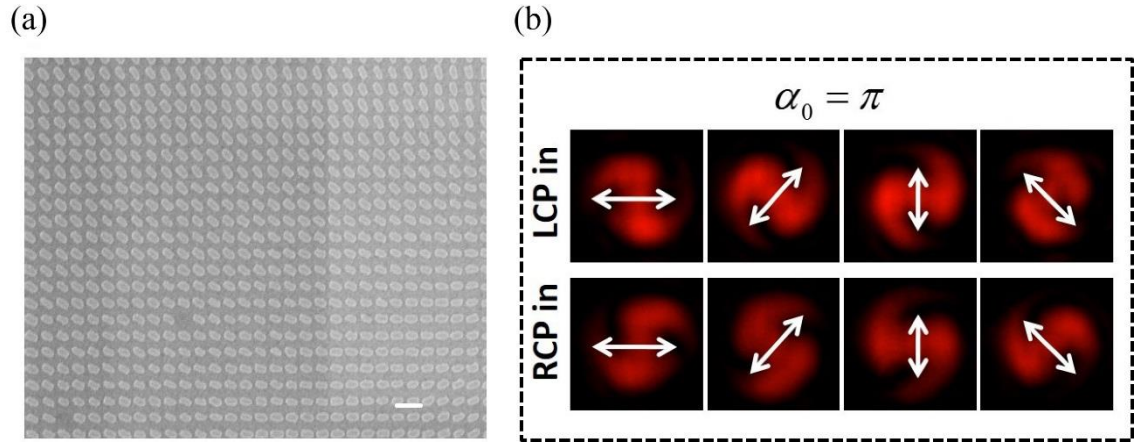

Figure 5.6. (a) SEM image of fabricated metasurface with $\alpha_0 = \pi$. (b) the experimental results. The scale bar is 500 nm.

For the application of free space communication, the optical vortex has attracted growing attention due to its higher data transmission capacity. However, the atmospheric turbulence strongly affects the properties of the optical vortex when propagating in free space. The existence of the vectorial vortex can be identified with longer propagation distance through atmosphere than the scalar vortex even with vanishing characteristic vortex structure [147]. By carefully designing the angle distribution of nanorods, the manipulation of polarization profile can be realised using a single metasurface with the circularly polarized incident light. In addition, the resultant polarization distribution is switchable by controlling the helicity of the circularly polarized incident light.

5.2 Hiding a Grayscale Image on a Laser Beam

In this section, we demonstrate the second approach to control the transverse polarization profiles. Moreover, we encode a high-resolution grayscale image into the spatially variant polarization states of the laser beam, which can be revealed after passing through a linear polarizer. The desired space-variant polarization profile originates from the superposition of two circularly polarized beams with opposite handedness and space-dependent phase difference emerging from a single metasurface.

5.2.1 The design method

The required light beam with an inhomogeneous linear polarization profile can be decomposed into the superposition of two circularly polarized beams with equal components and opposite handedness, which can be described as

$$\begin{aligned}\vec{E}(x,y) &= E_0[\vec{x}\cos\varphi(x,y)+\vec{y}\sin\varphi(x,y)] \\ &= \frac{E_0}{\sqrt{2}}[\exp(i\varphi(x,y))\hat{e}_R+\exp(-i\varphi(x,y))\hat{e}_L]\end{aligned} \tag{5.9}$$

where $\varphi(x,y)$ represents the relative phase difference between the two orthogonal circular polarization states, $\hat{e}_L=(x+iy)/\sqrt{2}$ and $\hat{e}_R=(x-iy)/\sqrt{2}$ are unit vectors of the left circular polarization and the right circular polarization. A geometric metasurface is used to realise the handedness-dependent phase profile while maintaining constant amplitude. Here, a single reflective metasurface is designed to generate the desired structured beams by manipulating the superposition of two beams with opposite circular polarization states emerging from the identical metasurface.

Figure 5.7 shows the schematic to generate the required linear polarization profile. To eliminate the effect of the non-converted beam, we adopt the off-axis configuration in this design. A general linear polarization topology can be generated by a coherent superposition of two planar circularly polarized beams with opposite handedness, which propagate along the same direction. The key point here is to generate a phase profile that, upon the illumination of circularly polarized light, can simultaneously generate a pair of centro-symmetrically distributed off-axis beams with same phase profile with respect to the propagation axis of the incident light (see Figure 5.7(i)). The required phase distribution is governed by

$$\Phi(x,y) = \arg(\exp(i(\varphi(x,y)+\delta(x))) + \exp(i(\varphi(x,y)-\delta(x)))) \tag{5.10}$$

where $\varphi(x,y)$ represents the position-dependent phase difference between the two orthogonal polarization states. $\pm\delta(x)$ is an additional phase profile, which is used to produce the phase gradient along *x* direction for the off-axis reflection (±1 order). The angle of reflection is determined by the generalized Snell's law of reflection. The detailed discuss can be found in Chapter 2. Since the sign of the geometric phase generated at the interface of the metasurface depends on the handedness of the incident circularly polarized light, when the incident beam is changed from RCP to LCP, a pair of off-axis beams with the phase profile $-\Phi(x,y)$ are generated accordingly (Figure 5.7(ii)). Obviously, under the illumination of linearly polarized light beam, the reflected beams with opposite handedness will meet and generate the desired polarization profile as shown in Figure 5.7 left.

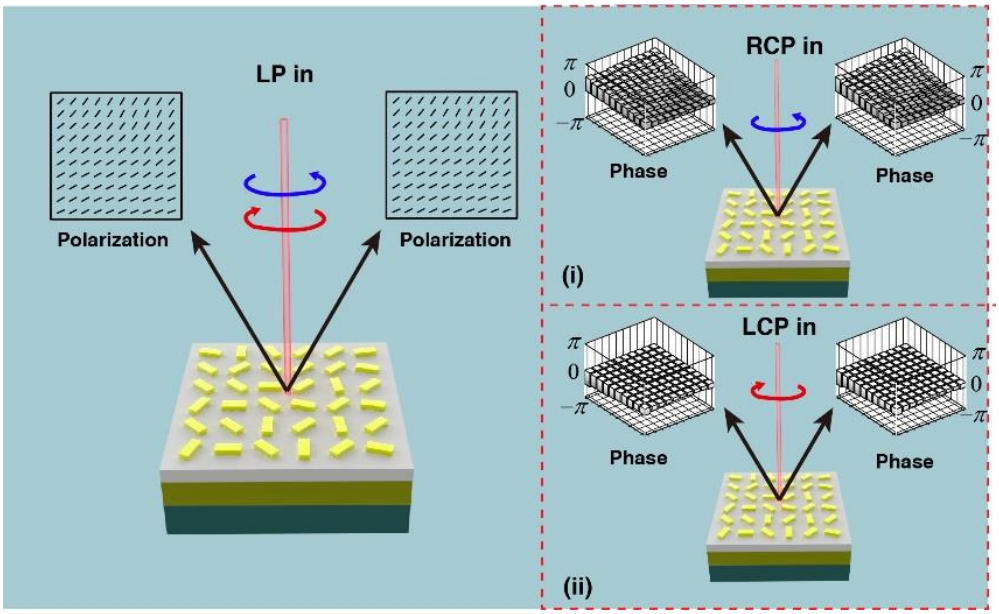

Figure 5.7. Mechanism of the polarization manipulation via the metasurface. The polarization states of incident beam in (i) and (ii) are right circular polarization and left circular polarization, respectively. A pair of off-axis beams with phase profile $\Phi(x,y)$ (or $-\Phi(x,y)$) are generated by shining the metasurface with light beam with RCP (or LCP). When a linearly polarized (LP) beam is incident on the metasurface, the reflected beam with opposite circular polarization and equal components will meet and generate the required polarization profile on both sides (Figure 5.7 left).

According to Malus' Law, when a linearly polarized light beam passes through an analyser (linear polarizer), the intensity of the light transmitted by the analyser is directly proportional to the square of the cosine of angle θ between the transmission axes of the analyser and the polarizer (see Figure 5.8(a)), i.e., $I = I_0 cos^2\theta$, where I_0 is the intensity of incident light. A structured beam with inhomogeneous polarization distribution can generate a spatial intensity distribution when passing through a polarizer, providing a new degree of freedom to hide an image. Based on the Malus' law, an arbitrary grayscale image can be hidden in the linear polarization profile of a light beam.

Figure 5.8(b) shows the high-resolution grayscale image with 1300×1300 pixels that is to be hidden in the optical beam. In memory of the milestone work of James Clerk Maxwell in electromagnetics, we take one of his grayscale portraits as the hidden image. The resultant beam has a dimension of 390 μm by 390 μm since each pixel has a size of 300 nm by 300 nm, exhibiting the subwavelength resolution. To explain our approach, we select an area from the eyebrow region with 10×10 pixels (Figure 5.8(c)). The enlarged intensity profile and the corresponding polarization distribution are given in the left and right of Figure 5.8(c) respectively. In our design, the transmission axes of the first polarizer and the analyser (second polarizer) are respectively along horizontal and vertical directions, respectively.

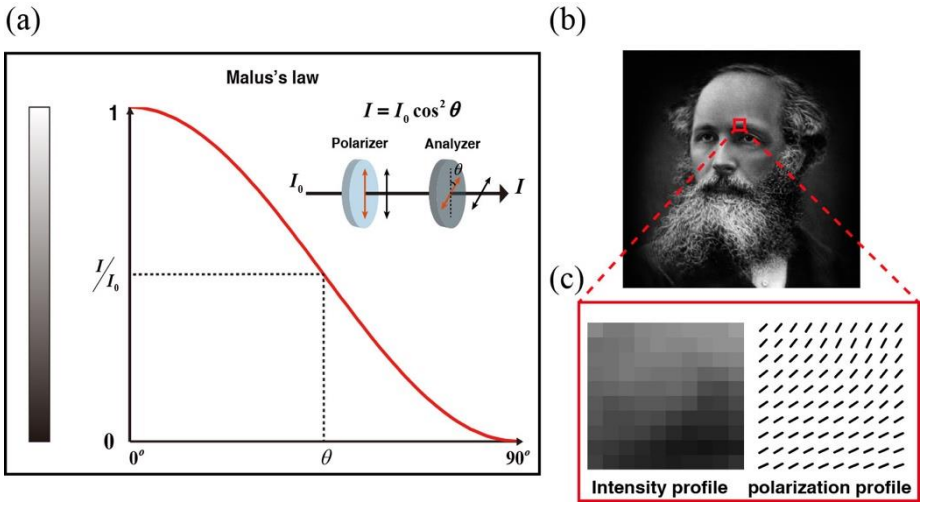

Figure 5.8. Malus' law and image hidden mechanism. (a) According to Malus' Law, when a linearly polarized light beam passes through an analyser (linear polarizer), the intensity of light transmitted by the analyser is $I = I_0 cos^2\theta$. Where I_0 is the intensity of incident light and θ is the angle between the transmission axes of the analyser and the polarizer. An arbitrary grayscale image can be hidden in the linear polarization profile of a light beam. (b) The target image of James Clerk Maxwell's grayscale portrait. (c) The details

of selected area from the eyebrow area with 10×10 pixels. The left side shows the grayscale profile and the right side shows the required polarization distribution for the analyser with a transmission axis along the vertical direction.

Figure 5.9 shows the schematic of our approach for hiding an image. A grayscale image is hidden in the structured beam with a spatially variant polarization profile, which is realised by a reflective metasurface illuminated by a laser beam at normal incidence. It is worth mentioning that two centro-symmetrically identical reflected beams are generated, whereas in the schematic, only one reflected beam is shown. An analyser (linear polarizer) is used to reveal the hidden image in the generated structured beam. Figure 5.9(a) and (b) show the simulated results with and without an analyser, respectively. This approach allows us to conceal the high capacity information in the inhomogeneous polarization profile of the laser beam and transfer the hidden information along the propagation direction of the light.

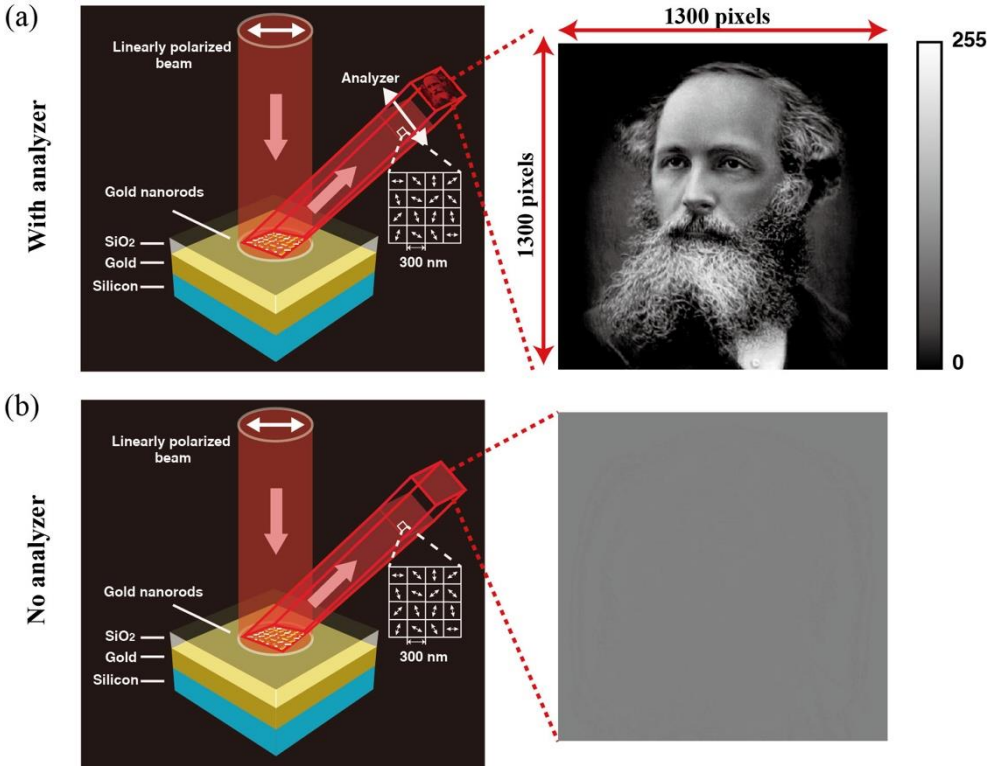

Figure 5.9. Schematic for hiding a high-resolution grayscale image. Under the illumination of linearly polarized light, two reflected beams with a spatially variant linear polarization profile are generated, which can be used to hide a high-resolution grayscale image (256 levels, black and white). It is worth mentioning that only one reflected beam is shown here for demonstration. The two beams are exactly the same apart from the

propagation direction. The hidden image is revealed by an analyser (linear polarizer) (a), while no image is obtained without it (b).

5.2.2 The simulation and experimental results

The design parameters of the metasurface and the fabrication process can be found in Chapter 2. Figure 5.10(a) shows the SEM image of the fabricated metasurface. In order to visualize the hidden image in the polarization topology of the laser beam, an analyser (linear polarizer) is used to reveal the grayscale of the image. In doing so, we do not directly observe the spatially-variant polarization profile of the laser beam but rather indirectly confirm its existence through the intensity profile (grayscale image) behind the analyser. For this metasurface, the additional phase difference between neighbouring pixels to along x direction is $\pi/5$, where the corresponding reflection angle is $12.2°$. The experimental setup is given in Figure 5.10(b). An objective with a magnification of 10x is used to expand the image for visualization with a charge-coupled device (CCD) camera.

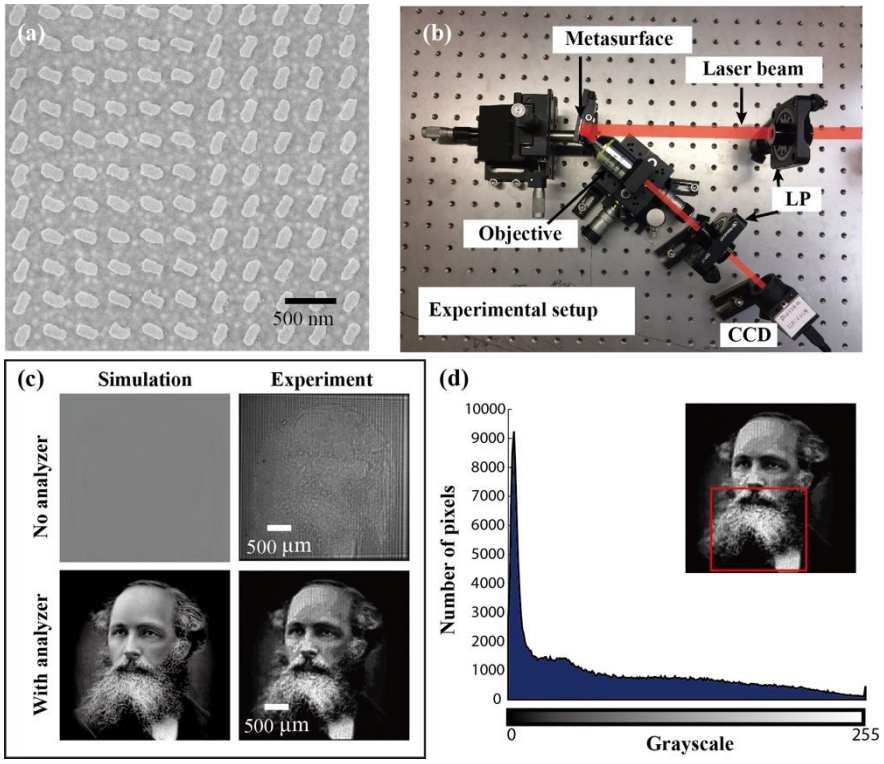

Figure 5.10. Fabricated metasurface, experiment setup and metasurface device characterization. (a) SEM image of the fabricated metasurface. The scale bar is 500 nm. (b) The experimental setup. The collimated light beam with the required linear polarization is generated using a linear polarizer (LP), and then is incident on the metasurface which is mounted on a 3D translation stage. The analyser, which is a linear polarizer, is placed in front of the CCD to reveal the hidden image. (c) The simulated and

experimental results with and without analyser. Note that the direction the transmission axis is along vertical direction. (d) The image histogram of a selected area of experiment image. The histogram is plotted with 256 equally spaced intervals, and then calculating the total number of pixels for each value.

Figure 5.10(c) shows the simulation and experiment results. As shown by the numerical calculation, no image is observed in the intensity profile of the beam (Figure 5.10(c) top left). The experimental result is given in Figure 5.10(c) (top right), indicating that the image-hidden functionality is unambiguously realised in comparison with the high-quality hidden image. A high-quality image is revealed with the analyser whose transmission axis is along the vertical direction, which agrees very well with the simulated result (Figure 5.10(c) bottom left and right). Here the transmission axes of the first polarizer and the analyser are along horizontal and vertical directions, respectively. It should be noted that the incident light beam for the simulation is a plane wave with uniform intensity, whereas the incident beam for experiment is a collimated laser beam with Gaussian profile. It causes a slight discrepancy between experiment and simulation. Another reason for the discrepancy is the imperfection of linear polarizer and fabrication error. Due to the off-axis design, another identical image is also observed in the reflected beam on the other side with respect to the surface normal. The detailed information in the measured result such as moustache, eyeball and eyebrow are clearly observed, indicating the ultrahigh resolution of the proposed approach.

To characterize the grayscale performance, we select an area from the measured image and plot the histogram that shows the distribution of intensities against grayscale level (see Figure 5.10(d)), which clearly shows that the image has a grayscale level of 256. To further analyse the performance of our approach, the dependence of simulated and measured results on the direction of transmission axis of the analyser is given in Figure 5.11. From the results at 0^o, 45^o, 90^o, 135^o, a good agreement between experimental and simulation results is found. Interestingly, the two images for the analyser with orthogonal directions of transmission axis (e.g., 0^o and 90^o, 45^o and 135^o) are complementary grayscale images, i.e., the brightest area becomes the darkest area and vice versa.

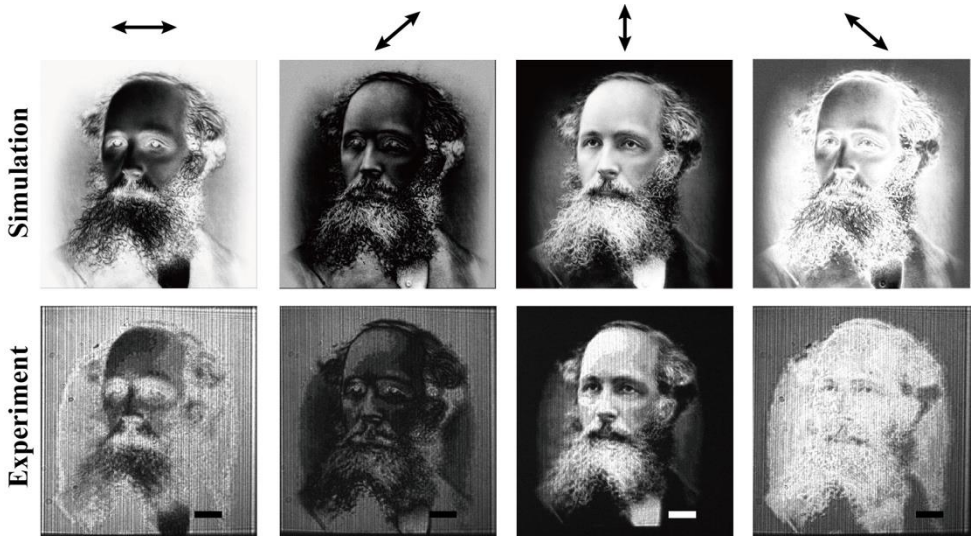

Figure 5.11. The simulated and experimental results for the analyser with various directions of transmission axis. Results at 0^o, 45^o, 90^o, 135^o are given. The scale bar is 500 µm.

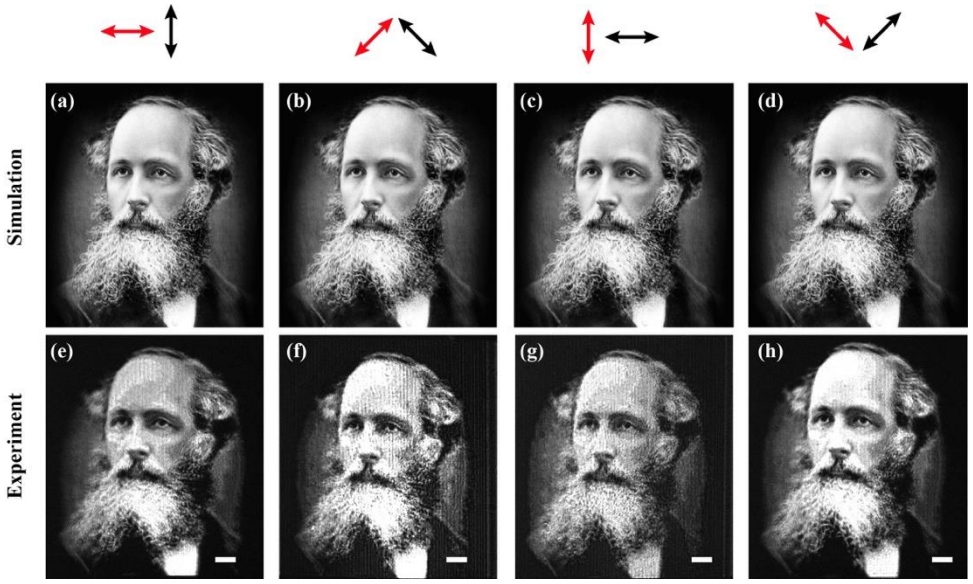

Figure 5.12. The simulated and experimentally obtained images when the angle between the transmission axes of the analyser and the polarizer is fixed at 90^o. The red and black double-headed arrows represent the transmission axes of the linear polarizer and the analyser, respectively. The transmission axis of the polarizer is set at 0^o, 45^o, 90^o, 135^o with respect to the horizontal direction, and the analyser is adjusted to maintain the transmission axis of the analyser perpendicular to that of the polarizer. (a-d) Simulated images. (e-h) Experimental images. Scale bar, 500 µm.

According to the Malus' Law, the intensity of the light transmitted by an analyser is directly proportional to the square of the cosine of angle between the transmission axes

of the analyser and the polarizer. Consequently, the quality of the hidden image (in comparison with target image) should be the same once the angle between the transmission axes of the analyser and the polarizer is fixed. In our experiment, we set the transmission angle of the polarizer at 0^o, 45^o, 90^o, 135^o, and adjust the analyser to make sure the transmission axis of the analyser is perpendicular to that of the polarizer. It is worth mentioning that the best image quality is for the angle between the transmission axes of the analyser and the polarizer fixed at 90^o. From the simulated and experimental results shown in Figure 5.12, the clear images are revealed in this case. The experimentally obtained images are captured with a monochrome CCD camera at the wavelength of 640 nm.

To characterize the performance of the approach at different polarization states of the incident light, the transmission axis of the analyser is fixed along the vertical direction. The polarization state is changed by controlling the angle between the transmission axis of the polarizer and the fast axis of the quarter-wave plate. These simulated and experimental results are shown in Figure 5.13. Although the image quality at LCP and RCP incident light is slightly different from that of the simulated results, the dependence of the revealed images on the polarization states of the incident light agrees well with the prediction. The minor difference for circular polarization states is mainly due to the imperfection of the experimental setup and fabrication error.

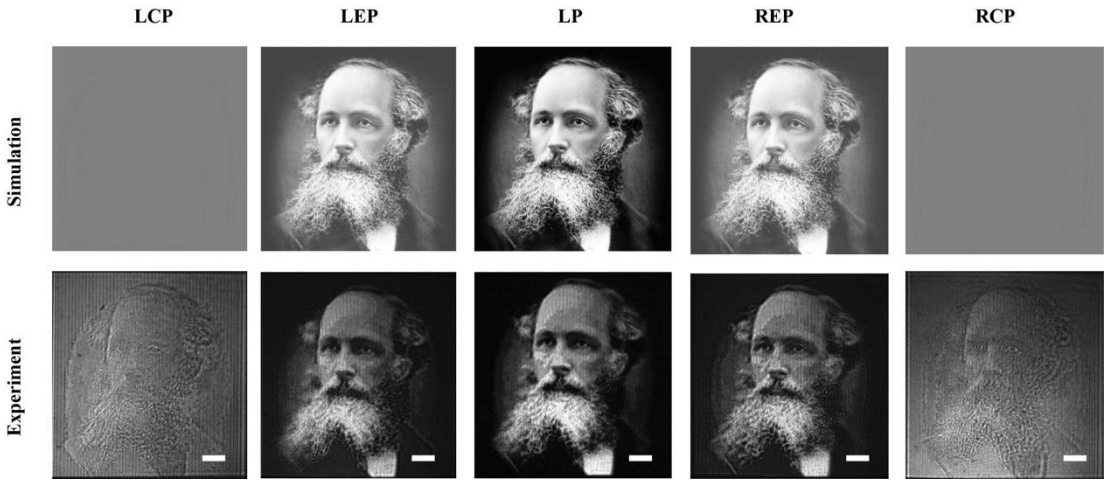

Figure 5.13. Simulated and experimentally measured results versus incident polarization states at 640 nm. The polarization states of the incident light are chosen to be LCP, left-handed elliptically polarized (LEP), linearly polarized (horizontal) (LP), right-handed elliptically polarized (REP) and RCP. Scale bar, 500 μm.

Benefiting from the broadband nature of the geometric metasurface, the developed device can operate in a broad wavelength range. Images at different wavelengths are captured and given in Figure 5.14. The experimentally revealed clear images at the wavelengths of 500 nm, 550 nm, 575 nm, 600 nm, 640 nm, and 700 nm unambiguously show the capability of the developed device in the visible range.

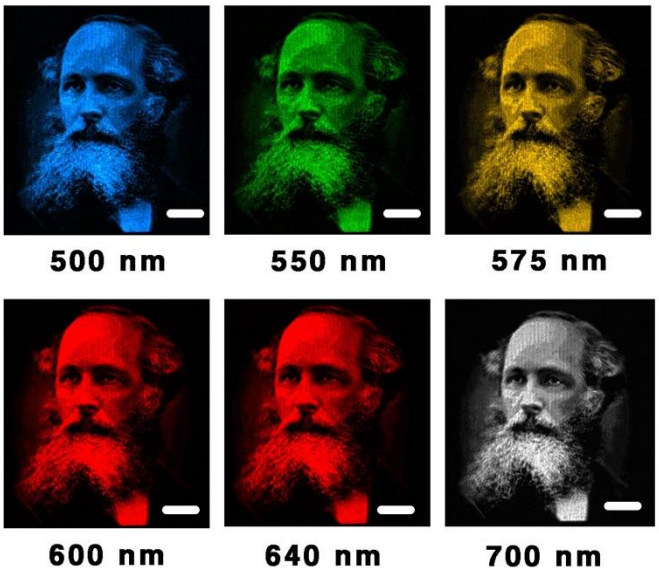

Figure 5.14. Broadband performance and robustness of the proposed approach.

Many techniques for image formation have been proposed and demonstrated in the past decades, in which the functionalities are realized by transforming the image information into the phase or amplitude space. One particular example for image formation is holography that can reconstruct a holographic image at the diffraction plane by illuminating a light beam onto an engineered surface or phase mask. The sampled amplitude distribution of the image is reconstructed due to the constructive or destructive interference at the diffraction plane. However, the phase distribution of the reconstructed image is uncertain through this process. Hence the level of spatial coherence of the resultant image is reduced. Compared to hologram, he specificity of this approach lies on encoding a high-resolution grayscale image onto the polarization profile of the laser beam. The phase correlation keeps same during the polarization encoding process. Therefore, the spatial coherence of this approach is better than hologram. Moreover, the image can be hidden and carried by the laser beam during propagation and manipulation. It can be easily displayed via an analyser with certain transmission angle. To show the advantage of our approach in terms of the image propagation, we perform a set of measurements in which we inspected the images at different propagating distance

including 0.3 m, 1 m, 2 m, and 4 m. Dielectric mirrors and lenses are used in the setup to examine the performance under multiple reflecting and focusing. The experimental setup and the recorded images are presented in Figure 5.15-5.18. The hidden grayscale images can be successfully displayed using an analyser even the beam is reflected and focused many times. It is important to note that the images will be flipped horizontally without any distortion after reflecting by mirror (Figure 5.16 and 5.18).

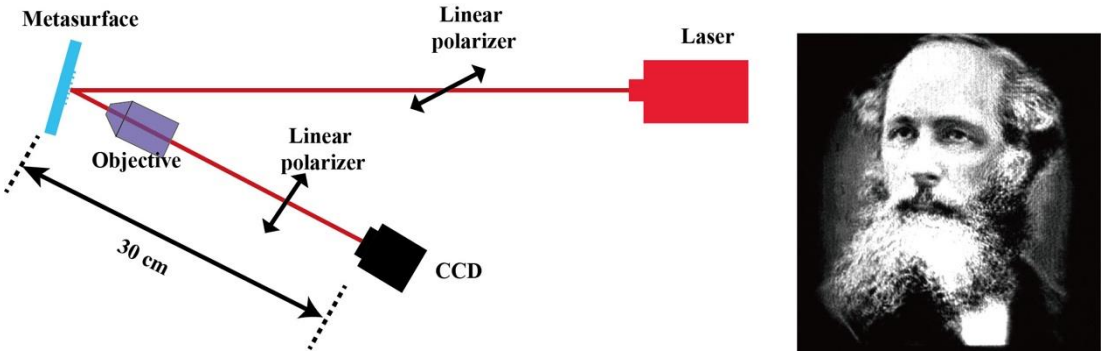

Figure 5.15. The experimental setup and experimentally recorded images at propagating distance of 0.3 m. LPs are the linear polarizers. A Nikon objective with magnification of 10X is used to enlarge the beam for projecting the image onto the CCD camera. The wavelength of incident light is 633 nm.

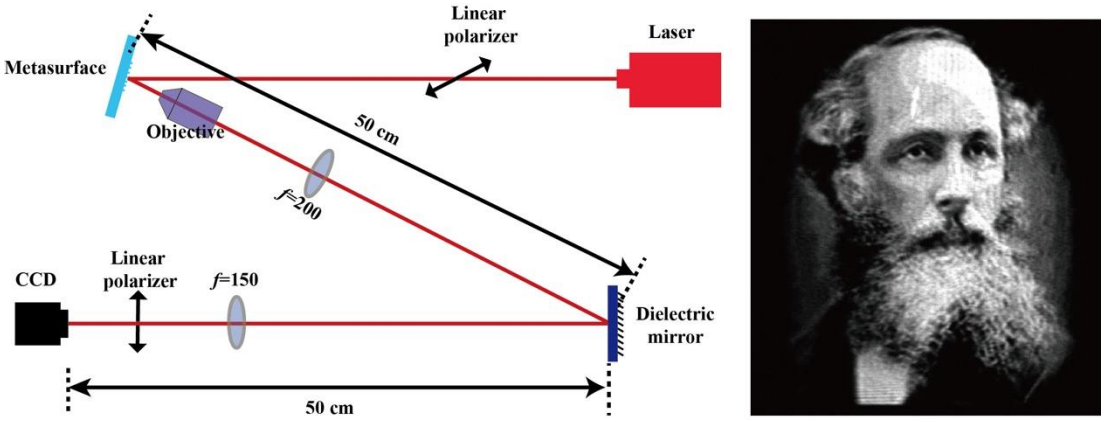

Figure 5.16. The experimental setup and experimentally recorded images at propagating distance of 1 m. Two lenses with focal lengths of $f = 200$ and $f = 150$ are used to control the beam size.

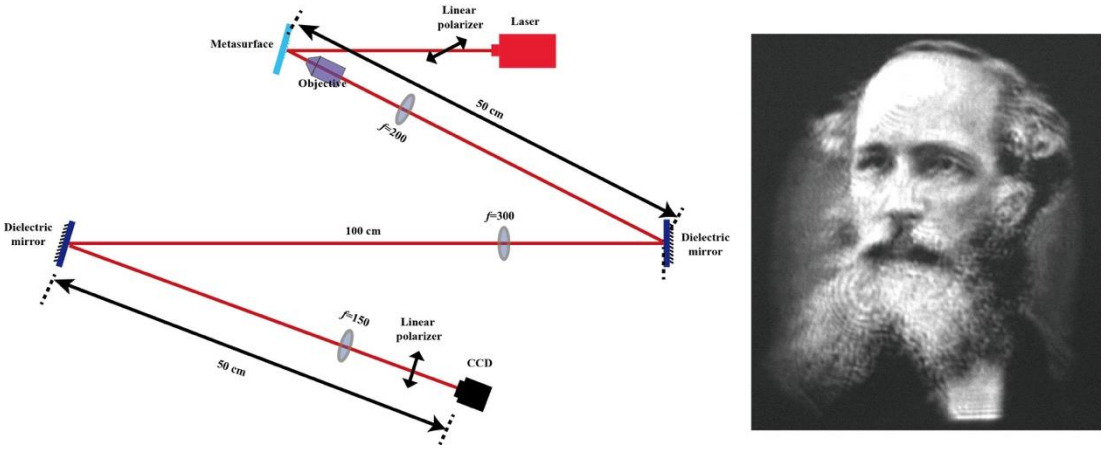

Figure 5.17. The experimental setup and experimentally recorded images at propagating distance of 2 m. Three lenses with focal lengths of $f = 300$, $f = 200$ and $f = 150$ are used to control the beam size. Two dielectric mirrors are used to reflected the beam twice.

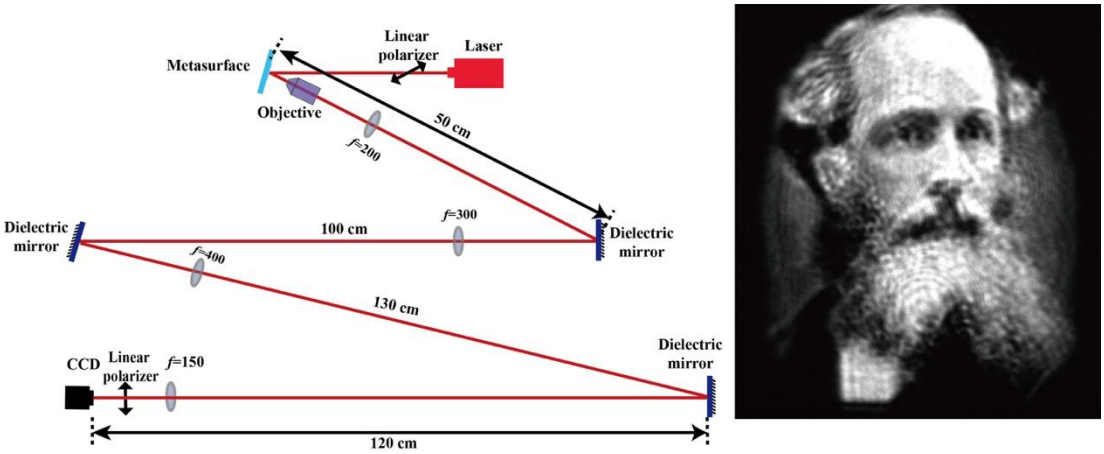

Figure 5.18. The experimental setup and experimentally recorded images at propagating distance of 4 m. Three lenses with focal lengths of $f = 200$, $f = 300$, $f = 400$, and $f = 150$ are used to control the beam size. Three dielectric mirrors are used to reflected the beam three times.

To characterize the performance of the developed device, the metasurface is exposed to a tuneable light beam from a supercontinuum laser source (NKT-SuperK EXTREME) to calculate the conversion efficiency. This approach is to generate the required linear polarization distribution, which is realised by the superposition of two orthogonal circularly polarized beams with certain phase profile. The two orthogonal circularly polarized beams should have the equal power and propagate exactly along the same direction. The key point is to design a phase profile that, upon the illumination of circularly polarized light, can simultaneously generate a pair of centro-symmetrically distributed off-axis beams with identical phase profile with respect to the normal axis. In

experiment, we measure the output power of two reflected off-axis beams at both sides under the illumination of right-handed circularly polarized light. The total power of two beams is normalized to unity. The relative power of two beams is shown in Figure 5.19(a). We can see that the power of the two beams remain equal over a broadband wavelength range (640-960 nm). The conversion efficiency is defined by the total power of two output beams divided by the power of incident light (Figure 5.19(b)). The maximum conversion efficiency is 60% at the wavelength of 820 nm. The difference between simulated and experimental results is mainly due to the titanium adhesion layer and the fabrication error of the nanopatterns.

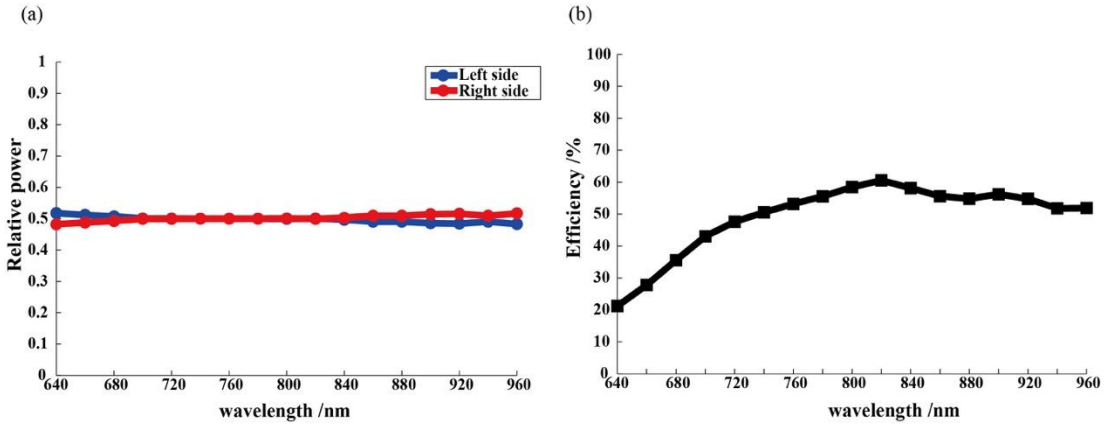

Figure 5.19. The relative power of two reflected beams and the conversion efficiency. (a) The measured relative power of two reflected beams at two sides under the illumination of right-handed circularly polarized light. (b) The measured conversion efficiency is defined as the total power of the two reflected beams divided by the power of incident beam.

This approach provides a novel route to manipulate the polarization profile with high resolution. We adopted this approach to hide a high-resolution grayscale image in the polarization topology of a laser beam that had not previously been reported in the literature. The uniqueness of our approach in precise polarization manipulation and high performance in resolution, bandwidth, and compactness renders this technology very attractive for diverse applications, such as encryption, imaging, anti-counterfeiting, optical communications, quantum science, and fundamental physics.

Chapter 6 – CONCLUSION AND FUTURE WORK

6.1 Summary of Thesis

In the beginning of the thesis, current progress on metasurfaces and their applications (for example, novel flat optical devices, metasurface hologram, surface plasmon polariton generation and higher-order harmonic generation) were reviewed. Then the fundamental physics of metasurface was discussed. After that, we experimentally demonstrated polarization-controlled holograms based on reflective metasurface. Moreover, a novel approach to realise the superposition of orbital angular momentum states was proposed and experimentally verified. Multiple superpositions of orbital angular momentum states were realised in four channels, which have great potential in classical physics and quantum optics. Inspired by these two projects, we proposed and experimentally demonstrated two metasurface methods to precisely control the polarization profile at the transverse plane of light beam. These novel approaches for polarization manipulation in subwavelength scale open a new route for various applications including imaging, smart optical components, structured beam generation, encryption, and quantum photonics.

Theoretically, we started by the optical properties of plasmonic nanostructure, and then discussed the interaction between light and nanostructures. The shape and size of nanostructures affect the spectral selective light scattering and absorption, providing a new degree of freedom to tailor the optical properties of the resultant light. After that, we discussed the geometric phase emerged from the spin-rotation coupling and built models to theoretically analyse the conversion efficiency. This content was presented in Chapter 2. The analysis of reflective metasurface with high efficiency and broadband performance was given in Chapter 2 as well. The control of phase and polarization by means of metasurface was discussed in the theoretical part of Chapter 3, Chapter 4, and Chapter 5, respectively.

Numerically, we simulated the phase distribution of the phase gradient metasurface using CST microwave studio, which was shown in Chapter 2. The conversion efficiency of reflective metasurfaces consisting of a gold ground layer, a silicon dioxide layer and a top layer of nanorods, was modelled and the simulated results are also presented in Chapter 2. We used the MATLAB software to simulate the intensity distribution of hologram (Chapter 3), the vortex beam (Chapter 4), the polarization distribution of structured beam (Chapter 5), and the grayscale image profile (Chapter 5).

Experimentally, we fabricated various metasurface samples for different applications. Initially, a reflective-type phase gradient metasurface was used to characterize the efficiency. Chapter 2 presented the fabricated sample and the measured efficiency over a broad wavelength range. Then we designed and fabricated three metasurface devices for the helicity multiplexed holograms. The far field images have been experimentally characterized and the results were shown in Chapter 3. Upon the illumination of a linearly polarized light beam, the optical illusions were perceived through our novel approach for holograms generation. The alliance between geometric metasurface and the optical illusion opens a pathway for new applications related to encryption, optical patterning, and information processing. In Chapter 4, we have experimentally demonstrated the geometric metasurfaces for vortex beam generation and characterization. More importantly, we proposed and experimentally demonstrated a facile metasurface approach to realise polarization-controllable multichannel superpositions of OAM states at will. Multiple OAM beams in four separate channels were generated by a single metasurface for an incident Gaussian beam with circular polarization. By manipulating the polarization state of the incident light, arbitrary control of the superpositions of various OAM states in multiple channels was realised, which provided a fast and efficient way for the manipulation of OAM superposition and significantly simplifies the experiment setup. This approach is of great importance for the efforts in the fields of metrology, quantum entanglement, and optical data storage. In Chapter 5, we proposed and experimentally demonstrated two different novel methods to control the polarization profile of light using geometric metasurfaces. The first method featured the spin-rotation coupling and the superposition of two circular components which were the converted part with an additional phase pickup and the residual part without a phase change. The second approach was to spatially manipulate the phase of the two circular components simultaneously to control the polarization distribution of the resultant beam. We believe that these two approaches for polarization manipulation may pave a new way for light engineering, which are of great importance for both scientific research and practical implications.

6.2 Future Work

Metasurfaces can manipulate the light properties in a desirable manner by imparting local and space-variant abrupt phase change, which provides an unprecedented capability to yield fundamental insights into physical phenomena not easily accessible using even the highest quality commercial devices. The precise control of optical response now can be designed on demand on a single subwavelength-thick interface. The attractive advantages of metasurface such as miniature size, high-resolution phase and polarization manipulation, and high efficiency, make this technology very attractive for diverse applications. In the future, the metasurface technology could be adopted in integrated photonics [148]. The striking feature of optical properties control in nanoscale make the metasurface nanodevices eminently suitable for ultracompact device and system integration. In Chapter 5, we used two cascaded metasurface devices in experimental system to decompose the resultant beam [119]. The future research of metasurface technology would focus on integration of multiple metasurface components to develop smart devices [148] or micro-system on optical waveguide [149]. On the one hand, by tailoring the size and shape of plasmonic or dielectric nanoparticles, both the polarization and phase of the light field can be controlled precisely [7, 149]. On the other hand, the mutual transforming between the scattering mode and evanescent mode can also be realised by changing the interparticle distance of neighbouring particles [59, 60, 83]. The metasurface can also be used to control the propagation of waveguide mode via strong optical scattering at subwavelength intervals.

Due to the ultrathin nature and arbitrary control of phase and polarization, metasurfaces provide the capability to empower the sensing system and metrology, such as the integration of metasurface doublet with a complementary metal-oxide-semiconductor (CMOS) image sensor to produce wide angle images at near-diffraction-limited resolution. The new compact optical configuration will enable various innovative portable instruments for many applications.

REFERENCES

[1] Yu Nanfang, Genevet Patrice, Kats Mikhail A, Aieta Francesco, Tetienne Jean-Philippe, Capasso Federico, *et al. Light Propagation with Phase Discontinuities: Generalized Laws of Reflection and Refraction*. Science **334**, 333-337 (2011).

[2] Huang Lingling, Chen Xianzhong, Mühlenbernd Holger, Li Guixin, Bai Benfeng, Tan Qiaofeng, *et al. Dispersionless phase discontinuities for controlling light propagation*. Nano Letters **12**, 5750-5755 (2012).

[3] Aieta Francesco, Genevet Patrice, Kats Mikhail A, Yu Nanfang, Blanchard Romain, Gaburro Zeno, *et al. Aberration-free ultrathin flat lenses and axicons at telecom wavelengths based on plasmonic metasurfaces*. Nano Letters **12**, 4932-4936 (2012).

[4] Kildishev Alexander V, Boltasseva Alexandra, Shalaev Vladimir M., *Planar photonics with metasurfaces*. Science **339**, 1232009 (2013).

[5] Zhao Yang, Liu Xing-Xiang, Alù Andrea. *Recent advances on optical metasurfaces*. Journal of Optics **16**, 123001 (2014).

[6] Huang Yaowei, Chen Weiting, Tsai Weiyi, Wu Pin Chieh, Wang Chih Ming, Sun Greg, *et al. Aluminum Plasmonic Multicolor Meta-Hologram*. Nano Letters **15**, 3122-3127 (2015).

[7] Arbabi Amir, Horie Yu, Bagheri Mahmood, Faraon Andrei. *Dielectric metasurfaces for complete control of phase and polarization with subwavelength spatial resolution and high transmission*. Nature Nanotechnology **10**, 937-943 (2015).

[8] Yang Yuanmu, Kravchenko, Ivan I, Briggs Dayrl P., Valentine Jason. *All-dielectric metasurface analogue of electromagnetically induced transparency*. Nature Communications **5**, 5753 (2014).

[9] Jahani Saman, Jacob Zubin. *All-dielectric metamaterials*. Nature Nanotechnology **11**, 23-36 (2016).

[10] Lin Dianmin, Fan Pengyu, Hasman Erez, Brongersma Mark L. *Dielectric gradient metasurface optical elements*. Science **345**, 298-302 (2014).

[11] Mongia R Kumar, Ittipiboon Apisak. *Theoretical and experimental investigations on rectangular dielectric resonator antennas*. IEEE Transactions on Antennas and Propagation **45**, 1348-1356 (1997).

[12] Karimi Ebrahim, Schulz Sebastian A., De Leon Israel, Qassim Hammam, Upham Jeremy, Boyd Robert W. *Generating optical orbital angular momentum at visible*

wavelengths using a plasmonic metasurface. Light: Science & Applications **3**, e167 (2014).

[13] Keren-Zur Shay, Avayu Ori, Michaeli Lior, Ellenbogen Tal. *Nonlinear Beam Shaping with Plasmonic Metasurfaces*. ACS Photonics **3**, 117-123 (2016).

[14] Wen Dandan, Yue Fuyong, Kumar Santosh, Ma Yong, Chen Ming, Ren Ximing, *et al. Metasurface for characterization of the polarization state of light*. Optics Express **23**, 10272-10281 (2015).

[15] Wen Dandan, Yue Fuyong, Li Guixin, Zheng Guoxing, Chan Kinlong, Chen Shumei, *et al. Helicity multiplexed broadband metasurface holograms*. Nature Communications **6**, 8241 (2015).

[16] Zheng Guoxing, Muhlenbernd Holger, Kenney Mitchell, Li Guixin, Zentgraf Thomas, Zhang Shuang. *Metasurface holograms reaching 80% efficiency*. Nature Nanotechnology **10**, 308-312 (2015).

[17] Khorasaninejad Mohammadreza, Chen Wei Ting, Zhu Alexander Y, Oh Jaewon, Devlin Robert C, Roques-Carmes Charles, *et al. Visible Wavelength Planar Metalenses Based on Titanium Dioxide*. IEEE Journal of Selected Topics in Quantum Electronics **23**, 1-16 (2017).

[18] Khorasaninejad Mohammadreza, Chen Wei Ting, Devlin Robert C, Oh Jaewon, Zhu Alexander Y, Capasso Federico. *Metalenses at visible wavelengths: Diffraction-limited focusing and subwavelength resolution imaging*. Science **352**, 1190-1194 (2016).

[19] Kuznetsov Arseniy I, Miroshnichenko Andrey E, Brongersma Mark L, Kivshar Yuri S, Luk'yanchuk Boris. *Optically resonant dielectric nanostructures*. Science **354**, aag2472 (2016).

[20] Eisenbach Omri, Avayu Ori, Ditcovski Ran, Ellenbogen Tal. *Metasurfaces based dual wavelength diffractive lenses*. Optics Express **23**, 3928-3936 (2015).

[21] Huang Lingling, Chen Xianzhong, Mühlenbernd Holger, Zhang Hao, Chen Shumei, Bai Benfeng, *et al. Three-dimensional optical holography using a plasmonic metasurface*. Nature Communications **4**, (2013).

[22] Aieta Francesco, Genevet Patrice, Yu Nanfang, Kats Mikhail A, Gaburro Zeno, Capasso Federico. *Out-of-plane reflection and refraction of light by anisotropic optical antenna metasurfaces with phase discontinuities*. Nano Letters **12**, 1702-1706 (2012).

[23] Berry Michael. V. *The Adiabatic Phase and Pancharatnam's Phase for Polarized Light*. Journal of Modern Optics **34**, 1401-1407 (1987).

[24] Bomzon Ze'ev, Kleiner Vladimir, Hasman Erez. *Pancharatnam–Berry phase in space-variant polarization-state manipulations with subwavelength gratings.* Optics Letters **26**, 1424-1426 (2001).

[25] Marrucci Lorenzo, Manzo C, Paparo D. *Pancharatnam-Berry phase optical elements for wave front shaping in the visible domain: switchable helical mode generation*. Applied Physics Letters **88**, 221102 (2006).

[26] West Paul R, Stewart James L, Kildishev Alexander V, Shalaev Vladimir M, Shkunov Vladimir V, Strohkendl Friedrich, *et al. All-dielectric subwavelength metasurface focusing lens*. Optics Express **22**, 26212-26221 (2014).

[27] Wen Dandan, Yue Fuyong, Ardron Marcus, Chen Xianzhong. *Multifunctional metasurface lens for imaging and Fourier transform*. Scientific Reports **6**, 27628 (2016).

[28] Zhao Yang, Alù Andrea. *Manipulating light polarization with ultrathin plasmonic metasurfaces*. Physical review B **84**, 205428 (2011).

[29] Yu Nanfang, Aieta Francesco, Genevet Patrice, Kats Mikhail A., Gaburro Zeno, Capasso Federico. *A broadband, background-free quarter-wave plate based on plasmonic metasurfaces*. Nano Letters **12**, 6328-6333 (2012).

[30] Zheng Jun, Ye Zhicheng, Sun Nanling, Zhang Rui, Sheng Zhengming, Shieh Hanping D., *et al. Highly anisotropic metasurface: a polarized beam splitter and hologram*. Scientific Reports **4**, 6491 (2014).

[31] Yue Fuyong, Wen Dandan, Zhang Chunmei, Gerardot Brian D, Wang Wei, Zhang Shuang, *et al. Multichannel Polarization-Controllable Superpositions of Orbital Angular Momentum States*. Advanced Materials **29**, (2017).

[32] Pors Anders, Nielsen Michael G., Bozhevolnyi Sergey I. *Plasmonic metagratings for simultaneous determination of Stokes parameters*. Optica **2**, 716 (2015).

[33] Ni Xingjie, Wong Zi Jing, Mrejen Michael, Wang Yuan, Zhang Xiang. *An ultrathin invisibility skin cloak for visible light*. Science **349**, 1310-1314 (2015).

[34] Wen Dandan, Yue Fuyong, Zhang Chunmei, Zang Xiaofei, Liu Huigang, Wang Wei, *et al. Plasmonic metasurface for optical rotation*. Applied Physics Letters **111**, 023102 (2017).

[35] Li Zhongyang, Palacios Edgar, Butun Serkan, Aydin Koray. *Visible-frequency metasurfaces for broadband anomalous reflection and high-efficiency spectrum splitting*. Nano Letters **15**, 1615-1621 (2015).

[36] Chen Xianzhong, Huang Lingling, Mühlenbernd Holger, Li Guixin, Bai Benfeng, Tan Qiaofeng, *et al. Dual-polarity plasmonic metalens for visible light*. Nature Communications **3**, 1198 (2012).

[37] Aieta Francesco, Kats Mikhail A, Genevet Patrice, Capasso Federico. *Multiwavelength achromatic metasurfaces by dispersive phase compensation*. Science **347**, 1342-1345 (2015).

[38] Jiang Zhi Hao, Lin Lan, Ma Ding, Yun Seokho, Werner Douglas H, Liu Zhiwen, *et al. Broadband and wide field-of-view plasmonic metasurface-enabled waveplates*. Scientific Reports **4**, 7511 (2014).

[39] Chen Weiting, Yang Kuangyu, Wang Chihming, Huang Yaowei, Sun Greg, Chiang I-Da, *et al. High-efficiency broadband meta-hologram with polarization-controlled dual images*. Nano Letters **14**, 225-230 (2014).

[40] Genevet Patrice, Capasso Federico. *Holographic optical metasurfaces: a review of current progress*. Reports on Progress in Physics **78**, 024401 (2015).

[41] Lin Jiao, Genevet Patrice, Kats Mikhail A., Antoniou Nicholas, Capasso Federico. *Nanostructured holograms for broadband manipulation of vector beams*. Nano Letters **13**, 4269-4274 (2013).

[42] Montelongo Yunuen, Tenorio-Pearl Jaime Oscar, Williams Calum, Zhang Shuang, Milne William Ireland, Wilkinson Timothy David. *Plasmonic nanoparticle scattering for color holograms*. Proceedings of the National Academy of the United States of America **111**, 12679-12683 (2014).

[43] Ni Xingjie, Kildishev Alexander V, Shalaev Vladimir M. *Metasurface holograms for visible light*. Nature Communications **4**, 2807 (2013).

[44] Bergman David, Stockman Mark. *Surface Plasmon Amplification by Stimulated Emission of Radiation: Quantum Generation of Coherent Surface Plasmons in Nanosystems*. Physical Review Letters **90**, 027402 (2003).

[45] Berini Pierre, De Leon Israel. *Surface plasmon–polariton amplifiers and lasers*. Nature Photonics **6**, 16-24 (2011).

[46] De Leon Israel, Berini Pierre. *Theory of surface plasmon-polariton amplification in planar structures incorporating dipolar gain media*. Physical review B **78**, 161401 (2008).

[47] Jen Yi-Jun. *Commentary: Arbitrarily polarized long-range surface-plasmon-polariton waves*. Journal of Nanophotonics **5**, 050304 (2011).

[48] Krenn J. R., Weeber J. C. *Surface plasmon polaritons in metal stripes and wires*. Philosophical Transactions of the Royal Society A Mathematical, Physical and Engineering Sciences **362**, 739-756 (2004).

[49] Miroshnichenko A. E., Kivshar Y. S. *Applied physics. Polarization traffic control for surface plasmons*. Science **340**, 283-284 (2013).

[50] Pitarke J. M., Silkin V. M., Chulkov E. V., Echenique P. M. *Theory of surface plasmons and surface-plasmon polaritons*. Reports on Progress in Physics **70**, 1-87 (2007).

[51] Tsai Changching, Wu Shintson. *Study of broadband polarization conversion with metallic surface-relief gratings by rigorous coupled-wave analysis*. Journal of the Optical Society of America A-Optics Image Science and Vision **25**, 1339-1348 (2008).

[52] Xie Yu-Bo, Liu Zheng-Yang, Wang Qian-Jin, Zhu Yong-Yuan, Zhang Xue-Jin. *Miniature polarization analyzer based on surface plasmon polaritons*. Applied Physics Letters **105**, 101107 (2014).

[53] Zayats Anatoly V., Smolyaninov Igor I., Maradudin Alexei A. *Nano-optics of surface plasmon polaritons*. Physics Reports **408**, 131-314 (2005).

[54] Zia Rashid, Brongersma Mark L. *Surface plasmon polariton analogue to Young's double-slit experiment*. Nature Nanotechnology **2**, 426-429 (2007).

[55] Huang Lingling, Chen Xianzhong, Bai Benfeng, Tan Qiaofeng, Jin Guofan, Zentgraf Thomas, *et al. Helicity dependent directional surface plasmon polariton excitation using a metasurface with interfacial phase discontinuity*. Light: Science & Applications **2**, e70 (2013).

[56] Wintz Daniel, Genevet Patrice, Ambrosio Antonio, Woolf Alex, Capasso Federico. *Holographic Metalens for Switchable Focusing of Surface Plasmons*. Nano Letters **15**, 3585-3589 (2015).

[57] Lin Jiao, Mueller Balthasar J. P., Wang Qian, Yuan Guanghui, Antoniou Nicholas, Yuan Xiaocong, *et al. Polarization-controlled tunable directional coupling of surface plasmon polaritons*. Science **340**, 331-334 (2013).

[58] Mueller Balthasar J. P., Leosson Kristjan, Capasso Federico. *Polarization-selective coupling to long-range surface plasmon polariton waveguides*. Nano Letters **14**, 5524-5527 (2014).

[59] Sun Shulin, He Qiong, Xiao Shiyi, Xu Qin, Li Xin, Zhou Lei. *Gradient-index meta-surfaces as a bridge linking propagating waves and surface waves*. Nature Materials **11**, 426-431 (2012).

[60] Sun Wujiong, He Qiong, Sun Shulin, Zhou Lei. *High-efficiency surface plasmon meta-couplers: concept and microwave-regime realizations*. Light: Science & Applications **5**, e16003 (2016).

[61] Lin Jiao, Wang Qian, Yuan Guanghui, Du Luping, Kou Shan Shan, Yuan Xiao-Cong. *Mode-matching metasurfaces: coherent reconstruction and multiplexing of surface waves*. Scientific Reports **5**, 10529 (2015).

[62] Li Guixin, Chen Shumei, Pholchai Nitipat, Reineke Bernhard, Wong Polis Wing, Pun Edwin Yue, *et al. Continuous control of the nonlinearity phase for harmonic generations*. Nature Materials **14**, 607-612 (2015).

[63] Segal Nadav, Keren-Zur Shay, Hendler Netta, Ellenbogen Tal. *Controlling light with metamaterial-based nonlinear photonic crystals*. Nature Photonics **9**, 180-184 (2015).

[64] Tymchenko Mykhailo, Gomez-Diaz J. S., Lee Jongwon, Nookala Nishant, Belkin Mikhail A., Alu Andrea. *Gradient Nonlinear Pancharatnam-Berry Metasurfaces*. Physical Review Letters **115**, 207403 (2015).

[65] Ye Weiming, Zeuner Franziska, Li Xin, Reineke Bernhard, He Shan, Qiu Chengwei, *et al. Spin and wavelength multiplexed nonlinear metasurface holography*. Nature Communications **7**, 11930 (2016).

[66] Nookala Nishant, Lee Jongwon, Tymchenko Mykhailo, Sebastian Gomez-Diaz J., Demmerle Frederic, Boehm Gerhard, *et al. Ultrathin gradient nonlinear metasurface with a giant nonlinear response*. Optica **3**, 283 (2016).

[67] Bohren Craig F, Huffman Donald R. *Absorption and scattering of light by small particles*. John Wiley & Sons (2008).

[68] Drude Paul. *Zur elektronentheorie der metalle*. Annalen der Physik **306**, 566-613 (1900).

[69] Drude Paul. *Zur elektronentheorie der metalle; II. Teil. galvanomagnetische und thermomagnetische effecte*. Annalen der Physik **308**, 369-402 (1900).

[70] Powell CJ. *Analysis of optical-and inelastic-electron-scattering data. II. Application to Al*. Journal of the Optical Society of America **60**, 78-93 (1970).

[71] Rakić Aleksandar D, Djurišić Aleksandra B, Elazar Jovan M, Majewski Marian L. *Optical properties of metallic films for vertical-cavity optoelectronic devices*. Applied Optics **37**, 5271-5283 (1998).

[72] Granqvist CG, Hunderi O. *Optical properties of ultrafine gold particles*. Physical review B **16**, 3513 (1977).

[73] Johnson Peter B, Christy R-W_. *Optical constants of the noble metals*. Physical review B **6**, 4370 (1972).

[74] Gaponenko Sergey V. *Introduction to nanophotonics*. Cambridge University Press (2010).

[75] Brongersma Mark L, Kik Pieter G. *Surface plasmon nanophotonics*. Springer (2007).

[76] Palik Edward D. *Handbook of optical constants of solids*. Academic press (1998).

[77] Ebbesen Thomas W, Lezec H J., Ghaemi H. F, Thio Tineke, Wolff P. A. *Extraordinary optical transmission through sub-wavelength hole arrays*. Nature **391**, 667-669 (1998).

[78] Kelly K Lance, Coronado Eduardo, Zhao Lin Lin, Schatz George C. *The optical properties of metal nanoparticles: the influence of size, shape, and dielectric environment*. Journal of Physical Chemistry B-Condensed Phase **107**, 668-677 (2003).

[79] Gans R. *Über die Form ultramikroskopischer Silberteilchen*. Annalen der Physik **352**, 270-284 (1915).

[80] Link Stephan, Mohamed MB, El-Sayed MA. *Simulation of the optical absorption spectra of gold nanorods as a function of their aspect ratio and the effect of the medium dielectric constant*. The Journal of Physical Chemistry B **103**, 3073-3077 (1999).

[81] Boyd Robert W. Nonlinear optics. In: *Handbook of Laser Technology and Applications (Three-Volume Set)*. Taylor & Francis (2003).

[82] Gotschy W, Vonmetz K, Leitner A, Aussenegg F. R. *Thin films by regular patterns of metal nanoparticles: tailoring the optical properties by nanodesign*. Applied Physics B: Lasers and Optics **63**, 381-384 (1996).

[83] Lamprecht B, Schider G, Lechner R. T, Ditlbacher H, Krenn J. R, Leitner A, *et al. Metal nanoparticle gratings: influence of dipolar particle interaction on the plasmon resonance*. Physical Review Letters **84**, 4721 (2000).

[84] Meier M, Wokaun A, Liao Paul F. *Enhanced fields on rough surfaces: dipolar interactions among particles of sizes exceeding the Rayleigh limit*. Journal of the Optical Society of America B **2**, 931-949 (1985).

[85] Goldstein Dennis H. *Polarized light*. CRC press (2016).

[86] Grady Nathaniel K, Heyes Jane E, Chowdhury Dibakar Roy, Zeng Yong, Reiten Matthew T, Azad Abul K, *et al. Terahertz metamaterials for linear polarization conversion and anomalous refraction*. Science **340**, 1304-1307 (2013).

[87] Jiang Shang-Chi, Xiong Xiang, Hu Yuan-Sheng, Hu Yu-Hui, Ma Guo-Bin, Peng Ru-Wen, *et al. Controlling the Polarization State of Light with a Dispersion-Free Metastructure*. Physical Review X **4**, 021026 (2014).

[88] Liu Na, Mesch Martin, Weiss Thomas, Hentschel Mario, Giessen Harald. *Infrared perfect absorber and its application as plasmonic sensor*. Nano Letters **10**, 2342-2348 (2010).

[89] Wen Dandan, Chen Shumei, Yue Fuyong, Chan Kinlong, Chen Ming, Ardron Marcus, *et al. Metasurface Device with Helicity - Dependent Functionality*. Advanced Optical Materials **4**, 321-327 (2016).

[90] Wen Dandan, Yue Fuyong, Ardron Marcus, Chen Xianzhong. *Multifunctional metasurface lens for imaging and Fourier transform*. Scientific Reports **6**, (2016).

[91] Yue Fuyong, Zang Xiaofei, Wen Dandan, Li Zile, Zhang Chunmei, Liu Huigang, *et al. Geometric Phase Generated Optical Illusion*. Scientific Reports **7**, 11440 (2017).

[92] Slinger Chris, Cameron Colin, Stanley Maurice. *Computer-generated holography as a generic display technology*. Computer **38**, 46-53 (2005).

[93] Kelly Damien P, Monaghan David S, Pandey Nitesh, Kozacki Tomasz, Michałkiewicz Aneta, Finke Grzegorz, *et al. Digital holographic capture and optoelectronic reconstruction for 3D displays*. International journal of digital multimedia broadcasting **2010**, (2010).

[94] Huang Yao-Wei, Chen Wei Ting, Tsai Wei-Yi, Wu Pin Chieh, Wang Chih-Ming, Sun Greg, *et al. Aluminum plasmonic multicolor meta-hologram*. Nano Letters **15**, 3122-3127 (2015).

[95] Li Xiong, Chen Lianwei, Li Yang, Zhang Xiaohu, Pu Mingbo, Zhao Zeyu, *et al. Multicolor 3D meta-holography by broadband plasmonic modulation*. Science Advances **2**, e1601102 (2016).

[96] Montelongo Yunuen, Tenorio-Pearl Jaime Oscar, Williams Calum, Zhang Shuang, Milne William Ireland, Wilkinson Timothy David. *Plasmonic nanoparticle scattering for color holograms*. Proceedings of the National Academy of Sciences **111**, 12679-12683 (2014).

[97] Yifat Yuval, Eitan Michal, Iluz Zeev, Hanein Yael, Boag Amir, Scheuer Jacob. *Highly efficient and broadband wide-angle holography using patch-dipole nanoantenna reflectarrays*. Nano Letters **14**, 2485-2490 (2014).

[98] Wang Bo, Dong Fengliang, Li Qi-Tong, Yang Dong, Sun Chengwei, Chen Jianjun, *et al. Visible-frequency dielectric metasurfaces for multiwavelength achromatic and highly dispersive holograms*. Nano Letters **16**, 5235-5240 (2016).

[99] Huang Kun, Dong Zhaogang, Mei Shengtao, Zhang Lei, Liu Yanjun, Liu Hong, *et al. Silicon multi-meta-holograms for the broadband visible light*. Laser & Photonics Reviews **10**, 500-509 (2016).

[100] Mueller J. P. Balthasar, Rubin Noah A, Devlin Robert C, Groever Benedikt, Capasso Federico. *Metasurface Polarization Optics: Independent Phase Control of Arbitrary Orthogonal States of Polarization*. Physical Review Letters **118**, 113901 (2017).

[101] Gerchberg Ralph W. *A practical algorithm for the determination of the phase from image and diffraction plane pictures*. Optik **35**, 237-246 (1972).

[102] Allen Les, Beijersbergen Marco W., Spreeuw R. J. C., Woerdman J. P. *Orbital angular momentum of light and the transformation of Laguerre-Gaussian laser modes*. Physical Review A **45**, 8185-8189 (1992).

[103] Padgett Miles, Bowman Richard. *Tweezers with a twist*. Nature Photonics **5**, 343-348 (2011).

[104] Nicolas A., Veissier L., Giner L., Giacobino E., Maxein D., Laurat J. *A quantum memory for orbital angular momentum photonic qubits*. Nature Photonics **8**, 234-238 (2014).

[105] Lei Ting, Zhang Meng, Li Yuru, Jia Ping, Liu Gordon Ning, Xu Xiaogeng, *et al. Massive individual orbital angular momentum channels for multiplexing enabled by Dammann gratings*. Light: Science & Applications **4**, e257 (2015).

[106] Bozinovic Nenad, Yue Yang, Ren Yongxiong, Tur Moshe, Kristensen Poul, Huang Hao, *et al. Terabit-Scale Orbital Angular Momentum Mode Division Multiplexing in Fibers*. Science **340**, 1545-1548 (2013).

[107] Salem Mohamed A, Caloz C. Precision orbital angular momentum (OAM) multiplexing communication using a metasurface. In: *Advanced Electromagnetic Materials in Microwaves and Optics (METAMATERIALS), 2013 7th International Congress on*. IEEE 94-96 (2013).

[108] Lavery Martin P. J., Speirits Fiona C, Barnett Stephen M, Padgett Miles J. *Detection of a spinning object using light's orbital angular momentum*. Science **341**, 537-540 (2013).

[109] D'Ambrosio Vincenzo, Spagnolo Nicolò, Del Re Lorenzo, Slussarenko Sergei, Li Ying, Kwek Leong Chuan, *et al. Photonic polarization gears for ultra-sensitive angular measurements*. Nature Communications **4**, (2013).

[110] Poynting JH. *The wave motion of a revolving shaft, and a suggestion as to the angular momentum in a beam of circularly polarised light*. Proceedings of the Royal Society of London Series A, Containing Papers of a Mathematical and Physical Character **82**, 560-567 (1909).

[111] Beth Richard A. *Mechanical detection and measurement of the angular momentum of light*. Physical Review **50**, 115 (1936).

[112] Baumann S. M., Kalb D. M., MacMillan L. H., Galvez E. J. *Propagation dynamics of optical vortices due to Gouy phase*. Optics Express **17**, 9818-9827 (2009).

[113] Marrucci Lorenzo. *The q-plate and its future*. Journal of Nanophotonics **7**, 078598-078598 (2013).

[114] Marrucci Lorenzo, Karimi Ebrahim, Slussarenko Sergei, Piccirillo Bruno, Santamato Enrico, Nagali Eleonora, *et al. Spin-to-orbital conversion of the angular momentum of light and its classical and quantum applications*. Journal of Optics **13**, 064001 (2011).

[115] Nagali E., Sciarrino F., De Martini F., Marrucci L., Piccirillo B., Karimi E., *et al. Quantum information transfer from spin to orbital angular momentum of photons*. Physical Review Letters **103**, 013601 (2009).

[116] Cardano Filippo, Karimi Ebrahim, Slussarenko Sergei, Marrucci Lorenzo, de Lisio Corrado, Santamato Enrico. *Polarization pattern of vector vortex beams generated by q-plates with different topological charges*. Applied Optics **51**, C1-C6 (2012).

[117] Rumala Yisa S., Milione Giovanni, Nguyen Thien An, Pratavieira Sebastiao, Hossain Zabir, Nolan Daniel, *et al. Tunable supercontinuum light vector vortex beam generator using a q-plate*. Optics Letters **38**, 5083-5086 (2013).

[118] Beresna Martynas, Gecevičius Mindaugas, Kazansky Peter G, Gertus Titas. *Radially polarized optical vortex converter created by femtosecond laser nanostructuring of glass*. Applied Physics Letters **98**, 201101 (2011).

[119] Yue Fuyong, Wen Dandan, Xin Jingtao, Gerardot Brian D, Li Jensen, Chen Xianzhong. *Vector vortex beam generation with a single plasmonic metasurface*. ACS Photonics **3**, 1558-1563 (2016).

[120] Bomzon Ze'ev, Biener Gabriel, Kleiner Vladimir, Hasman Erez. *Radially and azimuthally polarized beams generated by space-variant dielectric subwavelength gratings*. Optics Letters **27**, 285-287 (2002).

[121] Yi Xunong, Ling Xiaohui, Zhang Zhiyou, Li Ying, Zhou Xinxing, Liu Yachao, *et al. Generation of cylindrical vector vortex beams by two cascaded metasurfaces*. Optics Express **22**, 17207-17215 (2014).

[122] Beckley Amber M., Brown Thomas G., Alonso Miguel A. *Full Poincare beams*. Optics Express **18**, 10777-10785 (2010).

[123] Beckley Amber M., Brown Thomas G., Alonso Miguel A. *Full Poincare beams II: partial polarization*. Optics Express **20**, 9357-9362 (2012).

[124] Dorn R., Quabis S., Leuchs G. *Sharper Focus for a Radially Polarized Light Beam*. Physical Review Letters **91**, 233901 (2003).

[125] Berg-Johansen Stefan, Töppel Falk, Stiller Birgit, Banzer Peter, Ornigotti Marco, Giacobino Elisabeth, *et al. Classically entangled optical beams for high-speed kinematic sensing*. Optica **2**, 864 (2015).

[126] Lavery Martin P. J., Barnett Stephen M., Speirits Fiona C., Padgett Miles J. *Observation of the rotational Doppler shift of a white-light, orbital-angular-momentum-carrying beam backscattered from a rotating body*. Optica **1**, 1-4 (2014).

[127] Andersen MF, Ryu C, Cladé Pierre, Natarajan Vasant, Vaziri A, Helmerson Kristian, *et al. Quantized rotation of atoms from photons with orbital angular momentum*. Physical Review Letters **97**, 170406 (2006).

[128] Sun Kuei, Qu Chunlei, Zhang Chuanwei. *Spin–orbital-angular-momentum coupling in Bose-Einstein condensates*. Physical Review A **91**, 063627 (2015).

[129] Mair Alois, Vaziri Alipasha, Weihs Gregor, Zeilinger Anton. *Entanglement of the orbital angular momentum states of photons*. Nature **412**, 313-316 (2001).

[130] Karimi Ebrahim, Leach Jonathan, Slussarenko Sergei, Piccirillo Bruno, Marrucci Lorenzo, Chen Lixiang, *et al. Spin-orbit hybrid entanglement of photons and quantum contextuality*. Physical Review A **82**, 022115 (2010).

[131] Fickler Robert. *Quantum Entanglement of Complex Structures of Photons*. Springer (2015).

[132] Bhatti Daniel, von Zanthier Joachim, Agarwal Girish S. *Entanglement of polarization and orbital angular momentum*. Physical Review A **91**, 062303 (2015).

[133] Karimi Ebrahim, Slussarenko Sergei, Piccirillo Bruno, Marrucci Lorenzo, Santamato Enrico. *Polarization-controlled evolution of light transverse modes and associated Pancharatnam geometric phase in orbital angular momentum*. Physical Review A **81**, 053813 (2010).

[134] Naidoo Darryl, Roux Filippus S., Dudley Angela, Litvin Igor, Piccirillo Bruno, Marrucci Lorenzo, *et al. Controlled generation of higher-order Poincaré sphere beams from a laser*. Nature Photonics **10**, 327-332 (2016).

[135] Fickler Robert, Krenn Mario, Lapkiewicz Radek, Ramelow Sven, Zeilinger Anton. *Real-time imaging of quantum entanglement*. Scientific Reports **3**, (2013).

[136] Liu Jinpeng, Min Changjun, Lei Ting, Du Luping, Yuan Yangsheng, Wei Shibiao, *et al. Generation and detection of broadband multi-channel orbital angular momentum by micrometer-scale meta-reflectarray*. Optics Express **24**, 212-218 (2016).

[137] Milione Giovanni, Sztul H. I., Nolan D. A., Alfano R. R. *Higher-Order Poincare Sphere, Stokes Parameters, and the Angular Momentum of Light*. Physical Review Letters **107**, 053601 (2011).

[138] Milione Giovanni, Evans S, Nolan DA, Alfano RR. *Higher order Pancharatnam-Berry phase and the angular momentum of light*. Physical Review Letters **108**, 190401 (2012).

[139] Yi Xunong, Liu Yaochao, Ling Xiaohui, Zhou Xinxing, Ke Yougang, Luo Hailu, *et al. Hybrid-order Poincare sphere*. Physical Review A **91**, 023801 (2015).

[140] Galvez Enrique J, Khadka Shreeya, Schubert William H, Nomoto Sean. *Poincaré-beam patterns produced by nonseparable superpositions of Laguerre–Gauss and polarization modes of light*. Applied Optics **51**, 2925-2934 (2012).

[141] Bauer Thomas, Banzer Peter, Karimi Ebrahim, Orlov Sergej, Rubano Andrea, Marrucci Lorenzo, *et al. Observation of optical polarization Möbius strips*. Science **347**, 964-966 (2015).

[142] D'Ambrosio Vincenzo, Nagali Eleonora, Walborn Stephen P., Aolita Leandro, Slussarenko Sergei, Marrucci Lorenzo, *et al. Complete experimental toolbox for alignment-free quantum communication*. Nature Communications **3**, (2012).

[143] Hamazaki Junichi, Mineta Yuriya, Oka Kazuhiko, Morita Ryuji. *Direct observation of Gouy phase shift in a propagating optical vortex*. Optics Express **14**, 8382-8392 (2006).

[144] Feng Simin, Winful Herbert G. *Physical origin of the Gouy phase shift*. Optics Letters **26**, 485-487 (2001).

[145] Hiesmayr B. C, de Dood MJA, Löffler W. *Observation of Four-Photon Orbital Angular Momentum Entanglement*. Physical Review Letters **116**, 073601 (2016).

[146] Yue Fuyong, Zhang Chunmei, Zang Xiaofei, Wen Dandan, Gerardot Brian D, Zhang Shuang, *et al. High-resolution grayscale image hidden in a laser beam*. Light: Science & Applications, (2018).

[147] Cheng W., Haus J. W., Zhan Q. W. *Propagation of vector vortex beams through a turbulent atmosphere*. Optics Express **17**, 17829-17836 (2009).

[148] Arbabi Amir, Arbabi Ehsan, Horie Yu, Kamali Seyedeh Mahsa, Faraon Andrei. *Planar metasurface retroreflector*. Nature Photonics **11**, 415-420 (2017).

[149] Li Z., Kim M. H., Wang C., Han Z., Shrestha S., Overvig A. C., *et al. Controlling propagation and coupling of waveguide modes using phase-gradient metasurfaces*. Nat Nanotechnol, (2017).